

METEORITICS & PLANETARY SCIENCE

Sierra Gorda 009: A New Member of the Metal-Rich G Chondrites Grouplet

Journal:	<i>Meteoritics & Planetary Science</i>
Manuscript ID	MAPS-3340.R2
Manuscript Type:	Article
Date Submitted by the Author:	n/a
Complete List of Authors:	<p>Ivanova, Marina; Vernadsky Institute, Laboratory of meteoritics; Vernadsky Institute, Laboratory of Meteoritics Lorenz, Cyril; Vernadsky Institute, Laboratory of Meteoritics Humayun, Munir; Florida State University, National High Magnetic Field Laboratory and Dept. of Geological Sciences; Corrigan, Cari; Smithsonian, Mineral Science; Ludwig, Thomas; Institut für Geowissenschaften, Klaus Tschira-Labor für Kosmochemie, Ruprecht-Karls-Universität Heidelberg Trieloff, Mario; Institut für Geowissenschaften, Klaus Tschira-Labor für Kosmochemie, Ruprecht-Karls-Universität Heidelberg, D-69120 Heidelberg Righter, Kevin; NASA Johnson Space Center, MAIL CODE XI2; Franchi, Ian; The Open University, The Department of Physical Sciences Verchovsky, Alexander; The Open University, Department of Physical Sciences Korochantseva, E. V. ; Vernadsky Institute Kozlov, Vladimir Teplyakova, Svetlana; Vernadsky Institute, Laboratory of Meteoritics Korochantsev, Alexander; Vernadsky Institute, Laboratory of Meteoritics Grokhovsky, Victor; Ural Federal University,</p>
Keywords:	Anomalous meteorite(s), Carbon, Classification, fugacity < Oxygen

SCHOLARONE™
Manuscripts

Sierra Gorda 009: A New Member of the Metal-Rich G Chondrites Grouplet

Marina A. IVANOVA^{1**,*}, Cyril A. LORENZ¹, Munir HUMAYUN³, Catherine M. CORRIGAN², Thomas LUDWIG⁴, Mario TRIELOFF⁴, Kevin RIGHTER⁶, Ian A. FRANCHI⁵, Alexander B. VERCHOVSKY⁵, Ekaterina V. KOROCHANTSEVA¹, Vladimir V. KOZLOV⁷, Svetlana N. TEPLYAKOVA¹, Alexander V. KOROCHANTSEV¹, Victor I. GROKHOVSKY⁷

^{1*}Vernadsky Institute of Geochemistry and Analytical Chemistry, Moscow 119991, Russia;

^{2**}National Museum of Natural History, Smithsonian Institution, Washington DC, USA;

³National High Magnetic Field Laboratory and Department of Earth, Ocean & Atmospheric Science, Florida State University, Tallahassee, 1800 E. Paul Dirac Drive, FL 32310, USA;

⁴Institut für Geowissenschaften, Klaus Tschira-Labor für Kosmochemie, Ruprecht-Karls-Universität Heidelberg, D-69120 Heidelberg, Germany;

⁵Planetary and Space Sciences Research Institute, Open University, Milton Keynes, MK7 6AA, UK;

⁶NASA – Johnston Space Center, Mailcode XI2, USA;

⁷Oxford Instruments OM & Gatan Inc., Moscow Office 26, Denisovskii Pereulok, Moscow, 105005;

⁷Ural Federal University, Ekaterinburg, 620002, Russian Federation.

*Correspondence author, e-mail: *meteorite2000@mail.ru; **ivanovama@si.edu

To be submitted in *Meteoritics and Planetary Science*, January 20, 2020.

ABSTRACT

We investigated the metal-rich chondrite Sierra Gorda (SG) 009, a member of the new G chondrite grouplet (also including NWA 5492, GRO 95551). G chondrites contain 23% metal, very reduced silicates, and rare oxidized mineral phases (Mg-chromite, FeO-rich pyroxene). G chondrites are not related to CH-CB chondrites, based on bulk O, C and N isotopic compositions, mineralogy and geochemistry. G chondrites have no fine-grained matrix or matrix lumps enclosing hydrated material typical for CH-CB chondrites. G chondrites' average metal compositions are similar to H chondrites. Siderophile and lithophile geochemistry indicate sulfidization and fractionation of the SG 009 metal and silicates, unlike NWA 5492 and GRO 95551. The G chondrites have average O isotopic compositions $\Delta^{17}\text{O} > 0 \text{ ‰}$ ranging between bulk enstatite (E) and ordinary (O) chondrites. An Al-rich chondrule from SG 009 has $\Delta^{17}\text{O} < 0 \text{ ‰}$ indicating some heterogeneity in oxygen isotopic composition of G chondrite components. SG 009's bulk carbon and nitrogen isotopic compositions correspond to E and O chondrites. Neon isotopic composition reflects a mixture of cosmogenic and solar components, and cosmic ray exposure age of SG 009 is typical for O, E, and R chondrites. G chondrites are closely related to O, E, and R chondrites and may represent a unique metal-rich parent asteroid containing primitive and fractionated material from the inner Solar System. Oxidizing and reducing conditions during SG 009 formation may be connected with a chemical micro-environment and possibly could indicate that G chondrites may have formed by a planetesimal collision resulting in the lack of matrix.

INTRODUCTION

The study of metal-rich meteorites with textural similarities to CH or CB chondrites from different Solar System reservoirs and/or locations may provide a better understanding of early chemical fractionation processes in the Solar System, formation and accretion of metal-rich parent bodies, and relationship to other types of material. The metal-rich chondrites (~20 vol% of Fe,Ni - metal) are very intriguing meteorites and have attracted a lot of attention recently. They include carbonaceous (C) chondrites - CH, CB_a+CB_b chondrites (Weisberg et al., 1990, 2001; Meibom et al., 1999; Krot et al., 2002; Campbell et al., 2001, Ivanova and Petaev, 2015), the CH/CB_b chondrite Isheyevo (Ivanova et al. 2008), the recently studied metal-rich chondrites Northwest Africa (NWA) 5492 and Grosvenor Mountains (GRO) 95551 (Weisberg et al. 2012, 2015) and new ungrouped chondrites Northwest Africa (NWA) 12273 and 12379 which have affinities to L/LL chondrites (Jansen et al. 2019, Agee et al. 2019).

CB chondrites (bencubbinites) are divided into CB_a (coarse-grained) and CB_b (fine-grained) (Weisberg et al. 2001). They consist of chemically zoned (CB_b) and unzoned (CB_a) Fe,Ni-alloy, non-porphyritic (skeletal olivine, SO) and cryptocrystalline (CC) magnesian chondrules, which predominate over other clast types. Chondrules have a narrow range of oxygen isotopic compositions ($\Delta^{17}\text{O} \sim -2.5 \pm 0.5 \text{ ‰}$), while refractory inclusions surrounded by a Wark-Lovering rim, are depleted in ^{16}O ($\Delta^{17}\text{O} \sim$ from -15 ‰ to -5 ‰) compared to CV3 CAIs. CB chondrites contain hydrated lithic clasts, and lack the matrix component (Weisberg et al. 2001; Krot et al. 2014, 2017). Despite a lot of data, the origin of CB chondrites remains unclear. Whether their chondrules and other components formed in the early solar nebula (Newsom and Drake, 1979; Weisberg et al., 1990, 2001; Meibom et al., 1999; Krot et al., 2002; Campbell et al., 2001) or are products of late stage protoplanetary collisions (e.g., Wasson, 1990; Campbell et al., 2002; Amelin and Krot, 2005; Campbell et al., 2005; Krot et al., 2005; Fedkin et al., 2015; Oulton et al., 2016), remains debatable.

CH chondrites mainly consist of zoned and unzoned Fe,Ni-metal (22 vol.%) and common carbonaceous chondrite chondrules - magnesian, ferrous, and Al-rich porphyritic chondrules, the oxygen isotopic compositions of which vary over a wide range ($\Delta^{17}\text{O} \sim$ from -5 ‰ to $+4 \text{ ‰}$). Like CB chondrites, CH chondrites do not have a matrix component. Refractory inclusions are surrounded by Wark-Lovering rims, which have $\Delta^{17}\text{O} \sim -24 \text{ ‰}$. (Kimura et al., 1993; Weber et

1
2
3 al., 1995; Ivanova et al. 2008; Krot et al., 2008, 2010, 2012). Krot et al. (2008, 2010, 2012)
4 suggested that CB and CH chondrites are genetically related and represent different samples of
5 chondritic components formed by both shock and nebular processes. Weisberg et al. (1995) also
6 pointed out the chemical and isotopic similarities of CB, CH, and CR chondrites and proposed
7 combining them into a single CR clan of meteorites. According to this work, the CR clan
8 meteorites formed at the same time and at approximately the same heliocentric distance.
9

10
11
12
13 The Isheyev meteorite (CH/CBb) has the characteristics of both CH and CB chondrites
14 (Ivanova et al. 2008). It is known that CH/CBb chondrites have the heaviest nitrogen ($\delta^{15}\text{N} > 1000$
15 ‰) (Sugiura et al. 2000; Weisberg et al. 2001), like all other CB chondrites, and carbon is enriched
16 in the heavy isotope. Isheyev has an K-Ar age 3.4 Ga, but it cannot be ruled out that shock events
17 affected this age. The cosmic ray exposure age (CRE), determined by cosmogenic ^{38}Ar , is 34 Ma,
18 which corresponds to the age of the bencubbinites of the CBa group (Ivanova et al. 2008).
19

20
21
22
23 Two recently studied ungrouped meteorites, NWA 5492 and GRO 95551 (Weisberg et al.
24 2012, 2015) have affinities to CH-CB chondrites, but their silicate compositions are more reduced
25 than those in CH and CB chondrites. Sulfides in NWA 5492 and GRO 95551 are more abundant
26 and not related to the metal, as in the CB chondrites. Average metal compositions in NWA 5492
27 and GRO 95551 are close to H chondrite metal. Oxygen isotopic compositions of NWA 5492 and
28 GRO 95551 chondrules and their fragments show a range with most of having $\Delta^{17}\text{O}$ values >0 ‰.
29 Since there is no matrix component, their average chondrule + fragment oxygen isotopic
30 compositions are considered to be representative of whole rock and ($\Delta^{17}\text{O}$ values) are between
31 those for enstatite (E) and ordinary (O) chondrites. These data argue for a close relationship
32 between NWA 5492 and GRO 95551 and suggest that they are the first examples of a new type of
33 metal-rich chondrite, called G-chondrites (Weisberg et al., 2015).
34

35
36
37
38
39
40
41
42
43 NWA 12379 and 12273 (Jansen et al., 2019; Agee et al., 2019) are recently studied metal-
44 rich chondrites with unique characteristics that distinguish them from meteorites of any previously
45 described chondrite groups. They are listed as “probably paired” in the Meteoritical Bulletin.
46 Silicates in these meteorites are similar to mildly metamorphosed L3 chondrites (Jansen et al.
47 2019). However, the high metal content (~70 vol%) and complete lack of matrix are inconsistent
48 with OC classification; these characteristics are typical for metal-rich carbonaceous (CH and CB)
49 and G chondrites. In contrast to the metal-rich chondrites, but similar to OCs, the meteorite NWA
50 12379 experienced thermal metamorphism that resulted in nearly complete chemical equilibration
51
52
53
54
55
56
57

1
2
3 of chondrule olivine, and formation of Cl-apatite, merrillite, chromite, tetrataenite, and ferroan
4 olivine that replaces low-Ca pyroxene. It is unclear whether the major components of this
5 meteorite, chondrules and metal, originate from the same cosmochemical reservoir in the early
6 solar system or formed separately and were mixed together afterwards.
7
8
9

10 The recent discovery of a possible new member of the G chondrites, Sierra Gorda 009, led
11 us to perform a comprehensive petrologic, geochemical and isotopic study of this meteorite
12 (Ivanova et al. 2019). A goal of this investigation is to study the main properties of a new grouplet
13 of metal-rich G-chondrites (GCs), and to discuss the possible origin of their components based on
14 our comprehensive study of the Sierra Gorda (SG) 009 ungrouped metal-rich chondrite.
15
16
17
18
19

20 ANALYTICAL PROCEDURES

21 Mineralogy and Petrology

22
23
24
25
26 Two polished thin and thick sections with total surface area of ~ 5.5 cm² of the Sierra Gorda
27 009 meteorite were studied by optical microscopy at the Vernadsky Institute (Russia) and Ural
28 Federal University (Russia). Backscattered electron (BSE) imaging and energy dispersive X-ray
29 spectroscopy (EDS) analyses were performed using Tescan scanning electron microscope (SEM)
30 with analytical equipment of the Oxford Instruments AztecLive Automate with detector UltimMax
31 100 (Russia) and FEI Nova NanoSEM 600 scanning electron microscope (SEM) the Smithsonian
32 Institution (SI) (USA). FEI Nova NanoSEM 600 SEM is, equipped with a Thermo Electron energy
33 dispersive X-ray spectrometer and the Noran System Six software at the SI. The SEM was operated
34 at 15kV with a beam current of 2–3 nA. Approximately half of the section was subsequently
35 mapped in Si, Mg, Fe, Ca, Al, Ti, Fe, Ni, S, Cr, P x-rays using the FEI Nova NanoSEM 600. For
36 both instruments a fully focused electron beam was operated at 15 kV accelerating voltage, 100
37 nA beam current, 20–30 ms per pixel acquisition time, and a spatial resolution of ~ 2 –3 μ m per
38 pixel. Ca, Al, Mg, Ti, Na, Cl, Fe, Ni, and Sc were measured using $K\alpha$ lines. The elemental maps
39 in Mg, Ca, and Al $K\alpha$ were combined using an RGB-color scheme (Mg – red, Ca – green, Al –
40 blue) and the ENVI (Environment for Visualizing Images) software package.
41
42
43
44
45
46
47
48
49
50
51

52 Mineral compositions were analyzed with a JEOL JXA-8530+ Hyperprobe five-
53 spectrometer electron microprobe at the Smithsonian Institution. Operating conditions were 15 kV
54 accelerating voltage, a fully focused beam with 20 nA beam current, and peak counting times of
55
56
57

1
2
3 20 seconds for major elements and 40 seconds for minor elements. Natural and synthetic minerals
4 were used both as calibration standards and, in some cases, as unknowns that were analyzed at the
5 beginning and the end of every run. Matrix corrections were applied using Phi-Rho-Z (for JEOL
6 JXA 8530+) software routines. Detection limits for silicates were (in wt.%): SiO₂, TiO₂, Al₂O₃,
7 Cr₂O₃, FeO, MnO, MgO, CaO, NiO – 0.02; K₂O, Na₂O, Sc₂O₃, V₂O₃ – 0.05; ZrO₂– 0.1; Y₂O₃ –
8 0.3; HfO₂– 0.4. The modal abundances were estimated based on high resolution backscattered
9 electron (BSE) images using Adobe Photoshop™ software. Platinum group elements (PGE) in
10 metal particle of SG 009 were studied using a Tescan SEM with analytical equipment of the Oxford
11 Instruments AztecLive Automate with detector UltimMax 100 (Russia) and a Tescan MIRA
12 3MLU scanning electron microscope equipped with an INCA Energy 450 XMax 80 microanalysis
13 system (Oxford Instruments Ltd.) at the V.S. Sobolev Institute of Geology and Mineralogy (IGM),
14 Novosibirsk, Russia. EDS analyses of minerals were done in high-vacuum modes at an
15 accelerating voltage of 20 kV, a probe current of 1 nA, and accumulation time of 20 second. The
16 following simple compounds and metals were used as reference standards for most of the elements:
17 SiO₂ (Si and O), Al₂O₃ (Al), diopside (Mg and Ca), Ca₂P₂O₇ (P), Cr₂O₃ (Cr), metallic Fe, Mn, Ni,
18 Zn, Cu and PGE. Correction for matrix effects was performed using the XPP algorithm,
19 implemented in the software of the microanalysis system. Metallic Co served for quantitative
20 optimization (normalization to probe current and energy calibration of the spectrometer).
21
22
23
24
25
26
27
28
29
30
31
32
33
34
35

36 **Laser Ablation ICP-MS Analysis of Elemental Abundances.**

37
38
39 One section of SG 009 was analyzed using an Elemental Scientific Lasers New Wave™
40 UP193FX excimer laser ablation system coupled to a Thermo Element XR™, inductively coupled
41 plasma mass spectrometer (LA-ICP-MS) at the Plasma Analytical Facility, Florida State
42 University. Analyzed points are represented on Fig. S1ab. The oxide production was set with
43 tuning the sample gas to yield ThO⁺/Th⁺ < 1 %. Metal and sulfide grains were measured with a 50
44 μm spot, at 50 Hz repetition rate and 10 seconds of ablation per spot following Humayun (2012).
45 Standards used were USGS silicate glasses GSC-1g, GSD-1g and GSE-1g, NIST SRM 1263a
46 steel, and the iron meteorites Hoba (IVB) and North Chile (Filomena, IIA). Silicate clasts were
47 measured with either spot, line or raster modes at 50 Hz repetition rate. Spots were taken with 100
48 μm spot size and 10 seconds of ablation per spot. Lines were taken with 50 μm spot size scanned
49
50
51
52
53
54
55
56
57
58
59
60

1
2
3 at 10 $\mu\text{m}/\text{second}$. Rasters were taken with 100 μm spot size scanned at 20 or 25 $\mu\text{m}/\text{second}$
4 covering areas of about 300 $\mu\text{m} \times 800 \mu\text{m}$. Major and trace element concentrations for silicates
5 were standardized with USGS silicate glasses GSC-1g, GSD-1g, BHVO-2g, BCR-2g and BIR-1g
6 (Humayun et al., 2010).
7
8
9

10 11 12 **Oxygen, Neon, Argon, Nitrogen and Carbon Isotopic Compositions** 13

14
15 A separate split of the metal-rich lithology, weighing ~ 50 mg, was used to measure bulk
16 oxygen, nitrogen and carbon isotopic compositions at the Open University. The sample was
17 crushed in an agate mortar and pestle. Oxygen isotopic compositions were determined in replicate
18 on ~ 2 mg aliquots of the partly homogenized sample by laser fluorination. The samples were
19 heated with a CO_2 laser (10.6 nm) in the presence of excess BrF_5 , the gas purified over hot KBr
20 and cryogenic traps and then analyzed on a PRISM III mass spectrometer (VG Isogas Ltd).
21 Analytical precision is $\sim \pm 0.8$ ‰ and ± 1.6 ‰ (2σ) for $\delta^{17}\text{O}$ and $\delta^{18}\text{O}$ respectively, providing a
22 precision of $\sim \pm 1.7$ ‰ (2σ) for $\Delta^{17}\text{O}$. Details of the procedure are described by Miller et al. (1999).
23
24
25
26
27
28

29 Neon, argon, nitrogen and carbon isotopic compositions were determined simultaneously
30 using the Finesse mass-spectrometer system, a complex of three static mode mass-spectrometers
31 fed from a single extraction system (Wright et al. 1988; Wright and Pillinger 1989; Verchovsky et
32 al. 1998, Verchovsky 2017). The gases were extracted from the sample of SG 009 (13.44 mg) by
33 stepped combustion in the temperature range from 200 to 1400°C with 13 steps. The clean up
34 procedure of gases released by combustion and crushing methods was identical (Verchovsky et al.
35 1998, 2002). Typical system blank levels for stepped combustion were <10 ng of C and <1 ng of
36 N. Typical system blanks for ^{20}Ne were $<6.5 \times 10^{-10}$, and for ^{40}Ar and ^{36}Ar were $<8 \times 10^{-9}$ and
37 $<1.2 \times 10^{-10}$ (in cm^3 STP), respectively. The analytical precision is $\sim \pm 1\%$ for both $\delta^{13}\text{C}$ and $\delta^{15}\text{N}$
38 measurements. Uncertainties of absolute concentrations of gases are 5-10%, and elemental ratios
39 of noble gases are estimated to have an uncertainty of about 5%.
40
41
42
43
44
45
46
47
48
49

50 **SIMS Investigations of Oxygen Isotopes** 51

52
53 Oxygen isotope compositions in olivine, pyroxene and spinel were determined using the
54 Cameca IMS1280-HR ion microprobe at Heidelberg University (HIP). We used a 2 nA, 20 keV
55
56
57

1
2
3 Cs⁺ primary ion beam with a raster size of 10 μm (12 μm during pre-sputtering). Negative
4 secondary ions were accelerated to 10 keV. The secondary ion image was limited to 30 μm, the
5 dynamic transfer optical system (DTOS) was activated and sample charging was compensated
6 with the electron gun (NEG). ¹⁶O, ¹⁷O and ¹⁸O were detected simultaneously in three Faraday Cups.
7
8 The nominal mass resolving power for ¹⁶O and ¹⁸O was 2500 and 7000 for ¹⁷O. The contribution
9 of ¹⁶OH⁻ on the ¹⁷O peak was negligible at < 0.1%. Secondary intensities for ¹⁶O and ¹⁷O were
10 ~ 1.5 × 10⁹ cps and ~ 6 × 10⁵ cps, respectively. Prior to each analysis the secondary beam was
11 centered automatically in the field aperture (X and Y) and the entrance slit (X only). Including the
12 time for beam centering the analyses started after a total pre-sputtering time of 90 s and each
13 analysis had 20 cycles with 10 s integration time per cycle. The internal precision reported is the
14 standard deviation of the mean value of the isotope ratios. The baseline of the FC amplifiers was
15 determined with an integration time of 300 s at least three times per session.
16
17

18
19 San Carlos olivine (+2.69, +5.28), pyroxene (+3.09, +6.03) and Burma spinel (+14.77,
20 +28.09) were used as reference materials for calibration of the ol, px and sp analyses (values in
21 parentheses are δ¹⁷O and δ¹⁸O determined by laser fluorination mass spectrometry). The reference
22 minerals were on a separate sample holder and were analysed prior to and after each of the two
23 analytical sessions. The external repeatability (1σ) for δ¹⁷O, δ¹⁸O and Δ¹⁷O of these analyses was
24 0.4, 0.5 and 0.3 for ol, 0.4, 0.3 and 0.4 for px and 0.3, 0.7 and 0.4 for sp, respectively.
25
26

27
28 After the SIMS analyses reflected light images of the regions analysed were overlain with
29 EDX element mappings to check for mixed phase analyses and reject them (see Fig. S2 in the
30 electronic appendix).
31
32
33
34
35

36 37 38 39 40 41 42 43 44 45 46 47 48 49 50 51 52 53 54 55 56 57 58 59 60

Petrography and Mineralogy

The SG 009 meteorite consists of a silicate fraction represented by chondrules and their fragments, and Fe,Ni-metal nodules (23 vol%) (Fig. 1). The silicate fraction also includes 1-cm sized lithic fragments some of which have an achondritic texture.

Chondrules in SG 009 are commonly 400 μm to 1.2 mm in size (Fig. 2a-d). Some angular chondrule fragments are up to 2 mm in size. The silicate fraction is dominated by porphyritic

1
2
3 chondrules – porphyritic olivine (PO) or porphyritic pyroxene porphyritic (PP) chondrules – and
4 their fragments. Porphyritic olivine-pyroxene (POP) (Fig. 2a), barred olivine (BO), radial
5 pyroxene (RP), cryptocrystalline (C), glass-rich porphyritic, Al-rich (Fig. 2b) and SiO₂-rich
6 chondrules (Fig. 2c) are less common (1-2 chondrules of each type). Thus, most of the porphyritic
7 chondrules are either dominantly olivine or pyroxene and there is a lack of the porphyritic olivine-
8 pyroxene chondrules (POP) that dominate carbonaceous (Ebel et al., 2016) and ordinary chondrites
9 (Gooding and Keil, 1981, Kita et al. 2010). Several objects in SG 009 have chondrule textures but
10 are now clasts with irregular outlines and no evidence of once being spherical.

11
12 Mineral modes of SG 009 are (vol%) (Table 1): olivine - 5; low-Ca pyroxene - 40, Ca-
13 pyroxene - 4; glass (feldspathic) - 10; silica - 1; Fe,Ni-metal-(kamacite) 23; sulfide (mostly troilite
14 - 9 (troilite: daubréelite = 5:1), schreibersite - 3, magnesiochromite, anorthite, spinel, graphite,
15 and platinum group elements (PGE)-metal particles <1, weathering products and fine-grained
16 component ~ 5. Olivine abundance is lower than in ordinary chondrites. Mineral modes of SG 009
17 are mostly similar to those of NWA 5492 (Weisberg et al. 2012) with the exception of troilite
18 which is more abundant in SG 009 (Fig 1c), and magnesiochromite and (PGE)-metal particles
19 rarely occurring in the meteorite.

20
21 Silicates in some chondrules contain tiny blebs of metal suggestive of reduction of Fe from
22 silicates. One Al-rich chondrule (~ 500 µm in size) contains spinel, anorthite and Al,Ti-rich
23 diopside (Fig. 2b). It has an ideal round shape and clear boundaries with surrounding metal and
24 silicate material. Silica-bearing chondrules (Fig. 2c) have irregular outlines, porphyritic texture
25 and consist of SiO₂-phase and pyroxene. Adjacent to spinel from an Al-rich chondrule, Mg-
26 chromite was found in assemblage with daubréelite, troilite and Fe,Ni-metal.

27
28 Opaque assemblages are represented by intergrown daubréelite, troilite, schreibersite and
29 Fe,Ni-metal (Fig. 3ab). The Fe,Ni-metal in SG 009 occurs as ~600 µm diameter nodules or clusters
30 of nodules, interstitial to the chondrules, or together with sulfides as the mesostasis of some
31 chondrules (Fig. 2d). In one case a graphite vein cuts through metal grains (Fig. 2e). After etching,
32 kamacite demonstrates a polycrystalline structure (Fig. 2e) with equilibrium boundaries of grains
33 that indicates long-duration recrystallization at temperatures above 500° C. Tiny PGE-rich metal
34 particles (up to 5 µm) were observed mostly in intergrowths with schreibersite-daubréelite-troilite
35 assemblages surrounded by tiny secondary calcite grains and iron hydroxides, and in the silicate
36 material (Fig. 4ab).

1
2
3 While the metal abundance of SG 009 is similar to that of CH chondrites, the occurrence
4 of large metal clasts is texturally similar to CB chondrites and to GRO 95551 (Weisberg et al.
5 2001).
6
7

8 One fragment of 1 cm length and 0.4 cm width has an elliptical shape and achondritic
9 texture (Fig. 5). It is composed of irregularly distributed areas of fine-grained and medium-grained
10 texture. The fine-grained areas are composed of subhedral pyroxene crystals from 5 to 15 μm with
11 interstitial anhedral feldspar grains of the same size. Medium-grained areas are composed mostly
12 of 50-100 μm anhedral pyroxene with only minor 100 μm anhedral feldspar. Troilite is an
13 accessory phase with grains of irregular shape and average 10 μm in size. The modal mineral
14 composition (vol%) of the fine-grained area is: pyroxene 72.8; plagioclase 25.9; troilite 1.3;
15 medium-grained areas: pyroxene 79.8; plagioclase 17.6; oxides 2.7.
16
17

18 The meteorite shock stage is S2 (Stoffler et al. 1991) based on undulatory extinction and
19 absence of planar fractures in olivine grains, corresponding to shock pressure <10 GPa.
20
21
22

23 24 25 26 27 **Mineral Chemistry** 28

29
30
31 Olivines and pyroxenes in SG 009 are highly reduced compared to the mineral assemblages
32 of chondrules from carbonaceous or ordinary chondrites. The average composition of olivine
33 ($\text{Fa}_{0.47\pm 0.10}$) is similar to that of other G chondrites, NWA 5492 and GRO 95551. Olivine
34 composition is also similar to ECs ($\text{Fa}_{0.4}$) (Rubin 2010) more magnesian than olivine from CH-CB
35 chondrites (Fa_{2-4}) (Weisberg et al. 2001) and very different from more ferrous olivine from
36 ungrouped metal-rich chondrites NWA 12379/12273 (Jansen et al. 2019; Agee et al. 2019). Its
37 Cr_2O_3 and CaO contents are low like in NWA 5492 and GRO 95551 (Fig. 6, Table 2).
38
39

40
41 Average low-Ca pyroxene ($\text{Fs}_{1.42}$, $\text{Wo}_{0.88}$) with Fe/Mn ratio 2.83, is enstatite the
42 compositions of which are similar to those in other G chondrites, NWA 5492 and GRO 95551
43 (Weisberg et al. 2015), and ECs (Rubin 2010), and different from ungrouped metal-rich chondrites
44 NWA 12379/12273 (Jansen et al. 2019, Agee et al. 2019) (Table 3). Pyroxene is also represented
45 by diopside ($\text{Fs}_{1.34}$, $\text{Wo}_{47.32}$). FeO-rich low-Ca-pyroxene occurs in some chondrules ($\text{Fs}_{9.33-32.48}$,
46 $\text{Wo}_{0.23-4.74}$). Plagioclase varies in composition, $\text{An}_{32.28-95.04}$. Mesostasis in chondrules is enriched
47 in K_2O (3.83 - 9.18 wt%) and TiO_2 (1.22 - 6.53 wt%). MgO-chromite is almost pure MgO-end
48
49
50
51
52
53
54
55
56
57

1
2
3 member, MgCr_2O_4 . Such chromite has not been described for any of the metal-rich chondrites
4 before.
5

6 The one Al-rich chondrule (Fig. 2b, S2b) contains spinel, plagioclase, olivine and
7 pyroxene. Pyroxene is represented by diopside ($\text{Fs}_{0.4-0.8}$, $\text{Wo}_{47.1-50.2}$) enriched in Al_2O_3 (3.1-
8 3.2 wt.%) and TiO_2 (7.2-11.5 wt.%). Spinel is enriched in Cr_2O_3 (3.52 wt.%) (Table 3), while
9 plagioclase is almost pure anorthite (An_{98}).
10
11

12 Pyroxene in the clast with achondritic texture (Fig. 5) is also very reduced ($\text{En}_{96.8\pm 1.19}$
13 $\text{Wo}_{0.5\pm 0.09}$), and minor pyroxene has composition: $\text{En}_{45.5\pm 1.72}$ $\text{Wo}_{44.1\pm 1.48}$. The low-Ca pyroxene
14 contains Cr_2O_3 0.15 ± 0.04 , $\text{Fe}/\text{Mn}=10.5\pm 7.3$ (at.). The CaO-rich pyroxene is TiO_2 -, Cr_2O_3 - and
15 Na_2O - bearing (TiO_2 0.33 ± 0.03 ; Cr_2O_3 0.53 ± 0.09 ; Na_2O 0.41 ± 0.02 wt%). Feldspar composition
16 is: $\text{Ab}_{74.2}$ $\text{An}_{18.2}$ with 1.55 wt.% FeO.
17
18
19
20
21

22 Metal in SG 009 is fairly uniform in composition. Average metal composition (in wt%) is
23 4.99 ± 0.23 Ni, 0.44 ± 0.02 Co, and the metal contains less than 0.03 Si, P, and Cr. The high-Ni
24 metal in SG 009 contains (in wt%) 32.3 Ni, and 0.25 Co. The low-Ni metal does not have solar
25 Ni/Co ratio that is common in CH and CB chondrites. It is closer in composition to that of NWA
26 5492, than to GRO 95551 (Weisberg et al. 2012) (Fig. 7).
27
28
29
30

31 Sulfides are represented by Cr-rich troilite (up to 2.4 wt%) and daubréelite which is
32 enriched in Mn (up to 2.2 wt.%) (Table 4). We did not observe alabandite, which was reported by
33 Friend et al. (2011) in the G - chondrite NWA 5492. Alabandite was described in E chondrites and
34 in one inclusion from the Ghubara L chondrite (Ivanova et al. 2001). Schreibersite is homogeneous
35 in composition.
36
37
38

39 Representative platinum group element (PGE) enriched metal inclusion compositions are
40 given in Table 5. PGE-enriched Fe,Ni-metal particles are mostly enriched in Pt, Ru, Os and Ir.
41 These particles have homogeneous (particle # 3, 46, and 1554) and heterogeneous (particles #31
42 and 4520) chemical compositions. As shown in Table 5, the average compositions of different
43 particles vary in a wide range (particle #46 and 1554), as well as compositions inside particles
44 (particles #31 and 4520). Contents of Pt, Os, Ir and Ru in Fe,Ni-metal particles vary in a wide
45 range (in wt.%): Pt 1.79 – 27.6; Os 0.10 – 4.78; Ir 0.39 – 7.33; Ru 1.55 – 10.6; Pd up to 0.28. These
46 compositions are distinct from those of fremdlinge observed in CAIs (e.g. Hewins et al. 2014) and
47 of PGE particles found in R chondrites (Schulze 2007).
48
49
50
51
52
53
54
55
56
57
58
59
60

Siderophile and Chalcophile Element Geochemistry of Metal and Sulfides from Sierra Gorda 009

Results for 28 metal nodules and six sulfide grains from SG 009 analyzed by LA-ICP-MS are given in Tables 6 and 7 and shown in Fig. 8. Preliminary results were reported earlier in Ivanova et al. (2019). The locations of all analytical points are shown in the BSE image (Fig. S1ab), and the numbers shown in the BSE image (Fig. S1ab) correspond to those marked in the Tables 6-7. The elements V (1 ppm), Cr (6 ppm), Mn (1 ppm) and Sb (0.2 ppm) were below detection limits in all but one metal nodule, 127-G, that had 23 ppm Cr and 1 ppm V. Neither Nb nor Ta was found in metal.

The average metal composition of the SG 009 metal is a good match to that of the metal in NWA 5492 and GRO 95511 and differs from average metal compositions of equilibrated H chondrite, CR, and CB_b chondrites (Fig. 8). One important difference is that the SG 009 metal has a wide range of compositions (e.g., an order of magnitude variation) among the compatible elements (Re, Os, Ir, Pt, Ru) compared to the metal of NWA 5492 G-chondrite, which exhibits a narrow range ($\pm 10\%$) in the compatible elements (Fig. 8).

The abundances of the volatile elements, Ga (16 ppm vs. 15 ppm), Ge (26 ppm vs. 26 ppm), Au (0.61 ppm vs. 0.67 ppm) and Sn (0.4 ppm vs. 0.5 ppm) overlap within analytical error between the metal of SG 009 and NWA 5492. Antimony abundances were below detection limits in NWA 5492 metal (< 0.2 ppm) but consistent with the 0.12 ppm observed in SG 009 metal. Abundances for As (4.0 ppm vs. 4.8 ppm) are also similar between the metals of the two chondrites. The Cu abundances differ more substantially (37 ppm vs. 54 ppm). Other diagnostic features include the (Ni/Co)_{CI} ratio that is identical between the two chondrites (0.75 vs. 0.76) and lower than that of carbonaceous chondrites. The metal of the G chondrites is higher in volatile element abundances than that of CB or CR chondrites by an order of magnitude or more (Fig. 8).

In several sulfides from SG 009, strong enrichment of V, Cr and Nb compared to CI compositions (Table 7) was observed in SG 009 (sulfides were not measured in NWA 5492). Vanadium is higher in the sulfides (500-1100 ppm) than in the silicates (< 100 ppm). Similarly, Cr is higher in the sulfides (3-7 wt. %) than in the silicates (0.05-0.5 wt. %). Niobium contents in sulfides (~ 0.6 ppm) are higher than those in silicates of SG 009. Tantalum is generally lower in the sulfides (< 0.002 ppm) with one exception, relative to the silicates (0.009-0.060 ppm).

Lithophile Element Geochemistry of Silicates in Chondrules from Sierra Gorda 009

All spots, lines and rasters measurements taken on the silicate chondrules of SG 009 are shown on Fig. S1ab. Rasters over the analyzed areas that were 400 μm or more in diameter are generally more representative of bulk compositions of the chondrule fragments than spot analyses, and results are represented in Table 7. Average data of the fragments correspond to a mixture of pyroxene, olivine and plagioclase/glass compositions. The REE patterns have strong anomalies (Fig. 9). In addition to Eu anomalies, REEs show anomalies in Ce (all positive), that might be suspect for desert meteorites or might be cosmochemical in origin; in Yb, mainly positive, which is almost certainly a cosmochemical signal of volatilization in a reducing gas.

Other evidence for a reducing environment is provided by subchondritic Nb/Ta ratios in silicates, where Nb has acted like a chalcophile element. As mentioned above, sulfides have strong enrichments in V, Cr and Nb compared to silicates (Table 7) corroborating the evidence of Nb depletion observed in the silicates. The complementary relationship between Nb in silicates and sulfides indicates that the metal, sulfide and silicate clasts were all processed together in the same impact event. We observed strong fractionation of the Th/Sc ratio, immune to volatility, but sensitive to igneous processes, though there are no correlations between Sc and Sr or CaO and Al_2O_3 that might indicate that the Th/Sc variations are simple mixtures of pyroxene and feldspathic glass. Accordingly, it is suspected that the various silicate clasts might have igneous precursors, similar to what was observed by Oulton et al. (2016) in the study of Gujba silicate clasts. This would support our observation in the metals (see below).

Oxygen Isotopic Compositions of Sierra Gorda 009 and Its Minerals

Bulk oxygen isotopic composition of SG 009 silicates obtained at Open University (in ‰) is $\delta^{17}\text{O}$ 3.763, 3.736; $\delta^{18}\text{O}$ 6.263, 6.169; $\Delta^{17}\text{O}$ 0.506, 0.528 ‰) (Fig. 10). These values are different with CH/CB carbonaceous chondrites (e.g., Isheyevo (Ivanova et al. 2008)), but plot intermediate between ordinary and enstatite chondrites in the three oxygen isotope diagram (Fig. 10). The oxygen isotopic composition is on a line with other metal-rich chondrites NWA 5492 and GRO 95551, described by Weisberg et al. (2015), and very close to HH chondrite Burnwell (Russell et

1
2
3 al. 1998). However, it is different from the very metal-rich chondrites NWA 12379/12273 oxygen
4 compositions, whose silicates have affinities to L/LL chondrites.
5

6
7 Oxygen isotopic compositions of SG 009 minerals were also analyzed by ion probe at
8 Heidelberg University. Fig. S2ab shows the thin section areas where analyses were performed.
9
10 These measurements comprised various olivine and pyroxene crystals, and spinel and olivine from
11 a single Al-rich chondrule (Fig. S2c). Results are presented in Table 8 and Fig. 11.
12

13
14 The majority of oxygen isotopic composition data of individual SG 009 minerals are
15 similar to the two other G-chondrites NWA 5492 and GRO 95551 as represented by mean values
16 of olivine and pyroxene of ion probe data by Weisberg et al. (2012, 2015) in Fig. 11, and
17 representative of the bulk oxygen isotopic composition of G chondrites (Fig. 10). However,
18 individual spinel and olivine from the Al-rich chondrule display values below the terrestrial
19 fractionation line indicating the same heterogeneity of oxygen isotopic compositions as found by
20 Weisberg et al. (2012) for barred silicate clasts (Fig. 10) and Weisberg et al. (2015) for olivine in
21 another Al-rich chondrule (Fig. 11). This heterogeneity may be related to refractory precursors of
22 Al-rich chondrules, which has been also concluded by Maruyama et al. (1999) who found extreme
23 ^{16}O enrichments for spinel grains in two Allende (CV3) chondrules.
24
25
26
27
28
29
30
31

32 **Noble Gas, Carbon and Nitrogen Abundances and Isotopic Compositions, Cosmic Ray** 33 **Exposure (CRE) Age of Sierra Gorda 009.** 34 35 36

37 Detailed stepwise combustion results for noble gas, carbon and nitrogen abundances and
38 isotopic compositions of SG 009 are listed in Table 9.
39

40
41 ^{20}Ne , ^{36}Ar and ^{40}Ar contents are 28.3, 18.2 and 3987.8 ($\times 10^{-7}$ cm³ STP/g), respectively. Ne
42 isotopes data points form a trend reflecting a mixture of solar wind and the cosmogenic component.
43
44 The contribution from cosmogenic neon is more pronounced at the late combustion steps (Fig. 12).
45 The low temperature steps of SG 009 having weathering grade W2 show terrestrial Ar
46 contamination typical of desert meteorites (Fig. 13) (Korochantseva et al. 2005). $^{40}\text{Ar}/^{36}\text{Ar}$ ratios
47 of temperature steps $\geq 700^\circ\text{C}$ (except for 1100°C) are constant (53-56) and characterize the argon
48 isotopic composition of this meteorite without atmospheric contamination (Fig. 13).
49
50
51

52
53 The C and N abundances of the step-combusted SG 009 are 1628 and 61 ppm, respectively.
54 Bulk $\delta^{13}\text{C}$ (+1.6 ‰) (Fig. 14) and $\delta^{15}\text{N}$ (+14.4 ‰) (Fig. 15) are in the range observed for EH
55
56
57
58
59
60

1
2
3 chondrites and OCs, respectively (Table 10). Note that low temperature steps are possibly
4 contaminated by terrestrial carbon and nitrogen (as in the case of argon) that can influence on
5 average C and N contents and isotopic compositions.
6
7

8 The concentration of cosmogenic ^{21}Ne is 6.93×10^{-8} cm³ STP/g comprising 97.0 % of
9 $^{21}\text{Ne}_{\text{total}}$ and calculated using the endmember compositions of SW Ne with $^{20}\text{Ne}/^{22}\text{Ne}=13.78$ and
10 $^{21}\text{Ne}/^{22}\text{Ne}=0.0329$ (Heber et al. 2009) and cosmogenic Ne with $^{20}\text{Ne}/^{22}\text{Ne}=0.8$ (Eugster and Michel
11 1995) and $^{21}\text{Ne}/^{22}\text{Ne}=0.90$ (see the caption of Fig. 12). The minimum CRE age of 24 Ma was
12 calculated for SG 009 from the maximum P_{21} of 0.29×10^{-8} cc/gMa for the meteoroid with radius
13 of 40-50 cm by the model of Leya and Masarik (2009) and the bulk composition of chondrite
14 calculated from mineral composition and modes. For comparison, metal-rich carbonaceous
15 chondrites Isheyevo (CH/CB_b) and Bencubbin (CB_a) have CRE ages of 34 Ma and 39 ± 3 Ma,
16 respectively, some CH chondrites have rather young CREs (HaH 237 [CB_b] 3 Ma; PAT 91546
17 [CH] >8 Ma; PCA 92468 [CH] 4.3 Ma; RKP 02435 [CH] 1.5 Ma; Weber et al. 2001). The CRE
18 age of SG 009 is usual for O, E and R chondrites having the range up to 50-80 Ma and close to
19 carbonaceous chondrites (Wieler et al. 2002).
20
21
22
23
24
25
26
27
28
29
30

31 DISCUSSION

32 33 34 A New Grouplet of G-chondrites

35
36
37 SG 009 is a new metal-rich chondrite breccia **which has characteristics similar to those of**
38 **other metal-rich** chondrites NWA 5492 and GRO 95551. Weisberg et al. (2015) distinguished
39 these as a new grouplet of G-chondrites named from the first found meteorite of this grouplet,
40 GRO 95551. SG 009 is here identified as the third member of the G-chondrites (GCs). Matrix is
41 absent in all three GCs similar to other metal-rich chondrites including CH-CB and NWA
42 12379/12273 meteorites. Like other GCs, SG 009 does not contain matrix lumps that occur in CH-
43 CB chondrites and there is no matrix material interstitial to the chondrules and metal. G-chondrites
44 contain PO, PP, POP, BO, RP, Al-rich and SiO₂-rich chondrules, with PP chondrules being
45 strongly predominant. No refractory inclusions have been observed in any G chondrites.
46
47
48
49
50
51
52

53 SG 009 and the two other G-type meteorites are characterized by a high content of metal
54 (>20 vol%) like CH chondrites, more than in ordinary (OC) and enstatite (EC) chondrites (5-15
55
56
57

1
2
3 vol%), HH and low-FeO ordinary chondrites (Russell et al. 1998, Troiano et al., 2011), but less
4 than in CB chondrites (up to 70 vol%) and ungrouped metal-rich chondrites NWA 12379/12273
5 (~64 vol%) (Jansen et al. 2019; Agee et al. 2019). Fe,Ni-metal in SG 009 is similar to that of NWA
6 5492 in Ni and Co contents, but differs from that of GRO 95551 having both high-Ni and low-Ni
7 metal (Weisberg et al. 2015). None of the G chondrites have solar Co/Ni ratios unlike CH-CB
8 chondrites (Fig. 7), and the Si, Cr, and P contents of the metal are low (below our electron probe
9 detection limit of 0.03 wt%), unlike metal in enstatite chondrites (e.g., Keil, 1968) (Table 4). G
10 chondrites do not contain any zoned Fe,Ni - metal like that in the CH and CBb chondrites.

11
12
13
14
15
16
17 Among the G chondrites only SG 009 contains PGE metal inclusions that were not
18 described in NWA 5492 or in GRO 95551. The PGE nuggets may be products of transformation
19 of primary refractory material similar to metal nuggets in CVs or be products of metal oxidization
20 (e.g., Blum et al., 1989). The fact that PGE metal particles are surrounded by calcite may indicate
21 that this oxidization took place in the desert rather than being intrinsic to the meteorite.

22
23
24
25
26 Sulfides are more abundant in G-chondrites than in CHs and CBs, but all GCs have a
27 sulfide assemblage (daubréelite, rare alabandite and Cr-troilite) distinct from that of ECs,
28 oldhamite, alabandite, niningerite or any of the other unusual sulfides typical of E chondrites (e.g.,
29 Keil 1968). The FeO/MnO ratio in enstatite of G chondrites (2.83) compared with the FeO/MnO
30 ratio in enstatite of E chondrites in which MnO, Cr₂O₃ and TiO₂ contents are below a microprobe
31 detection limits (van Niekirk et al. 2014) that may indicate incomplete reduction of Mn, Cr, and
32 Ti in G chondrites in comparison with E chondrites.

33
34
35
36
37
38 The silicate compositions of SG 009 are very reduced and similar to those of other GCs
39 (Weisberg et al. 2015) and EHs, and they are more reduced than those of CH-CB chondrites (Fa2-
40 4), any other types of ordinary chondrites, HH chondrites (Russell et al. 1998, Troiano et al., 2011),
41 and the metal-rich ungrouped NWA 12379/12273 which have olivine composition like that in
42 L/LL chondrites (Jansen et al. 2019).

43
44
45
46
47 All GCs have plagioclase with variable compositions (Table 3) compared to ordinary and
48 enstatite chondrites and NWA 12379/12273 very sodic plagioclase, and compared to CH-CB
49 plagioclase of anorthitic composition. This may indicate selective evaporation of sodium from the
50 melt during impact events. Glasses in chondrule mesostasis of all G chondrites are enriched in
51 K₂O, TiO₂, CaO and Na₂O, and the metal enriched mesostasis was also observed in NWA 5492.
52 Troilite-bearing mesostasis instead of glassy mesostasis was mentioned to be present in NWA
53
54
55
56
57

1
2
3 5492 (Weisberg et al. 2012). The metal and sulfide rich mesostasis in some chondrules indicate
4 that these chondrules may form by melting of sulfide and metal-rich precursors. These precursors
5 may in turn be formed in a sulfur-bearing vapor.
6
7

8 Among chromite-spinel minerals Mg-chromite was described only in SG 009; in other G
9 chondrites, NWA 5492 and GRO 95551, chromite was not observed, and all chromium-rich
10 minerals were sulfides - daubreelite and Cr-rich troilite which are typical minerals of E chondrites.
11 In all GCs, the spinel in Al-rich chondrules occurs together with anorthite, olivine and Ca-
12 pyroxene.
13
14
15
16

17 The G chondrites have variable degrees of shock stages, from S2 (SG 009, NWA 5492) to
18 S3 (NWA 5492 and GRO 95551) based on olivine extinction and presence or absence of planar
19 fractures (Stoffler et al. 1991). In NWA 5492 section pyroxene coexisting with olivine is darkened
20 due to inclusions of metal and sulfides (Weisberg et al., 2015). Such silicate darkening may be
21 interpreted as evidence of a moderate degree of shock, and post-shock annealing could have healed
22 the shock features of olivine (e.g., Rubin, 2004). Alternatively, the darkening in the pyroxene may
23 be a result of reduction instead of shock effects.
24
25
26
27
28

29 Bulk oxygen isotopic compositions of all G chondrites show a range of $\Delta^{17}\text{O} > 0$, and are
30 plotted between values for ordinary chondrites and enstatite chondrites in the three-oxygen isotope
31 diagram. The oxygen isotopic compositions of most chondrules and silicate clasts in the G
32 chondrites overlap with chondrules from EH3, LL3 and R3 chondrules (Fig. 10-11).
33
34
35

36 Oxygen isotopic compositions of olivine and pyroxene from SG 009 also plot between EHs
37 and OCs. However, we observed heterogeneity in oxygen isotopic compositions among spinel and
38 olivine of the Al-rich chondrule and of the olivine-pyroxene chondrules, similar to barred silicate
39 clasts (Weisberg et al. 2012) and Allende spinel rich chondrules (Maruyama et al. 1999). The
40 spread of the SG 009 data above and below the mass-dependent fractionation line (Fig. 11) can be
41 explained by mixing of material from different oxygen reservoirs and by exchange of oxygen
42 isotopes during melting and crystallization. The precursor of the Al-rich chondrule was probably
43 a CAI with oxygen isotopic composition typical for refractory inclusions (^{16}O –enriched). During
44 melting, evaporation and isotopic exchange with oxygen between different reservoirs, the primary
45 oxygen isotope compositions were shifted, as a result of it, formed the observed range of $\Delta^{17}\text{O}$
46 values.
47
48
49
50
51
52
53
54
55
56
57
58
59
60

1
2
3 The affinity of SG 009 to E and O chondrites is supported by bulk carbon and nitrogen
4 isotopic data – they have affinity to E and OC chondrites (Grady and Wright 2003). Neon isotopic
5 data reflect a mixture of cosmogenic and solar components but do not prove helpful in
6 discriminating the variable provenances of components in SG 009. Domination of solar but not
7 planetary noble gases indicates that the analysed sample has been exposed to solar wind on the
8 surface of the parent body. The cosmic ray exposure age of SG 009 is typical for O, E, and R
9 chondrites.

16 17 **Metal and Silicate Geochemistry of G Chondrites.**

18
19 The average metal composition of SG 009 in general is in a good agreement with that of
20 the metal in NWA 5492 (Weisberg et al. 2015) and GRO 95551 (Campbell and Humayun, 2003)
21 although the GRO 95551 metal is represented by both high-Ni and low-Ni metal (Weisberg et al.
22 2001). However, there are important differences between the SG 009 metal and NWA 5492 and
23 GRO 95551 metal – SG 009 metal shows a wide range of compatible element abundance (Re, Os,
24 Ir, Pt, Ru) (Fig. 8). This may imply that the metal underwent some fractionation, and that we are
25 dealing with differently modified metal particles at surface conditions or in outer space due to
26 several possibilities: sulfidization, partial melting of the metal, and/or formation of small pools of
27 shock melt which crystallized relatively quickly that resulted in a wide spread in siderophile
28 element compositions.

29
30 Unlike metal from carbonaceous chondrites, CR, and CH-CB, SG 009 and other G
31 chondrites, NWA 5492 and GRO 95551, have a fractionated refractory siderophile element
32 patterns similar to those in H chondrite (Kong and Ebihara, 1997; Teplyakova et al., 2012) that
33 lacks the oxidation losses of Fe, Ni and Co observed in H4-6 chondrite metal due to more intense
34 reduction in SG 009 metal. The G chondrite metal has siderophile element abundances that are
35 similar to H chondrite bulk composition with the exception of Mo, Ni, Pd, Au and As whose
36 concentrations are higher than for other siderophiles (Fig. 8). The G chondrite metal does not show
37 the enrichments of Au and As observed in EH and EL metal (Kong et al. 1997) but has chondritic
38 Au/Ni ratio unlike CR, CH and CB metal (which have sub-chondritic Au/Ni ratios). As is seen on
39 a plot of As vs. Au (Fig. 16) the SG 009 metal has chondritic composition unlike IIIAB, IVA, and
40 IIAB irons. Ir and Os correlation in metal of SG 009 compared with IVB, and metal of NWA 5492,
41 G-chondrite also indicates chondritic composition (Fig. 17).

1
2
3 Therefore, metal from G chondrites could derive from the H chondrite bulk composition
4 under a higher degree of reduction than the ordinary chondrite metal experienced. A plot of W/Ni
5 (CI) versus Fe/Ni (CI) (Fig. 18) shows this degree of reduction of G chondrite metal. On this plot,
6 bulk H chondrite metal plots at a high W/Ni (CI) ratio with a chondritic Fe/Ni (CI) ratio. Metal
7 from unequilibrated and equilibrated LL, L, H (Kong and Ebihara 1997), EL and EH (Kong et al.
8 1997) metal plot along a W-Fe trend towards the bulk H chondrite composition trend. Metal
9 compositions from SG 009 display variable W/Ni (CI) composition at constant Fe/Ni(CI)
10 composition, exhibiting both higher and lower W/Ni(CI) ratio relative to the chondritic ratio, while
11 NWA 5492 metal clusters (Weisberg et al. 2015) around the chondritic value (Fig. 18). Thermal
12 re-equilibration may have caused the (W/Ni) (CI) ratio to increase (Humayun and Campbell, 2002)
13 because W is less siderophile than Fe at $T < 1200$ K and a low metal-silicate ratio during re-
14 equilibration would result in a final W/Ni (CI) > 1 .
15
16
17
18
19
20
21
22
23

24 Rare earth element patterns (REEs) in chondrules of SG 009 reflect variable oxygen
25 fugacity environments during chondrule formation. The positive Ce anomaly is an indicator of
26 condensation from a vapor formed by evaporating silicates under oxidizing conditions. Such
27 oxidizing conditions are attained during evaporation of silicates, for example, in vacuum (Wang
28 et al., 2001), although low-pressure nebular environments with high dust-to-gas ratios probably
29 suffice.
30
31
32
33

34 The negative Eu and Yb may record volatilization in a gas in reducing conditions more
35 typical of nebular environments. Evidence for a highly reducing environment experienced by SG
36 009 chondrules is provided by the subchondritic Nb/Ta ratios (9.2 in average, compare to 17.3 in
37 CI) in the silicates where Nb has acted like a chalcophile element, with high concentrations in SG
38 009 sulfides. Using the equilibrium $\text{Fe} + \text{FeSiO}_3 + 0.5 \text{O}_2 = \text{Fe}_2\text{SiO}_4$, the SG 009 metal, olivine,
39 and orthopyroxene compositions, and assuming a temperature of 1273 K, we calculated $\log f\text{O}_2 =$
40 -18.2 , which relative to the IW buffer is -3.29 , indicating highly reduced formation condition of
41 this material (Fig. 19). This low ΔIW value is similar to the other G chondrites and all are lower
42 than R chondrites, ordinary chondrites, reduced CR chondrites, and even slightly more reduced
43 than the primitive achondrites like the acapulcoites and lodranites (Fig. 19). The juxtaposition of
44 initially oxidizing conditions followed by reducing conditions, even extremely reducing
45 conditions, speaks to the formation of SG 009 chondrules within a chemical micro-environment.
46
47
48
49
50
51
52
53
54
55
56
57
58
59
60

1
2
3 Plausible conditions for such micro-environments include collapsing impact vapor plumes within
4 an envelope of hydrogen gas (Stewart et al., 2019).
5

6
7 Large variations in Nb/Ta ratio may also indicate sulfidization. If sulfidization took place
8 the melt from which silicate chondrules were formed have reacted with vapor or fluid enriched in
9 sulfur. The metal- and sulfide- enriched mesostasis in some chondrules may be evidence of such
10 a process, as well as chalcophile behavior of Nb concentrated in SG 009 sulfides. Possible
11 differentiated precursors of SG 009 silicates could be evaluated with elemental ratios.
12
13
14

15 Ratios of Zr, Nb, Hf and Ta should remain constant during volatilization or recondensation.
16 Munker et al. (2003) have shown that different planets are characterized by a wide range in Zr/Hf
17 and Nb/Ta ratio because of the larger incompatibility of Nb relative to Ta and of Zr relative to Hf
18 during partial melting of planetary mantles. In Fig. 20, the Nb/Ta ratios vs. Zr/Hf ratios for some
19 of the SG 009 silicates are compared with the Gujba clasts (Oulton et al. 2016) and with planetary
20 basalt compositions from Munker et al. (2003). The SG 009 silicates have Nb/Ta ratios: 3-23,
21 Gujba clasts: 14-21, eucrite: 17-20, Martian meteorites: 13-21 and lunar basalt: 12-23. The Zr/Hf
22 ratios in SG 009 silicates: 22-40, in Gujba clasts: 29-41, eucrite: 34-35, Martian meteorites: 23-
23 34, and lunar basalts: 27-41. While the large range in Nb/Ta ratios represents extreme reduction
24 and sulfidation, the variation in Zr/Hf ratios is likely to reflect processes that affected the
25 precursors to SG 009.
26
27
28
29
30
31
32
33

34 We also observed fractionation of the Th/Sc ratio (0.001 – 0.006, compared to 0.005 in CI)
35 possibly indicating igneous processing in the chondrule precursors. During evaporation processes
36 Th and Sc are not fractionated from each other. In contrast Th is partitioning into melt since it is
37 much more incompatible than Sc. Thus, the SG 009 chondrules may contain a contribution from
38 melting and differentiated crust similar to basalts from the Moon, Mars and the Earth Munker et
39 al. (2003). However, given oxygen isotopic compositions between O and E chondrites and absence
40 of any traces of differentiated clasts it is difficult to imagine a big differentiated asteroid as a parent
41 body of G chondrites, but we do not exclude such a possibility for the G chondrite initial parent
42 body.
43
44
45
46
47
48
49
50

51 **Origin of Sierra Gorda 009 and Other G Chondrites**

52
53
54
55
56
57

1
2
3 The most important observation distinguishing G chondrites (SG 009, NWA 5492 and
4 GRO 95551) from O, E and R chondrites is a lack of matrix. The matrix abundance is an important
5 characteristic of all types of chondrites for understanding the origin and evolution of chondrites.
6 Besides G chondrites, no matrix was observed in the ungrouped metal-rich chondrites NWA 12379
7 and 12273 (Jansen et al., 2019, Agee et al., 2019) nor in metal-rich carbonaceous chondrites, CH-
8 CB groups (Weisberg et al. 1995b). Therefore, our observation shows that chondritic materials
9 with a metal abundance of >20-22% do not contain any fine-grained matrix, only matrix lumps
10 were preserved. Instead of the matrix all silicate objects are embedded in metal or are surrounded
11 by metal in these meteorites. The cause of this relationship between the abundance of metal and
12 the lack of matrix is not clear. We can only propose that the fine - grained matrix did not survive
13 during the processes of formation of G chondrites and the metal phase was predominant in the
14 region of the G chondrites formation.
15

16
17
18
19
20
21
22
23
24 There are other interpretations for the lack of matrix in the metal-rich chondrites. Meibom
25 et al. (2005) reported the FeO - rich composition of the impact in CB chondrites and hypothesized
26 that it may have originally been chondrite matrix that was melted during impact heating. The
27 presence of matrix-like material as dark inclusions (lumps) in the CH and CBb chondrites could
28 be interpreted as clumps of dust that aggregated together with other components and was not
29 dispersed interstitial to the chondrules. However, SG 009 demonstrates minor shock features
30 corresponding to S2 shock stage and it does not contain any traces of impact melt and fine-grained
31 matrix lumps unlike CH and CB chondrites. The lack of matrix could also indicate that the
32 chondrule formation mechanism was more efficient in this region of the disk, because a wide
33 variation in matrix abundances among chondrite groups is observed.
34
35

36
37
38
39
40
41 The lack of matrix in the G chondrites may result from similar processes that explain the
42 lack of matrix for CB chondrites but are derived of material from isotopically different oxygen
43 reservoirs. The lack of matrix could indicate a rapid hot accretion as was suggested by Metzler
44 (2012) or formation of G chondrites from an impact vapor plume produced by collision of
45 planetesimals (Stewart et al. 2019). Based on a new physical model for the formation of chondrules
46 and chondrites, mutual collisions between dynamically coexisting planetesimals produce impact
47 vapor plumes that collapse and concentrate a size-sorted mixture of chondrules and dust. The warm
48 cloud of shock-heated gas, dust, and chondrules is a dynamical and thermal anomaly in the nebula
49 with characteristics that assist with new planetesimal formation. Then, condensates from vapor
50
51
52
53
54
55
56
57

1
2
3 made by impacts between metal-, silicate-rich bodies accreted together (Fedkin et al. 2015).
4 During rapid hot accretion the dust was evaporated. The young age of chondrules from CB
5 chondrites supports this hypothesis (Krot et al. 2005). If this scenario is accurate chondrules from
6 G chondrites should also have a young age. Based on metal and silicate geochemistry
7 demonstrating fractionations of trace elements shown above, we can propose that one of the
8 colliding bodies, a precursors of G chondrites, might have been partly differentiated.
9

10
11
12
13 In the case of the formation of SG 009, unlike other G chondrites, besides the absence of
14 matrix fractionation of silicate and metal compositions, the presence of chromium in the oxidized
15 (Mg-chromite) and sulfide phases (daubréelite and Cr-troilite), graphite veins in Fe,Ni-metal,
16 achondritic clasts and chondrule-like objects may indicate a mixture of oxidized and reduced,
17 primitive and fractionated material, formed in oxygen isotopic reservoir between O and E
18 chondrites as well as carbon and nitrogen isotopes. Weisberg et al. (2015) noted a close
19 relationship between O, E, R and G chondrites which were formed inside the snow line in
20 comparison with C chondrites (Weisberg et al. 2015). However, unlike other G chondrites, SG 009
21 may preserve traces of oxidizing and reducing material in the final accretion of the G-chondrite
22 parent body.
23
24
25
26
27
28
29

30
31 Thus, G chondrites have unique characteristics and unique processes of their formation
32 resulted in the lack of matrices and enrichment of Fe,Ni-metal phase. The oxygen isotopic
33 compositions plot near the terrestrial fractionation line, a lack of any traces of aqueous alteration,
34 and carbon and nitrogen isotopic evidence of mixing between O and E reservoirs suggest formation
35 of the G chondrites in the inner Solar System.
36
37
38
39

40 41 CONCLUSIONS 42 43

44
45 The meteorites Sierra Gorda 009, North West Africa 5492 and Grosvenor Mountain 95551
46 represent a new grouplet of metal-rich (>21% of metal) chondrites, the G chondrites (named from
47 the first member, Grosvenor Mountain 95551), that are not related to CH or CB chondrites based
48 on bulk oxygen, carbon, nitrogen isotopic compositions, mineralogy and siderophile and lithophile
49 geochemistry. The silicates are very reduced in composition. **However**, rare oxidized mineral
50 phases occur (Mg-chromite, FeO-rich pyroxene). Sulfides are more abundant in G chondrites than
51
52
53
54
55
56
57
58
59
60

1
2
3 in CH-CB chondrites. SG 009 contains PGE inclusions, unlike NWA 5492 and GRO 95551, that
4 may be connected with oxidation of Fe,Ni-metal or represent remnants of refractory material.
5

6
7 None of the G chondrites contain fine-grained matrix or any matrix lumps enclosing
8 hydrated material similar to matrix lumps in CH-CB chondrites. Average compositions of metal
9 in G chondrites is similar to H chondrite metal, albeit formed in a more reducing environment.
10

11
12 Siderophile and lithophile geochemistry indicates sulfurization during G chondrites
13 formation, and fractionation caused by igneous process of some metal and silicate precursors. The
14 low ΔIW value during SG 009 chondrule formation is similar to the other G chondrites.
15

16
17 Oxygen of all G chondrites shows a range of isotopic compositions. Most have
18 $\Delta^{17}O > 0$ ‰ sandwiched between the bulk enstatite and ordinary chondrites. NWA 5492 and GRO
19 95551 oxygen compositions demonstrated a small contribution of R chondrite-like material
20 (Weisberg et al. 2015). An Al-rich chondrule from SG 009 has $\Delta^{17}O < 0$ ‰ that indicates some
21 heterogeneity in the oxygen isotopic composition of the G chondrite components and contribution
22 of refractory material.
23

24
25 Bulk carbon and nitrogen isotopic compositions of SG 009 correspond to EH and O
26 chondrites. Neon and argon isotopic data reflect a mixture of cosmogenic and solar components.
27 The presence of solar gases suggests exposure to solar wind at the surface of the parent body. The
28 cosmic ray exposure age determined from the concentration of cosmogenic ^{21}Ne is ≥ 24 Ma is
29 typical for O, E, and R chondrites. G chondrites have a relationship with O, E, and R chondrites,
30 and they all represent closely related Solar System material (Weisberg et al.2015). They may
31 represent a unique metal-rich parent asteroid containing both the primitive material and
32 fractionated material from the inner Solar System.
33

34
35 The observed oxidizing and reducing conditions during the formation of the SG 009
36 components. indicates a chemical micro-environment. Plausible conditions for such micro-
37 environments, as an example, may include collapsing impact vapor plumes within an envelope of
38 hydrogen gas as a result of collision of planetesimals (Stewart et al., 2019).
39

40
41 *Acknowledgments* – We thank M. Weisberg, H. Downes, an anonymous reviewer, and
42 Associate Editor, C. Goodrich, for their thoughtful reviews which helped to improve this paper.
43 The authors thank Sasha Krot for very fruitful discussions. This work was supported by the
44 Russian Fond of Basic Research No. 20-05-00117A, by Klaus Tschira Stiftung gGmbH, by the
45 NASA Emerging Worlds program (80NSSC18K0595, MH), and we thank the National High
46
47
48
49
50
51
52
53
54
55
56
57

1
2
3 Magnetic Field Laboratory, which is supported by National Science Foundation Cooperative
4 Agreement No. DMR-1644779* and the State of Florida. This work was also supported by the
5 Project No. FEUZ-2020-0059 of the Ministry of Science and Higher Education of the Russian
6 Federation.
7
8
9

10 11 12 REFERENCES

- 13
14
15 Agee C. B., Vaci Z., Ziegler K., and Spilde M. N. 2019. Northwest Africa 12273: Unique
16 ungrouped metal-rich chondrite (abstract #1176) *50th Lunar and Planetary Science*
17 *Conference*.
18
19 Amelin Y. and Krot A. E. 2005. Young Pb-isotopic ages of chondrules in CB carbonaceous
20 chondrites. (abstract # 1247) *36th Lunar and Planetary Science Conference*.
21
22 Anders E. and Grevesse N. 1989. Abundances of the elements: Meteoritic and solar. *Geochimica*
23 *et Cosmochimica Acta* **53**:197–214.
24
25 Bischoff A., Geiger T., Palme H., Spettel., Schultz L., Scherer P., Loeken T., Bland P., Clayton
26 R.N., Mayeda T.K., Herpers U., Meltzow B., Michel R., Dittrich-Hannen B. 1994. Acfer
27 217 – a new member of the Rumuruti chondrite group (R) meteorites. *Meteoritics* **29**:264-
28 273.
29
30 Bollard J., Connelly J., and Bizzarro M. 2015. Pb-Pb dating of individual chondrules from the
31 CB_a chondrite Gujba: Assessment of the impact plume formation model. *Meteoritics and*
32 *Planetary Science* **50**:1197–1216.
33
34 Blum J. D., Wasserburg G. J., Hutcheon I. D., Beckett J. R., Stolper E. M. 1989.
35 Origin of opaque assemblages in C3V meteorites: Implications for nebular and planetary
36 processes. *Geochimica et Cosmochimica Acta* **53**: 543.
37
38 Campbell A. J., Humayun M., Krot A. and Keil K. 2001. Origin of zoned metal grains in the
39 QUE 94411 chondrite. *Geochimica et Cosmochimica Acta* **65**:163-180.
40
41 Campbell A. J., Humayun M. and Weisberg M. K. 2002. Siderophile element constraints on the
42 formation of metal in the metal-rich chondrites Bencubbin, Gujba and Weatherford.
43 *Geochimica et Cosmochimica Acta* **66**:647-660.
44
45 Campbell A., and Humayun M. 2003. Formation of metal in Grosvenor Mountains 95551 and
46 comparison to ordinary chondrites. *Geochimica et Cosmochimica Acta* **67**: 2481-2495.
47
48
49
50
51
52
53
54
55
56
57
58
59
60

- 1
2
3 Campbell A.J., and Humayun M. 2005. Composition of the group IVB iron meteorites and their
4 parent melt. *Geochimica et Cosmochimica Acta* **69**:4733-4744.
5
6 Clayton R. N., Mayeda T. K., and Rubin A. E. 1984. Oxygen isotopic compositions of enstatite
7 chondrites and aubrites. Proceedings, 15th Lunar and Planetary Science Conference,
8
9 *Journal of Geophysical Research* **B89**:C245–C249.
10
11 Clayton R.N., Mayeda T.K., Goswami J.N. and Olsen E.J. (1991) Oxygen isotope studies of
12 ordinary chondrites. *Geochimica et Cosmochim Acta* **55**: 2317-2337.
13
14 Connelly J.N., Bizzarro M., Krot A.N. Nordlunds A., Wielandt D., Ivanova M.A. 2012. The
15 absolute chronology and thermal processing of solids in the solar protoplanetary disk.
16
17 *Science*: **338**:651-655.
18
19 Ebel D., Brunner C., Konrad K., Leftwich K., Erb I., Lu M., Rodriguez H., Crapster-Pregont E.
20
21 J., Friedrich J. M., Weisberg M. K. 2016. Abundance, major element composition and size
22 of components and matrix in CV, CO and Acfer 094 chondrites. *Geochimica et*
23
24 *Cosmochimica Acta* **172**:322-356.
25
26 Eberhardt P., Eugster O. and Marti K. 1965. A redetermination of the isotopic composition of
27 atmospheric neon. *Z. Naturforsch. Teil A* 20: 623–624.
28
29 Eugster O. and Michel Th. 1995. Common asteroid break-up events of eucrites, diogenites, and
30 howardites and cosmic-ray production rates for noble gases in achondrites. *Geochimica et*
31
32 *Cosmochimica Acta* **59**: 177-199.
33
34 Fedkin A. V., Grossman L., Humayun M., Simon S. B., and Campbell A. J. 2015. Condensates
35 from vapor made by impacts between metal-, silicate-rich bodies: Comparison with metal
36 and chondrules in CB chondrites. *Geochimica et Cosmochimica Acta* **164**:236–261.
37
38 Friend P., Zipfel J., Gellissen M., Kleinschrod R., Muenker C., Paek A., Schulz T., Stracke A.
39 and Palme H. 2011. Northwest Africa 5492: An extremely reduced chondritic meteorite
40 with low volatile element contents. (abstract #1095) *42nd Lunar and Planetary Science*
41
42 *Conference*.
43
44 Gooding J. L. and Keil K. 1981. Relative abundances of chondrule primary textural types in
45 ordinary chondrites and their bearing on conditions of chondrule formation. *Meteoritics*
46
47 **16**: 17-43.
48
49 Grady M. M. and Wright I. P. 2003. Elemental and isotopic abundances of carbon and
50 nitrogen in meteorites. *Space Science Review* **106**:231-248.
51
52
53
54
55
56
57
58
59
60

- 1
2
3 Heber V. S., Wieler R., Baur H., Olinger C., Friedmann T.A., Burnett D.S. 2009. Noble gas
4 composition of the solar wind as collected by the Genesis mission. *Geochimica et*
5 *Cosmochimica Acta* **73**: 7414-7432.
6
7
8 Hewins R. H., Bourot-Denis M., Zanda B., Leroux H., Barrat J-A., Humayun M., Göpel C.,
9 Greenwood R. C., Franchi I. A., Gattacceca J., Pont S., Lorand J.-P., Rochette P., Kuga
10 M., Marty B., Courne C., Marrocchi, Y. 2014. The Paris meteorite: the least altered CM
11 chondrite so far. *Geochimica et Cosmochimica Acta* **124**:190-222.
12
13
14 Humayun M., Simon S.B. and Grossman L. 2007. Tungsten and hafnium distribution in calcium-
15 aluminum inclusions (CAIs) from Allende and Efremovka, *Geochimica et Cosmochimica*.
16 *Acta* **71**:4609-4627.
17
18
19 Humayun M. 2012. Chondrule cooling rates inferred from diffusive profiles in metal lumps
20 the Acfer 097 CR2 chondrite. *Meteoritics and Planetary Science* **47**:1191-1208.
21
22
23 Ivanova M.A., Kononkova N.N., Krot A.N., Greenwood R.C., Franchi I.A., Verchovsky A.B.,
24 Trieloff M., Korochansteva E.V., Brandstaetter F. 2008. The Isheyevo meteorite:
25 Mineralogy, petrology, bulk chemistry, oxygen, nitrogen, carbon isotopic compositions
26 and ^{40}Ar - ^{39}Ar ages. *Meteoritics and Planetary Science* **43**:915-940.
27
28
29 Ivanova M. A. and Petaev M. I. 2015. Characteristics and origin of the components of the
30 carbonaceous chondrite NWA 470. *Petrology* **23**:150–167.
31
32
33 Ivanova M.A., Lorenz C.A., Humayun M., Richter K., Corrigan C.M., Franchi I.A., Verchovsky
34 A.B., Korochantseva E.V., Kozlov V.V., Teplyakova S.N., Kononkova N. N., and
35 Korochantsev A.V. 2019. Properties of a new grouplet of G metal-rich chondrites.
36 (Abstract #6143) *Meteoritics and Planetary Science* **54**.
37
38
39 Jansen C. A., Brenker F. E., Krot A. N., Zipfel J., Pack A., Labenne L., Bizzarro M., and Schiller
40 M. 2019. Mineralogy, petrology, and oxygen isotopic composition of Northwest Africa
41 (NWA) 12379, a new metal-rich chondrite with affinity to ordinary chondrites. . (abstract
42 #2741) *50th Lunar and Planetary Science Conference*.
43
44
45
46
47
48 Keil K. 1968. Mineralogical and chemical relationships among enstatite chondrites. *Journal*
49 *Geophysical Research* **73**:6945-6976.
50
51
52 Kimura M., El Goresy A., Palme H., and Zinner E. 1993. Ca-Al-rich inclusions in the
53 unique chondrite ALH 85085 – Petrology, chemistry, and isotopic compositions.
54 *Geochimica et Cosmochimica Acta* **57**:2329–2359.
55
56
57
58
59
60

- 1
2
3 Kita N. T., Nagahara H., Tachibana S., Tomomura S., Spicuzza M. J., Fournelle J. H. and Valley
4 J. W. 2010. High precision SIMS oxygen three isotope study of chondrules in LL3
5 chondrites: role of ambient gas during chondrule formation. *Geochimica et Cosmochimica*
6 *Acta* **74**: 6610–6635.
7
8
9
10 Koch T.E., Brenker F.E., Prior D. J., Jilly K., Krot A. N., Bizzarro M. 2019 Shock history of the
11 metal-rich CB chondrite Quebrada Chimborazo (QC) 001.82nd Annual Meeting of The
12 Meteoritical Society, held 7-12 July, 2019 in Sapporo, Japan. LPI Contribution No. 2157,
13 2019, id.6179.
14
15
16
17 Kong P. and Ebihara M. 1997. The origin and nebular history of the metal phase of ordinary
18 chondrites. *Geochimica et Cosmochimica Acta* **61**: 2317-2329.
19
20 Kong P., Mori T. and Ebihara M. 1997. Compositional continuity of enstatite chondrites and
21 implications for heterogeneous accretion of the enstatite chondrite parent body.
22 *Geochimica et Cosmochimica Acta* **61**: 4895-4914.
23
24
25
26 Kong P., Ebihara M. and Palme H. 1999. Distribution of siderophile elements in CR
27 chondrites: evidence for evaporation and recondensation during chondrule formation.
28 *Geochimica et Cosmochimica Acta* **63**:2637-4914.
29
30
31 Korochantseva E. V., Trieloff M., Buikin A. I., Hopp J. and Meyer H.-P. 2005. $^{40}\text{Ar}/^{39}\text{Ar}$ dating
32 and cosmic-ray exposure time of desert meteorites: Dhofar 300 and Dhofar 007 eucrites
33 and anomalous achondrite NWA 011. *Meteoritics & Planetary Science* **40**: 1433-1454.
34
35
36 Krot A. N., Meibom A., Weisberg M. K., and Keil K. 2002. The CR chondrite clan:
37 Implications for early solar system processes. *Meteoritics and Planetary Science*
38 **37**:1451–1490.
39
40
41 Krot A. N., Amelin Y., Cassen P., and Meibom A. 2005. Young chondrules in CB chondrites
42 from a giant impact in the early Solar System. *Nature* **436**: 989–992.
43
44
45 Krot, A.N., Nagashima, K., Bizzarro, M., Huss, G.R., Davis, A.M., McKeegan, K.D., Meyer, B.S.
46 and Ulyanov, A.A. 2008. Multiple generations of refractory inclusions in the metal rich
47 carbonaceous chondrites Acfer 182/214 and Isheyev. *Astrophysical Journal*. **672**:
48 713–721.
49
50
51 Krot, A.N., Amelin, Y., Bland, P., Ciesla, F.J., Connelly, J., Davis, A.M., Huss, G.R.,
52
53
54
55
56
57
58
59
60

- 1
2
3 Hutcheon, I.D., Makide, K., Nagashima, K., Nyquist, L.E., Russell, S.S., Scott, E.R.D.,
4 Thrane, K., Yurimoto, H. and Yin, Q.-Z. (2009) Origin and chronology of chondritic
5 components: A review. *Geochimica et Cosmochimica Acta* **73**: 4963–4998.
6
7
8 Krot, A.N., Nagashima, K., Yoshitake, M. and Yurimoto, H. 2010. Oxygen isotope
9 compositions of chondrules from the metal-rich chondrites Isheyevo (CH/CB_b), MAC
10 02675 (CB_b) and QUE 94627 (CB_b). *Geochimica et Cosmochimica Acta* **74**: 2190–2211.
11
12
13 Krot, A.N., Nagashima, K. and Petaev, M.I. 2012. Isotopically uniform, ¹⁶O-depleted
14 calcium, aluminum-rich inclusions in CH and CB carbonaceous chondrites. *Geochimica et*
15 *Cosmochimica Acta* **83**: 159–178.
16
17
18 Krot A. N., Keil K., Goodrich C., Weisberg M. K., and Scott E. R. D. 2014. Classification
19 of meteorites. In *Meteorites and Cosmochemical Processes* (Ed. A. M. Davis), Vol. 1
20 Treatise on Geochemistry, 2nd Ed. (Exec. Eds. H. D. Holland and K. K. Turekian),
21 Elsevier, Oxford, pp. 1–63. Elsevier.
22
23
24
25 Krot A. N., Nagashima K., E. M. M. van Kooten, and Bizzarro M. 2017. High-temperature rims
26 around calcium-aluminum-rich inclusions from the CR, CB and CH carbonaceous
27 chondrites. *Geochimica et Cosmochimica Acta* **201**: 155–184.
28
29
30
31 Leya I., and Masarik J. 2009. Cosmogenic nuclides in stony meteorites revisited. *Meteoritics &*
32 *Planetary Science* **44**: 1061-1086.
33
34
35 Meibom A., Petaev M. I., Krot A. N., Wood J. A., and Keil K. 1999. Primitive FeNi
36 metal grains in CH carbonaceous chondrites formed by condensation from a gas of solar
37 composition. *Journal of Geophysical Research* **104**:22053-22059.
38
39
40 Meibom A., Righter K., Chabot N., Dehn G., Antignano A., McCoy T. J., Krot A. N., Zolensky
41 M. E., Petaev M. I. and Keil K. (2005) Shock melts in QUE 94411, Hammadah al Hamra
42 237, and Bencubbin: Remains of the missing matrix? *Meteoritics and Planetary Sciences*
43 **40**:1377–1391.
44
45
46 Metzler K. 2012. Ultra rapid chondrite formation by hot accretion? Evidence from ordinary
47 chondrites. *Meteoritics and Planetary Sciences* **47**:2193-2217.
48
49
50 Miller M.F., Franchi I.A., Pillinger C.T. 1999. High precision measurements of the oxygen isotope
51 mass- depended fractionation line for the Earth-Moon System. (abstract # 1729). 30th Lunar
52 and Planet Science.
53
54
55 Munker C., Pfander J. A., Weyer S., Buchl A., Klein T. And Mezger K. 2003. Evolution of
56
57
58
59
60

- 1
2
3 planetary cores and the Earth-Moon system from Nb/Ta systematics. *Science* **301**:84-87.
4
5 Maruyama S., Yurimoto H., Sueno S. 1999. Oxygen isotope evidence regarding the formation of
6
7 spinel-bearing chondrules. *Earth and Planetary Science Letter* **169**:165-171.
8
9 Newsom H, E. and Drake M. J. 1979. The origin of metal clasts in the Bencubbin meteorite
10
11 breccia. *Geochimica et Cosmochimica Acta* **43**:689-707.
12
13 Oulton J., Humayun M., Fedkin A., and Grossman L. 2016. Chemical evidence for
14
15 differentiation, evaporation and recondensation from silicate clasts in Gujba. *Geochimica*
16
17 *et Cosmochimica Acta* **177**:254–274.
18
19 Ott U. 2002. Noble gases in meteorites – trapped components. In Noble gases, edited by Porcelli
20
21 D. P., Ballentine C. J., and Wieler R. P. Reviews in Mineralogy and geochemistry, vol. 47.
22
23 pp. 71–100.
24
25 Righter K. and Drake M. 1996. Core formation in Earth's Moon, Mars, and Vesta. *Icarus* **124**:
26
27 513-529.
28
29 Righter, K., Sutton, S.R., Danielson, L., Pando, K. and Newville, M., 2016. Redox variations in
30
31 the inner solar system with new constraints from vanadium XANES in spinels. *American*
32
33 *Mineralogist* **101**: 1928-1942.
34
35 Rubin A. E., Kallemeyn G. W., Wasson J. T., Clayton R. N., Mayeda T. K., Grady M.,
36
37 Verchovsky A. B., Eugster O., and Lorenzetti S. 2003. Formation of metal and silicate
38
39 globules in Gujba: a new Bencubbin-like meteorite fall. *Geochimica et Cosmochimica Acta*
40
41 **67**:3283–3298.
42
43 Rubin A. E. 2010. Physical properties of chondrules in different chondrites groups: implications
44
45 for multiple melting events in dusty environments. *Geochimica et Cosmochimica Acta*
46
47 **74**:4807-4828.
48
49 Russell S. S., McCoy T. J., Jerosewich E. And Ash R. D. 1998. The Burnwell, Kentucky, low
50
51 iron oxide chondrite fall. *Meteoritics and Planetary Science* **33**:853-856.
52
53 Schulze H. 2007. Mineralogy and mineral chemistry of noble metal grains in R chondrites.
54
55 (abstract # 1720). *30th Linar and Planetary Science Conference*.
56
57 Stoffler D., Keil K., and Scott E. R. D. 1991. Shock metamorphism of ordinary chondrites.
58
59 *Geochimica et Cosmochimica Acta* **55**:3845-3867.
60
61 Stewart S. T., Carter P. J., Davies E. J., Lock S. J., Kraus R. G., Root S., Petaev M. I., Jacobsen

- 1
2
3 S. B. 2019. Collapsing impact vapor plume model for chondrule and chondrite
4 formation. (abstract #1251). *50th Lunar and Planetary Science Conference*.
5
6 Sugiura N., Zashu S., Weisberg M. K., and Prinz M. 2000. A nitrogen isotope study of
7 bencubbinites. *Meteoritics & Planetary Science* **35**:987–996.
8
9 Troiano J., Rumble III, D., Rivers M. L. Abd Friedrich J. M. 2011. Composition of
10 three low- FeO ordinary chondrites: indicators of common origin with the H chondrites.
11 *Geochimica et Cosmochimica Acta* **75**:6511-6519.
12
13 van Kooten E. M. M. E., Wielandt D., Schiller M., Nagashima K., Thomen A., Larsen K.
14 K., Olsen M. B., Nordlund Å, Krot A. N., and Bizzarro M. 2016. Isotopic evidence for
15 primordial molecular cloud material in metal-rich carbonaceous chondrites. *Proceedings*
16 *of Natural Academy of Sciences* **113**:2011– 2016.
17
18 van Niekirk D., Keil K. and Humayun M. 2014. Petrogenesis of anomalous Queen Alexandra
19 Range enstatite meteorites and their relation to enstatite chondrites, primitive enstatite
20 achondrites, and aubrites. *Meteoritics and Planetary Science* **49**:295-312.
21
22 Verchovsky A. B., Fisenko A. V., Semjonova L. F., Wright I. P., Lee M. R., Pillinger C. T. 1998.
23 C, N, and noble gas isotopes in grain size separates of presolar diamonds from
24 Efremovka. *Science* **281**:1165.
25
26 Verchovsky A. B. 2017. Origin of isotopically light nitrogen in meteorites.. *Geochemistry*
27 *International* **55**: 957-970.
28
29 Wasson J. T. 1999. Trapped Melt in IIIAB Irons; Solid/Liquid Elemental Partitioning During the
30 Fractionation of the IIIAB Magma. *Geochimica et Cosmochimica Acta* **63**:2875-2889.
31
32 Wasson J. T. and Kallemeyn G. W. 1990. Allan Hills 85085: a subchondritic meteorite of mixed
33 nebular and regolithic heritage. *Earth and Planetary Science Letter* **101**:148-161.
34
35 Wasson J. T. and Richardson J. W. 2001. Fractionation Trends Among IVA iron Meteorites:
36 Contrasts with IIIAB Trends. *Geochimica et Cosmochimica Acta* **65**: 951-970.
37
38 Wasson J. T., Huber H., and Malvin D. J. 2007. Formation of IIAB Iron Meteorites. *Geochimica*
39 *et Cosmochimica Acta* **71**: 760-781.
40
41 Weber D., Zinner E., and Bischoff A. 1995. Trace element abundances and magnesium,
42 calcium, and titanium isotopic compositions of grossite-containing inclusions from the
43 carbonaceous chondrite Acfer 182. *Geochimica et Cosmochimica Acta* **59**:803–823.
44
45 Weisberg M. K., Prinz M. and Nehru C. E. 1990. The Bencubbin chondrite breccia and
46
47
48
49
50
51
52
53
54
55
56
57
58
59
60

- 1
2
3 its relationship to CR chondrites and the ALH85085 chondrite. *Meteoritics* **25**:269-279.
4
5 Weisberg M. K., Bosenberg J. S., Kozhusko G., Prinz M., Clayton R. N., and Mayeda T. K.
6
7 1995a. EH3 and EL3 chondrites: A petrologic-oxygen isotopic study (abstract). 26th
8
9 Lunar and Planetary Science Conference. p. 1481.
- 10 Weisberg, M.K., Prinz, M., Clayton, R.N., Mayeda, T.K., Grady, M.M. and Pillinger, C.T.
11
12 1995b. The CR chondrite clan. *Proceedings of NIPR Symposium on Antarctic Meteorites*
13
14 **8**: 11–32.
- 15 Weisberg M. K., Prinz M., Clayton R. N., Mayeda T. K., Sugiura N., Zashu S., and Ebihara
16
17 2001. A new metal-rich chondrite grouplet. *Meteoritics and Planetary Science* **36**: 401–
18
19 418.
- 20 Weisberg M. K., Bunch T. E., Wittke J. H., Rumble III, D. and Ebel D. S. 2012. Petrology and
21
22 oxygen isotopes of NWA 5492, a new metal-rich chondrite. *Meteoritics and Planetary*
23
24 *Science* **47**, 363-373.
- 25 Weisberg M. K., Ebel D. S., Nakashima D., Kita N. T., and Humayun M. 2015 Petrology
26
27 and geochemistry of chondrules and metal in NWA 5492 and GRO 95551: A new type of
28
29 metal-rich chondrite. *Geochimica et Cosmochimica Acta* **167**:269–285.
- 30
31 Weyrauch M., Horstmann, M. and Bischoff, A. 2018. Chemical variations of sulfides and metal
32
33 in enstatite chondrites—Introduction of a new classification scheme. *Meteoritics and*
34
35 *Planetary Science* **53**:394–415.
- 36
37 Wieler R. 2002. Cosmic-ray-produced noble gases in meteorites. In Noble gases, edited by
38
39 Porcelli D. P., Ballentine C. J., and Wieler R. P. *Reviews in Mineralogy and geochemistry*,
40
41 vol. 47. pp. 125–170.
- 42
43 Wright I. P., Grady M. M., Pillinger C. T. 1988. Carbon, oxygen and nitrogen isotopic
44
45 compositions of possible Martian weathering products in EETA 79001.
46
47
48
49
50
51
52
53
54
55
56
57
58
59
60

1
2
3
4
5
6
7
8
9
10
11
12
13
14
15
16
17
18
19
20
21
22
23
24
25
26
27
28
29
30
31
32
33
34
35
36
37
38
39
40
41
42
43
44
45
46
47
48
49
50
51
52
53
54
55
56
57
58
59
60

For Peer Review Only

Table 1. Modal abundances (vol%) of SG 009 compared to average metal-rich chondrites: NWA 5492, CH, CB and NWA 12379 and ECs.

	SG 009	NWA 5492	EH3	EL3	CH	CB	NWA 12379
Olivine	5.2	6.3	4.4	2.4	-	-	-
Pyroxene	40.1	44.7	60.4	65.2	-	-	-
Ca-pyroxene	4.0	4.1	0.1	0.3	-	-	-
Glass	10.2	14.9	8.3	10.4	-	-	-
Silica	1.1	3.1	1.6	1.4	-	-	-
Fe-sulfide	9.2	2.5	10.4	7.6	<1	<1	5.0
Daubreelite	1.7	trace	0.6	0.3	<1	<1	nf
Alabandite	<1	nf	nd	0.4	nf	nf	nf
Schreibersite	2.8	1.8	0.6	0.6	nf	nf	nf
Chromite	<1	nf	nf	nf	-	-	<1
Phosphate	nf	nf	nf	nf	nf	nf	<1
PGE particles	<1	nf	nf	nf	nf	nf	nf
Graphite	<1	nf	<1	<1	nf	nf	nf
FeNi	23.1	22.6	9.3	10.3	22.0	60-80	70.0

Notes: nf= not found, nd= not determined; NWA, Northwest Africa.

Data for NWA 5492, CH, and CB from (Weisberg et al. 2001, 2015); data for NWA 12379 from (Jansen et al. 2019)

Data for EH and EL from (Weisberg et al. 1995a).

Table 2. Average composition of olivine (in wt.%) in SG 009, and other metal-rich chondrites, NWA 5492, GRO 95551, CH, CB and NWA 12379 chondrites.

	SG 009	NWA 5492	GRO 95551	Bencubbin	HaH 237	NWA 12379
SiO ₂	42.7±0.17	41.9	42.2	42.0	41.2	38.8
Cr ₂ O ₃	0.04±0.02	0.0	<0.1	0.6	0.5	0.1
FeO	0.51±0.11	0.1	1.5	3.5	4.1	23.6
MnO	0.15±0.02	0.0	0.2	0.2	<0.1	0.4
MgO	57.8±0.19	0.2	55.4	54.1	53.0	38.8
CaO	0.04±0.02	0.0	<0.1	0.2	0.2	0.1
Total		99.6	99.3	100.6	99.0	101.8
Fa (mol%)	0.49±0.11	0.3	1.3	3.4	4.1	25.4
SD		0.2	0.8	0.4	1.4	2.4
# grains	64	43	21	31	27	37

Table 3. Average and representative analyses of pyroxene, plagioclase, glass, chromite and spinel compositions (in wt.%) in SG 009.

	SiO ₂	TiO ₂	Al ₂ O ₃	Cr ₂ O ₃	FeO	MnO	MgO	CaO	Na ₂ O	K ₂ O	Total	Fs (mol%)	Wo (mol%)	An (mol%)	Ab (mol%)
low-Ca-Px (39)	58.9±0.7	0.1±0.1	0.7±0.6	0.3±0.1	0.7±0.2	0.3±0.1	39.1±0.7	0.5±0.01	0.01±0.0	0.02±0.0	100.5	1.4±0.4	0.9±0.6		
FeO-rich low-Ca Px	56.9	b.d.	0.06	0.24	6.21	0.21	34.78	0.36	b.d.	b.d.	98.8	9.3	0.7		
FeO-rich low-Ca Px	52.0	0.10	1.62	0.51	20.18	0.41	23.08	1.31	b.d.	b.d.	99.2	32.5	2.6		
Ca-Px	55.4	0.00	2.11	0.00	1.07	b.d.	21.80	19.7	b.d.	b.d.	100.0	1.3	46.3		
Al-rich Ca-Px	51.3	0.65	12.5	0.63	1.23	0.06	31.48	3.21	b.d.	0.02	101.1	2.1	6.7		
Al-rich low-Ca- Px	49.7	0.41	15.4	0.50	1.22	0.08	31.76	1.56	b.d.	0.02	100.7	2.2	3.3		
Plagioclase	59.5	0.05	19.6	0.05	0.90	0.04	9.70	4.30	4.86	0.19	99.2			32.3	66.0
Plagioclase	51.5	0.05	31.3	0.02	1.03	0.02	0.23	12.6	3.64	0.10	100.6			65.4	34.0
Plagioclase	57.0	0.00	28.6	0.01	0.20	b.d.	0.19	9.32	6.38	0.13	101.8			44.4	54.9
Plagioclase	43.2	0.06	37.1	0.00	0.09	b.d.	0.02	18.1	0.80	0.04	99.5			92.4	7.4
Glass	65.3	0.02	22.9	0.02	0.54	0.02	0.49	2.66	8.47	0.37	100.8				
Glass	65.6	0.08	19.7	0.00	0.64	b.d.	0.11	0.82	4.29	9.18	100.5				
Glass	51.8	3.06	11.5	0.24	0.33	0.03	11.89	16.9	2.39	0.24	98.4				
Mg-chromite	b.d.	0.28	0.00	77.3	2.15	2.46	18.7	b.d.	b.d.	0.02	100.9				
Spinel	b.d.	0.04	67.93	3.53	0.29	0.09	28.34	0.04	b.d.	b.d.	100.3				

Table 4. Representative analyses of troilite, daubreelite, schreibersite and Fe,Ni-metal in SG 009 (wt.%).

	Fe	Cr	Ni	Mn	S	P	Si	Co	Total
Troilite	59.5	2.40	0.02	0.10	36.7	b.d.	b.d.	0.08	98.8
Troilite	61.1	1.28	0.04	0.03	36.7	b.d.	b.d.	0.05	99.1
Schreibersite	51.5	0.02	32.57	0.00	0.03	15.46	b.d.	0.11	99.6
Daubreelite	18.9	34.6	0.04	1.25	44.4	b.d.	b.d.	0.03	99.3
Fe,Ni-metal	93.8	b.d.	5.97	0.01	b.d.	0.08	b.d.	0.44	100.3
Fe,Ni-metal	62.2	b.d.	36.27	0.00	b.d.	0.05	b.d.	0.21	98.7
Fe,Ni-metal	69.1	b.d.	29.69	0.00	b.d.	0.06	b.d.	0.26	99.2

b.d. – below detection.

Table 5. Representative and average compositions of PGE-enriched Fe,Ni-metal particles in SG 009 (wt.%) obtained by EPMA (2, 3, 5) and EDS (other points) analyses.

area	N	Fe	Co	Ni	Ru	Rh	Pd	Os	Ir	Pt	Total
3	2	60.7	0.38	30.3	2.1	0.53	b.d.	1.6	0.93	1.79	98.36
	3	61.3	0.31	29.6	2.01	0.44	b.d.	1.65	0.83	2.12	98.29
	5	61.7	0.25	29.8	2.11	0.48	b.d.	1.44	1.16	2.08	99.03
31	181	53.0	0.32	6.52	1.55	0.28	b.d.	3.44	7.33	27.6	100
	182	52.6	0.41	22.3	2.07	b.d.	b.d.	0.91	4.19	17.5	100
	185	56.3	0.32	15.8	1.57	0.20	b.d.	2.28	5.35	18.1	100
4520	1	57.9	n.d.	18.1	3.17	0.30	0.27	4.78	5.91	9.63	100
	2	69.7	n.d.	20.7	2.11	0.20	0.17	1.69	2.07	3.32	100
46	average (4)	67.7	0.46	17.4	7.94	1.52	0.28	0.10	0.39	4.22	100
	average (2)	62.3	0.40	16.9	10.6	1.91	0.27	0.38	0.57	6.69	100
1554	average										
	(10)	61.1	0.36	30.1	2.30	0.52	b.d.	1.61	1.44	2.59	100

n.d. - not determined; b.d. - below detection limit

Table 6. Siderophile element abundances in metal of SG 009 by LA-ICP-MS.

		101-G	102-G	103-G	104-G	105-G	106-G	107-G	108-G	109-G	110-G	111-G	112-G	113-G
Si	(wt.%)	0.05	0.04	0.05	0.06	0.06	0.04	<i>0.02</i>	0.04	0.06	0.06	0.04	0.04	0.05
P	(wt.%)	0.037	0.030	0.042	0.042	0.029	0.037	0.031	0.054	0.035	0.019	0.028	0.034	0.017
V	(ppm)	b.d.	b.d.	b.d.	b.d.	b.d.	b.d.	b.d.	b.d.	b.d.	b.d.	b.d.	b.d.	b.d.
Cr	(ppm)	3	<i>1</i>	b.d.	b.d.	b.d.	b.d.	b.d.	b.d.	b.d.	b.d.	b.d.	<i>0.4</i>	b.d.
Mn	(ppm)	1	1	2	1	1	1	5	1	1	3	2	2	2
Fe	(wt.%)	93.9	94.2	93.9	94.1	94.3	93.9	93.8	94.1	93.9	94.1	94.0	94.1	94.3
Co	(wt.%)	0.336	0.336	0.337	0.327	0.342	0.334	0.336	0.341	0.335	0.341	0.339	0.334	0.337
Ni	(wt.%)	5.67	5.38	5.62	5.44	5.21	5.63	5.53	5.40	5.62	5.46	5.60	5.51	5.28
Cu	(ppm)	38	35	38	36	36	37	37	35	38	36	39	35	35
Ga	(ppm)	16.8	15.5	16.4	15.9	15.6	15.9	16.1	15.9	16.0	15.6	16.9	16.0	15.4
Ge	(ppm)	28.8	26.5	26.2	25.8	26.3	25.8	26.0	26.0	26.5	25.9	24.8	25.0	26.4
As	(ppm)	4.26	3.92	4.12	4.05	4.39	4.05	3.81	3.76	4.00	4.07	3.72	4.35	4.43
Mo	(ppm)	6.22	4.21	4.23	<i>3.16</i>	4.39	4.46	<i>3.49</i>	5.01	<i>2.59</i>	5.07	4.05	4.52	<i>3.07</i>
Ru	(ppm)	2.57	2.48	2.74	3.45	4.28	3.10	2.72	7.28	2.37	2.95	2.37	2.48	2.88
Rh	(ppm)	0.40	0.39	0.46	0.54	0.69	0.40	0.46	1.27	0.40	0.36	0.40	0.42	0.51
Pd	(ppm)	2.54	2.83	2.71	2.55	3.56	2.17	2.40	3.95	2.56	2.67	2.33	2.17	2.32
Sn	(ppm)	0.41	0.36	0.34	0.39	0.44	0.37	0.36	0.37	0.39	0.45	0.33	0.30	0.32
Sb	(ppm)	<i>0.16</i>	<i>0.16</i>	<i>0.19</i>	<i>0.11</i>	<i>0.08</i>	<i>0.13</i>	<i>0.17</i>	<i>0.09</i>	<i>0.16</i>	<i>0.08</i>	<i>0.11</i>	<i>0.08</i>	<i>0.14</i>
W	(ppm)	0.89	1.35	1.09	1.17	0.85	0.90	0.78	0.70	0.85	0.60	0.65	0.93	0.97
Re	(ppm)	0.09	0.12	0.20	0.20	0.28	0.12	0.14	0.57	0.06	0.12	0.08	0.19	0.20
Os	(ppm)	0.92	0.86	2.33	1.75	3.14	1.95	1.08	5.22	0.87	1.08	1.15	1.74	2.29
Ir	(ppm)	0.86	1.00	1.91	1.50	2.54	1.46	0.96	4.67	1.00	1.23	1.07	1.75	1.89
Pt	(ppm)	2.27	2.32	4.29	3.75	5.78	3.28	2.88	10.66	2.65	2.50	3.00	3.00	3.78
Au	(ppm)	0.60	0.69	0.55	0.67	0.64	0.58	0.55	0.62	0.52	0.62	0.73	0.67	0.66

D.L. – detection limit. Values in italics are at the detection limit; b.d. – below detection.

Table 6 (continued).

	114-G	115-G	116-G	117-G	118-G	119-G	120-G	121-G	122-G	123-G	124-G	125-G	127-G	128-G	Metal average	D.L.
	0.03	0.04	0.05	0.04	0.04	0.02	0.08	0.03	0.01	0.02	0.01	b.d.	b.d.	b.d.	0.04	0.03
	0.025	0.022	0.017	0.023	0.031	0.038	0.030	0.043	0.033	0.028	0.037	0.032	0.028	0.030	0.032	0.003
	b.d.	b.d.	b.d.	b.d.	b.d.	b.d.	b.d.	b.d.	b.d.	b.d.	b.d.	b.d.	1	b.d.	1	0.4
	b.d.	b.d.	b.d.	0.8	b.d.	b.d.	b.d.	b.d.	b.d.	b.d.	b.d.	0.13	23	4	5	1
	3	2	2	2	2	2	4	6	2	3	3	3	2	1	2	1
	94.2	94.1	94.1	94.0	94.3	93.9	93.8	93.9	94.2	94.3	94.0	94.1	94.0	94.3	94.1	
	0.336	0.342	0.337	0.339	0.333	0.339	0.337	0.337	0.337	0.338	0.328	0.337	0.333	0.320	0.336	
	5.39	5.52	5.46	5.61	5.26	5.70	5.69	5.65	5.39	5.33	5.60	5.47	5.62	5.37	5.50	
	37	36	35	36	34	38	36	39	37	36	39	39	39	38	37	2
	17.1	16.2	16.0	16.2	15.4	16.6	16.0	16.5	16.6	16.3	16.2	16.6	16.5	15.5	16.1	0.2
	25.5	25.3	25.2	23.9	25.6	25.6	24.2	25.1	28.0	25.2	24.5	25.1	25.7	25.0	25.7	0.2
	3.92	3.94	4.05	3.75	3.98	4.13	4.00	4.19	3.50	4.02	3.66	3.55	3.89	4.00	3.98	1.20
	4.43	4.35	4.36	3.63	5.72	5.16	3.45	7.18	5.97	5.71	5.54	3.21	3.13	3.04	4.42	4
	2.42	2.11	2.54	2.43	2.22	2.67	1.70	3.39	4.13	6.14	2.20	2.21	1.94	2.92	2.99	0.04
	0.30	0.40	0.41	0.38	0.44	0.42	0.24	0.73	0.68	0.99	0.33	0.27	0.36	0.53	0.49	0.01
	2.28	2.11	2.22	1.95	2.43	2.59	2.08	2.68	2.16	2.30	2.23	2.86	2.64	2.57	2.51	0.05
	0.63	0.39	0.47	0.39	0.36	0.42	0.32	0.43	0.42	0.32	0.37	0.41	0.36	0.31	0.39	0.05
	0.20	0.07	0.12	0.12	0.15	0.11	0.12	0.12	0.12	0.12	0.06	0.08	0.08	0.14	0.12	0.2
	0.41	0.56	0.76	0.66	1.09	0.48	0.37	0.60	0.86	0.51	0.74	0.29	0.56	0.85	0.76	0.01
	0.03	0.09	0.11	0.06	0.08	0.14	0.06	0.23	0.31	0.56	0.14	0.09	0.06	0.19	0.17	0.01
	0.86	1.26	0.77	0.82	1.59	1.53	0.44	2.12	2.51	4.52	0.75	0.96	0.95	1.72	1.67	0.001
	0.93	1.42	0.82	0.99	1.17	1.24	0.53	1.86	1.97	4.47	0.70	0.82	0.64	1.65	1.52	0.003
	2.89	2.81	2.46	1.62	3.00	2.84	1.76	4.59	5.19	9.66	1.83	2.14	2.34	3.51	3.59	0.01
	0.51	0.53	0.63	0.60	0.58	0.56	0.62	0.60	0.62	0.61	0.59	0.60	0.63	0.60	0.61	0.03

Table 7. Representative elemental compositions of SG 009 chondrule fragments (85-G – 109-G, rasters; 129-G – 136-G, spots) and sulfides (110-G – 114-G, spots) where major elements in weight%, trace elements in ppm; b.d.=below detection, n.d.= not determine.

Object name	85-G	89-G	96-G	97-G	98-G	99-G	100-G	101-G	102-G	103-G
SiO ₂	53.26	60.60	59.61	54.55	56.21	52.06	55.49	50.68	54.76	56.24
TiO ₂	0.134	0.051	0.073	0.087	0.026	0.084	0.026	0.069	0.195	0.093
Al ₂ O ₃	3.71	0.98	1.34	1.20	1.81	1.36	0.19	0.51	1.39	1.09
FeO _T	5.00	3.54	3.37	5.70	5.63	9.08	7.22	10.59	4.85	3.54
MnO	0.188	0.192	0.176	0.203	0.169	0.167	0.112	0.180	0.230	0.197
MgO	32.97	32.60	33.17	35.05	34.33	32.91	35.88	34.62	32.92	35.93
CaO	3.00	1.47	1.30	2.62	0.71	3.49	0.92	1.23	5.04	2.31
Na ₂ O	0.60	0.23	0.55	0.30	0.84	0.37	0.07	0.11	0.43	0.41
K ₂ O	0.02	0.03	0.24	0.03	0.08	0.03	0.01	0.01	0.04	0.05
P ₂ O ₅	0.022	0.001	0.003	0.007	0.011	0.028	0.036	0.069	0.004	0.013
S	1.09	0.30	0.17	0.25	0.18	0.42	0.05	1.92	0.15	0.13
Li	7	12	7	11	4	20	8	12	13	7
Be	0.055	0.043	0.060	0.039	0.071	0.047	b.d.	b.d.	0.009	0.015
B	3.61	3.10	2.45	23.43	4.24	30.34	3.27	15.58	11.47	6.41
Sc	10	5	6	8	5	9	3	6	19	12
V	53	43	35	30	10	25	34	60	63	17
Cr	2888	2850	1190	1389	825	1136	2108	2854	2145	889
Co	96	46	60	104	180	146	135	283	75	58
Ni	1969	986	752	1399	2569	2244	2192	3455	1139	868
Cu	35	6	5	6	12	5	1	72	2	9
Zn	23	17	19	20	24	17	13	20	21	28
Ga	0.76	0.22	0.04	0.10	0.06	0.29	0.07	0.27	0.14	0.23
Ge	0.34	0.04	0.02	0.03	0.05	0.12	0.08	0.30	0.03	0.16
As	0.07	0.00	0.04	0.05	0.02	0.03	0.01	0.05	0.01	0.05
Se	1.63	0.35	0.26	0.44	0.32	0.40	0.05	2.69	0.20	0.29
Rb	0.4	0.9	6.2	0.6	1.0	0.5	0.4	0.2	0.6	1.0
Sr	158.7	24.0	39.6	185.2	34.6	149.5	13.7	114.8	143.1	70.3
Y	1.8	1.2	1.3	1.9	0.6	2.3	0.4	1.1	4.1	2.4
Zr	5.0	2.7	3.9	4.3	2.1	5.9	0.9	2.4	6.6	5.3
Nb	0.16	0.19	0.13	0.06	0.02	0.10	0.02	0.07	0.08	0.03
Mo	0.21	0.04	0.10	0.25	0.11	0.28	0.08	0.32	0.11	0.28
Ag	0.03	0.02	0.02	0.08	0.03	0.03	0.02	0.03	0.01	0.03
Cd	0.04	0.01	0.02	0.05	0.04	0.04	0.02	0.02	0.03	0.02
In	0.006	0.001	0.002	0.005	0.002	0.004	0.016	0.001	0.002	0.005
Sn	0.04	0.03	0.03	0.07	0.07	0.07	0.10	0.12	0.08	0.07
Sb	0.02	0.01	0.01	0.01	0.01	0.16	0.01	0.01	0.01	0.01
Cs	0.04	0.07	0.09	0.04	0.05	0.05	0.05	0.04	0.15	0.06
Ba	4.91	1.74	9.74	4.48	7.23	3.56	0.55	1.65	4.14	3.69
La	0.46	0.18	0.16	0.26	0.13	0.42	0.06	0.19	0.29	0.23
Ce	1.27	0.58	0.55	0.91	0.41	1.38	0.28	0.62	1.21	0.87
Pr	0.15	0.08	0.07	0.12	0.05	0.19	0.03	0.08	0.22	0.13
Nd	0.66	0.37	0.36	0.60	0.20	0.87	0.13	0.36	1.26	0.71
Sm	0.18	0.12	0.13	0.19	0.06	0.26	0.04	0.11	0.48	0.26
Eu	0.13	0.04	0.06	0.05	0.08	0.06	0.00	0.01	0.06	0.04
Gd	0.248	0.170	0.173	0.257	0.074	0.341	0.052	0.139	0.668	0.350
Tb	0.042	0.029	0.031	0.045	0.013	0.057	0.012	0.025	0.116	0.061
Dy	0.302	0.201	0.222	0.314	0.091	0.395	0.064	0.185	0.792	0.422

1	Ho	0.066	0.044	0.050	0.070	0.022	0.085	0.016	0.042	0.165	0.089
2	Er	0.208	0.135	0.157	0.221	0.066	0.261	0.054	0.139	0.468	0.266
3	Tm	0.030	0.019	0.023	0.032	0.010	0.037	0.009	0.021	0.062	0.037
4	Yb	0.233	0.148	0.184	0.224	0.098	0.259	0.073	0.164	0.418	0.246
5	Lu	0.036	0.023	0.025	0.043	0.012	0.040	0.012	0.028	0.059	0.041
6	Hf	0.162	0.077	0.111	0.127	0.095	0.169	0.022	0.071	0.273	0.165
7	Ta	0.017	0.010	0.013	0.012	0.004	0.016	0.003	0.007	0.013	0.016
8	W	0.010	0.003	0.004	0.009	0.005	0.007	0.013	0.012	0.003	0.020
9	Tl	0.001	0.000	0.001	0.002	0.001	0.001	0.001	0.002	0.000	0.001
10	Pb	0.067	0.105	0.058	0.069	0.100	0.138	0.507	0.201	0.215	0.105
11	Bi	0.009	0.004	0.005	0.003	0.008	0.005	0.034	0.003	0.005	0.021
12	Th	0.045	0.023	0.032	0.039	0.025	0.053	0.008	0.024	0.028	0.032
13	U	0.017	0.010	0.014	0.026	0.006	0.017	0.014	0.008	0.023	0.010

Table 7 (continued).

	104-G	105-G	106-G	107-G	108-G	109-G	129-G	130-G	131-G	132-G	133-G
21	56.03	57.81	54.24	57.94	58.43	55.52	48.87	48.08	47.10	45.02	57.40
22	0.042	0.013	0.125	0.114	0.122	0.133	0.231	0.208	0.257	0.146	0.119
23	0.38	0.18	2.21	1.71	1.98	1.44	3.05	4.33	5.15	3.83	2.49
24	3.09	7.83	7.40	1.71	1.69	4.27	3.58	1.59	4.01	1.60	2.02
25	0.165	0.189	0.629	0.197	0.213	0.212	0.194	0.169	0.152	0.163	0.244
26	37.64	31.15	29.56	33.87	34.18	33.35	40.20	41.74	38.17	45.85	34.42
27	2.42	2.48	4.44	2.68	2.10	3.48	3.56	3.14	4.46	2.71	2.34
28	0.13	0.14	0.94	0.68	0.88	0.47	0.29	0.70	0.66	0.66	0.89
29	0.01	0.03	0.09	0.40	0.14	0.27	0.01	0.03	0.03	0.03	0.06
30	0.005	0.005	0.006	0.002	0.002	0.008	0.008	0.009	0.010	0.009	0.000
31	0.08	0.16	0.35	0.70	0.26	0.84	n.d.	n.d.	n.d.	n.d.	n.d.
32	8	23	12	6	5	7	9	4	7	6	5
33	0.016	0.007	0.008	0.012	0.017	0.029	0.059	0.045	0.070	0.044	0.042
34	16.86	0.98	50.57	23.15	33.36	212.67	152	19	123	32	35
35	6	2	10	10	10	13	22	19	21	14	12
36	10	56	89	19	63	30	97	84	85	66	66
37	631	4078	5809	1348	2831	1557	2742	2294	2676	1775	3632
38	28	65	48	14	29	139	84	24	85	21	22
39	389	1064	1267	205	429	1949	1245	221	1407	371	342
40	1	4	5	9	7	14	5	9	11	5	20
41	17	10	9	57	17	88	25	25	21	24	20
42	0.07	0.34	0.33	0.04	0.13	0.16	0.17	0.08	0.12	0.07	0.13
43	0.02	0.08	0.03	0.03	0.03	0.07	0.02	0.01	0.02	-0.01	0.06
44	0.00	0.04	0.01	0.00	3.73	71.70	0.40	0.10	0.53	0.21	2.52
45	0.16	0.21	0.40	1.09	0.31	0.89	n.d.	n.d.	n.d.	n.d.	n.d.
46	0.3	0.9	1.5	8.8	2.9	7.0	0.4	0.9	0.6	0.8	2.1
47	127.2	49.2	70.5	79.3	69.8	138.1	118.1	29.9	76.4	38.3	88.9
48	1.0	0.5	2.4	1.7	2.1	3.1	5.1	4.6	6.5	3.5	3.1
49	2.7	1.1	5.7	6.0	5.2	7.9	8.1	12.1	14.9	11.4	7.6
50	0.02	0.04	0.48	0.06	0.46	0.10	0.36	0.76	0.90	0.74	0.42
51	0.16	0.06	0.50	0.15	1.72	6.18	1.19	0.10	1.46	0.25	2.14
52	0.01	0.04	0.05	0.03	0.07	0.08	0.03	0.03	0.03	0.02	0.06
53	0.02	0.02	0.02	0.02	0.08	0.26	0.03	0.01	0.01	0.01	0.05
54	0.005	0.009	0.001	0.002	0.001	0.010	0.001	b.d.	b.d.	b.d.	b.d.

	0.04	0.05	0.03	0.02	0.02	0.07	0.02	0.02	0.02	0.02	0.02
1	0.01	0.01	0.01	0.01	0.03	0.35	0.02	0.01	0.03	0.01	0.03
2	0.03	0.06	0.07	0.11	0.13	0.08	0.03	0.02	0.04	0.02	0.22
3	2.44	1.37	7.59	16.78	11.14	43.87	5.64	3.80	9.68	5.27	8.99
4	0.17	0.09	0.38	0.16	0.33	0.38	0.469	0.732	0.824	0.682	0.448
5	0.55	0.46	1.19	0.61	1.10	1.27	1.434	1.970	2.279	1.777	1.354
6	0.08	0.06	0.17	0.09	0.15	0.19	0.235	0.279	0.360	0.243	0.181
7	0.36	0.28	0.82	0.49	0.70	1.00	1.260	1.409	1.807	1.164	0.902
8	0.10	0.08	0.23	0.18	0.19	0.32	0.453	0.400	0.582	0.337	0.231
9	0.01	0.01	0.08	0.07	0.08	0.07	0.053	0.129	0.122	0.136	0.115
10	0.145	0.084	0.353	0.247	0.318	0.491	0.660	0.629	0.942	0.524	0.444
11	0.024	0.015	0.063	0.043	0.055	0.084	0.114	0.109	0.168	0.094	0.080
12	0.169	0.093	0.430	0.300	0.371	0.559	0.802	0.772	1.140	0.642	0.540
13	0.038	0.019	0.091	0.065	0.079	0.120	0.181	0.163	0.246	0.132	0.113
14	0.115	0.056	0.280	0.191	0.250	0.351	0.565	0.520	0.763	0.443	0.376
15	0.017	0.008	0.040	0.027	0.035	0.046	0.080	0.070	0.099	0.060	0.051
16	0.126	0.072	0.247	0.171	0.181	0.263	0.552	0.469	0.677	0.400	0.293
17	0.021	0.008	0.044	0.029	0.038	0.048	0.090	0.078	0.108	0.066	0.055
18	0.080	0.027	0.163	0.177	0.147	0.231	0.258	0.336	0.432	0.326	0.236
19	0.010	0.004	0.021	0.019	0.020	0.025	0.024	0.037	0.045	0.042	0.024
20	0.003	0.016	0.001	0.002	0.014	0.179	0.056	0.120	0.186	0.155	0.013
21	0.000	0.001	0.001	0.001	0.005	0.056	0.001	0.001	0.002	0.002	0.004
22	0.049	0.625	0.385	0.068	0.086	0.234	0.184	0.323	0.355	0.362	0.108
23	0.002	0.013	0.007	0.002	0.012	0.007	0.003	0.003	0.007	0.005	0.001
24	0.021	0.007	0.047	0.043	0.043	0.055	0.051	0.089	0.112	0.103	0.066
25	0.008	0.017	0.025	0.015	0.120	1.040	0.120	0.016	0.103	0.029	0.078

Table 7 (continued).

	134-G	135-G	136-G		110-G	111-G	112-G	113-G	114-G	Detection Limit
35	56.12	57.84	55.54	Si	0.15	0.51	0.21	0.61	1.09	0.005
36	0.050	0.105	0.063	Ti	0.003	0.004	0.003	0.003	0.003	0.0001
37	0.53	2.10	0.64	Al	0.01	0.08	0.01	0.01	0.02	0.001
38	2.98	1.42	3.91	Fe	51.72	44.43	44.89	44.57	42.08	0.0001
39	0.183	0.203	0.392	Mn	0.410	0.397	0.351	0.236	0.400	0.00001
40	38.80	33.00	36.64	Mg	0.17	0.35	0.28	0.18	0.92	0.0005
41	1.20	3.81	2.56	Ca	0.76	0.29	0.20	0.05	0.48	0.002
42	0.11	1.01	0.22	Na	0.57	0.13	0.15	0.20	0.24	0.002
43	0.03	0.51	0.03	K	0.14	0.03	0.04	0.05	0.06	0.002
44	0.003	0.001	0.004	P	0.096	0.028	0.001	0.028	0.001	0.0001
45	n.d.	n.d.	n.d.	S	30.10	39.81	40.33	40.26	40.39	0.001
46										
47	6	7	8	Li	141	13	18	17	28	0.07
48	0.032	0.025	0.032	Be	b.d.	b.d.	b.d.	b.d.	b.d.	0.02
49	58	30	67	B	28.18	1.61	1.09	0.95	20.05	0.03
50	6	12	9	Sc	2.4	2.0	1.2	0.7	0.4	0.2
51	46	19	75	V	855	765	639	499	1059	0.001
52	1871	1351	3067	Cr	68648	35680	34685	30028	60851	0.04
53	40	10	28	Co	272	26	51	118	83	0.01
54	688	252	412	Ni	10406	1093	1123	6788	2652	0.06
55	4	12	5	Cu	510	732	375	366	1582	0.2
56	15	99	22	Zn	65	59	63	11	84	0.02

	0.11	0.05	0.43	Ga	2.78	0.70	0.28	0.14	1.08	0.01
1	0.02	0.00	0.00	Ge	1.27	1.30	1.15	1.05	1.09	0.02
2	1.89	0.01	0.04	As	0.26	0.10	0.09	0.24	0.08	0.003
3	n.d.	n.d.	n.d.	Se	71.05	58.51	59.22	55.52	58.48	0.1
4	1.7	11.5	0.5	Rb	1.1	0.5	0.5	1.0	0.7	0.02
5	26.7	108.8	92.0	Sr	113.5	30.0	27.9	3.3	104.4	0.004
6	0.7	2.2	1.3	Y	0.0	0.1	0.0	0.0	0.0	0.003
7	1.7	7.6	2.1	Zr	0.1	0.2	0.1	0.1	0.1	0.004
8	0.03	0.05	0.04	Nb	0.60	0.54	0.54	0.66	0.58	0.0005
9	0.96	0.14	0.30	Mo	4.57	1.32	1.50	3.93	5.56	0.01
10	0.03	0.04	0.03	Ag	0.24	0.30	0.21	0.60	0.44	0.001
11	0.10	0.01	b.d.	Cd	0.07	0.09	0.06	0.17	0.04	0.002
12	b.d.	b.d.	b.d.	In	b.d.	b.d.	b.d.	0.4981	b.d.	0.0009
13	0.03	0.02	0.02	Sn	0.02	0.02	0.01	1.38	0.01	0.004
14	0.03	0.00	0.01	Sb	0.02	0.01	0.02	1.13	0.01	0.001
15	0.07	0.17	0.03	Cs	0.11	0.10	0.10	0.25	0.12	0.02
16	2.70	20.39	3.13	Ba	0.36	0.47	0.21	0.87	0.60	0.001
17	0.095	0.203	0.141	La	0.003	0.012	0.003	0.037	0.009	0.002
18	0.287	0.673	0.479	Ce	0.003	0.028	0.009	0.228	0.032	0.0003
19	0.038	0.104	0.068	Pr	0.001	0.006	0.002	0.072	0.004	0.0003
20	0.192	0.571	0.350	Nd	0.003	0.044	0.017	0.082	0.022	0.001
21	0.061	0.244	0.121	Sm	0.002	0.015	0.003	0.109	0.005	0.001
22	0.013	0.096	0.017	Eu	0.004	0.009	0.001	0.008	0.002	0.001
23	0.096	0.334	0.165	Gd	0.002	0.024	0.002	0.002	0.005	0.003
24	0.019	0.061	0.029	Tb	0.000	0.004	0.001	0.037	0.002	0.0008
25	0.128	0.395	0.214	Dy	0.003	0.024	0.005	0.016	0.009	0.001
26	0.032	0.089	0.055	Ho	0.000	0.004	0.001	0.003	0.001	0.0002
27	0.087	0.277	0.176	Er	0.001	0.007	0.003	0.006	0.007	0.0009
28	0.016	0.039	0.027	Tm	0.002	0.003	0.002	0.006	0.003	0.0008
29	0.111	0.211	0.217	Yb	0.002	0.011	0.002	0.012	0.006	0.0009
30	0.023	0.037	0.035	Lu	0.000	0.001	0.000	0.003	0.001	0.0005
31	0.060	0.253	0.066	Hf	0.001	0.007	0.005	0.012	0.006	0.002
32	0.003	0.023	0.008	Ta	0.001	0.001	0.001	0.062	0.000	0.0007
33	0.008	0.001	0.003	W	0.011	0.004	0.002	0.083	0.009	0.003
34	0.002	0.001	0.000	Tl	0.004	0.002	0.001	0.111	0.001	0.0007
35	0.042	0.077	0.877	Pb	0.201	0.114	0.202	0.561	0.186	0.0007
36	0.002	0.001	0.019	Bi	0.008	0.004	0.007	0.525	0.004	0.0006
37	0.020	0.056	0.025	Th	0.001	0.001	0.001	0.001	0.001	0.0003
38	0.031	0.014	0.010	U	0.002	0.001	0.001	0.412	0.002	0.0002
39										
40										
41										
42										
43										
44										
45										
46										
47										
48										
49										
50										
51										
52										
53										
54										
55										
56										
57										
58										
59										
60										

Table 8. Oxygen isotopic compositions of SG 009 Ol, Px and an Al-rich chondrule (Ol, Sp).

	ID	phase	$\delta^{17}\text{O}$	1σ	$\delta^{18}\text{O}$	1σ	$\Delta^{17}\text{O}$	1σ
Ol, Px	G18C	ol	+4.47	0.25	+5.38	0.06	+1.62	0.26
	G18D	ol	+3.70	0.28	+4.86	0.07	+1.13	0.28
	G18E	ol	+3.07	0.20	+4.55	0.07	+0.67	0.20
	G9A	ol	+2.84	0.31	+4.48	0.09	+0.47	0.31
	OL	ol	+2.59	0.29	+3.45	0.07	+0.78	0.30
	G9C	ol	+3.29	0.32	+5.25	0.07	+0.52	0.32
	G9D	ol	+3.47	0.20	+5.56	0.08	+0.53	0.21
	G18A	px	+3.94	0.25	+6.33	0.09	+0.59	0.25
	G18B	px	+3.55	0.31	+5.79	0.06	+0.50	0.31
	G18F	px	+4.53	0.26	+7.40	0.09	+0.63	0.27
	G18G	px	+4.73	0.21	+7.30	0.08	+0.87	0.21
G18H	px	+4.15	0.35	+7.32	0.07	+0.29	0.35	
G18I	px	+3.99	0.30	+7.05	0.07	+0.27	0.30	
Al-rich chondrule	G1B	ol	-1.47	0.35	+0.14	0.05	-1.54	0.35
	G1H	ol	-0.19	0.29	+2.02	0.07	-1.26	0.30
	G1I	ol	+1.47	0.40	+3.25	0.15	-0.25	0.40
	G1A	sp	-1.74	0.33	-1.04	0.08	-1.19	0.33
	G1C	sp	-1.77	0.29	-0.94	0.07	-1.27	0.29
	G1D	sp	-1.30	0.29	-1.63	0.06	-0.44	0.30
	G1E	sp	-1.07	0.28	-1.29	0.08	-0.39	0.29
G1G	sp	-0.69	0.31	-0.98	0.10	-0.18	0.31	

Table 9. Stepwise combustion data for Sierra Gorda 009 (13.44 mg).

T (°C)	²⁰ Ne ^a	²⁰ Ne/ ²² Ne	²¹ Ne/ ²² Ne	⁴⁰ Ar ^a	⁴⁰ Ar/ ³⁶ Ar	N ^b	δ ¹⁵ N	C ^b	δ ¹³ C
200	165.2	11.4(1)	0.0300(5)	24107.1	286.0(3)	14.65	7.41(23)	31.19	-7.76(24)
300	19.4	13.7(1)	-	4233.6	286.7(1.2)	13.36	10.3(2)	204.84	-3.63(13)
400	8.5	12.8(2)	0.0507(54)	1287.2	282.5(3.4)	9.03	18.5(3)	72.87	-7.43(25)
500	5.8	11.4(2)	0.0877(62)	974.7	279.8(4.9)	5.15	28.3(3)	150.67	3.06(16)
600	5.1	10.4(2)	0.147(8)	773.8	265.9(7.7)	3.62	27.2(4)	429.39	2.94(27)
700	4.8	5.79(8)	0.521(10)	602.7	53.3(1)	2.29	31.5(2)	700.89	3.51(13)
800	5.1	4.26(5)	0.632(10)	488.8	55.4(1)	1.53	30.3(3)	10.07	4.42(1.30)
900	5.4	4.26(5)	0.633(9)	475.4	56.6(1)	1.93	28.8(3)	9.63	-13.1(1.1)
1000	5.6	4.94(6)	0.545(9)	504.5	56.7(1)	1.93	23.4(3)	8.06	n.a.
1100	6.9	5.04(5)	0.551(6)	922.6	283.1(5.8)	1.41	18.2(3)	2.28	-4.01(2.40)
1200	8.0	5.13(5)	0.558(8)	427.1	57.5(1)	0.52	10.4(3)	2.93	-1.38(54)
1300	10.0	5.38(5)	0.573(7)	407.7	56.9(1)	1.28	-13.7(3)	3.45	5.95(47)
1400	33.0	8.56(5)	0.324(3)	4672.6	277.3(1.2)	4.33	-2.52(35)	1.26	-4.6(7)
total	282.8	9.23(6)	0.4898(69)	39878.0	219.0(7)	61.05	14.4(3)	1627.52	1.6(2)

^a x 10⁻⁸ cm³ STP/g

^b ppm

5-10% uncertainty in absolute concentrations of noble gases

Numbers in parentheses refer to the last digits and are 1σ-uncertainties.

n.a. – not analysed

Table. 10. Carbon and nitrogen abundances and isotopic compositions of SG 009. Literature data on other chondrites (Grady and Wright 2003) are given for comparison.

	C (ppm)	$\delta^{13}\text{C}$ (‰)	N (ppm)	$\delta^{15}\text{N}$ (‰)
Sierra Gorda 009	1628	1.6	61	14.4
OC	300-6000	-24 to -12	1-25	-20 to +100
EH (graphite)	1500-7000	-9 to +4	10-100	-30 to -10
CI, CM, CR	0.4-5 wt.%	-12 to -5	500-2000	+20 to +180
CO, CV, CK	0.1-1.1 wt.%	-25 to -8	5-200	-50 to +100
CH, Bencubbin	0.35-1.21	+0.3 to +6	20-280	+150 to +900

1
2
3
4
5
6
7
8
9
10
11
12
13
14
15
16
17
18
19
20
21
22
23
24
25
26
27
28
29
30
31
32
33
34
35
36
37
38
39
40
41
42
43
44
45
46
47
48
49
50
51
52
53
54
55
56
57
58
59
60

Fig. 1.

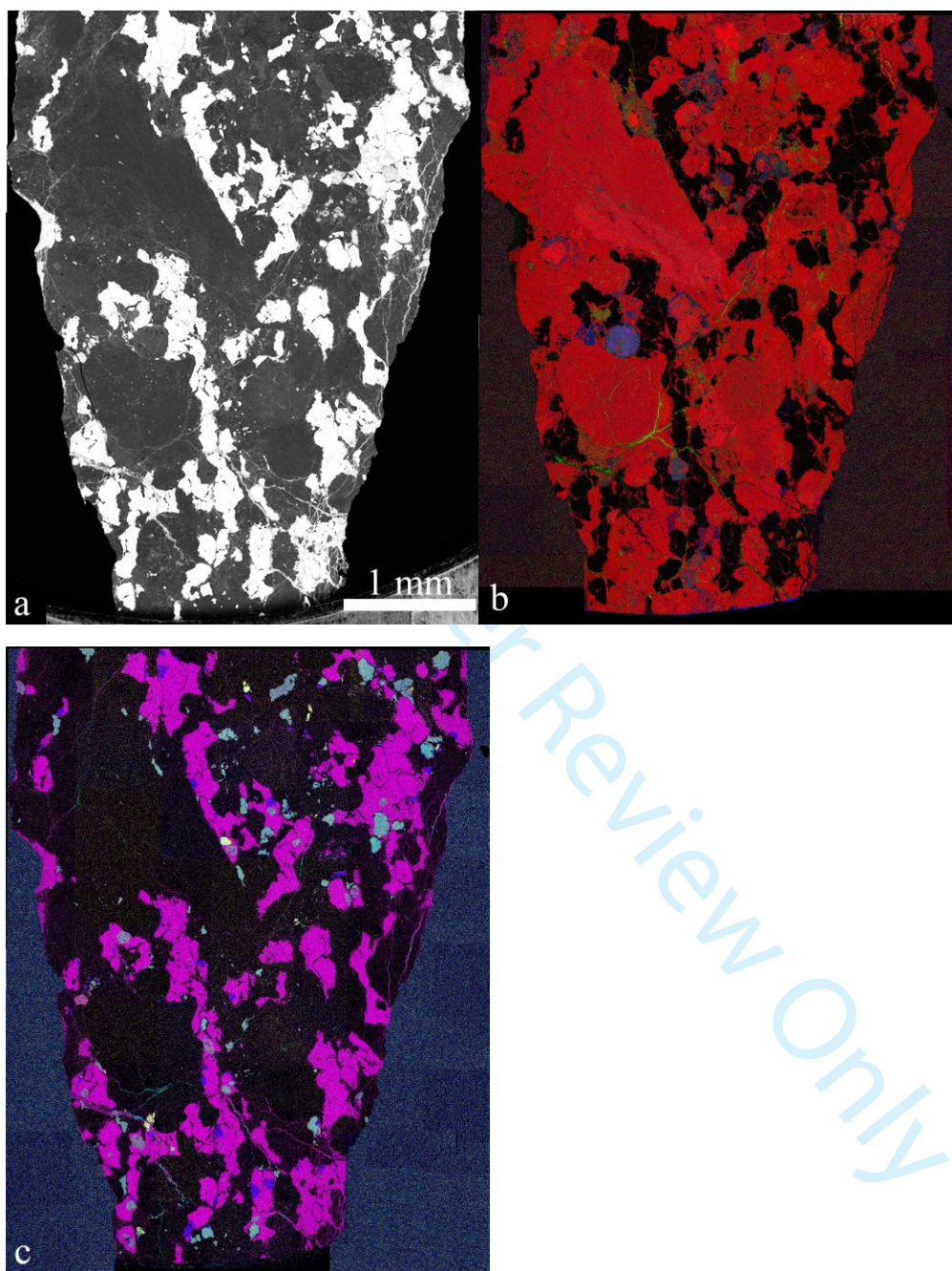
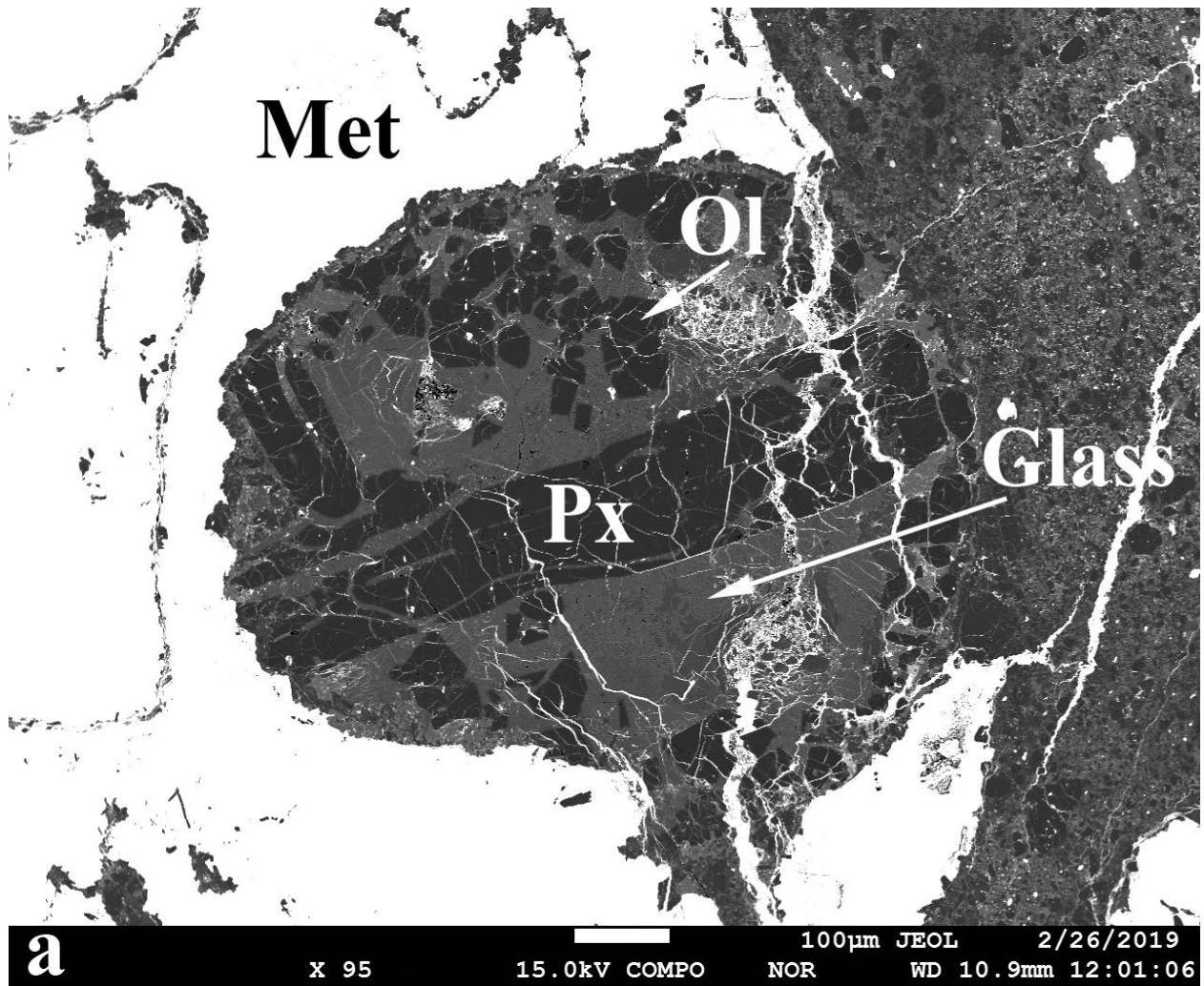
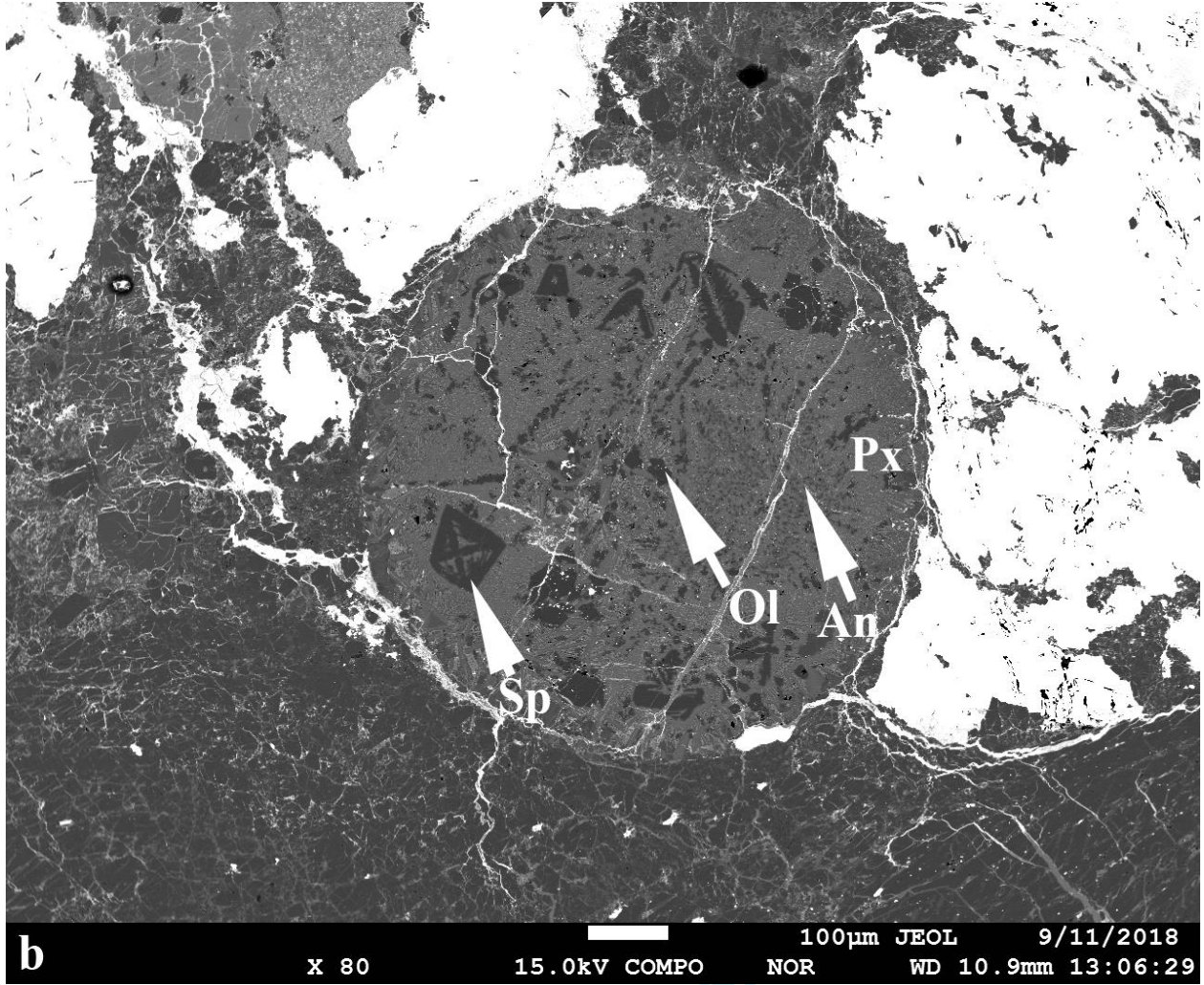
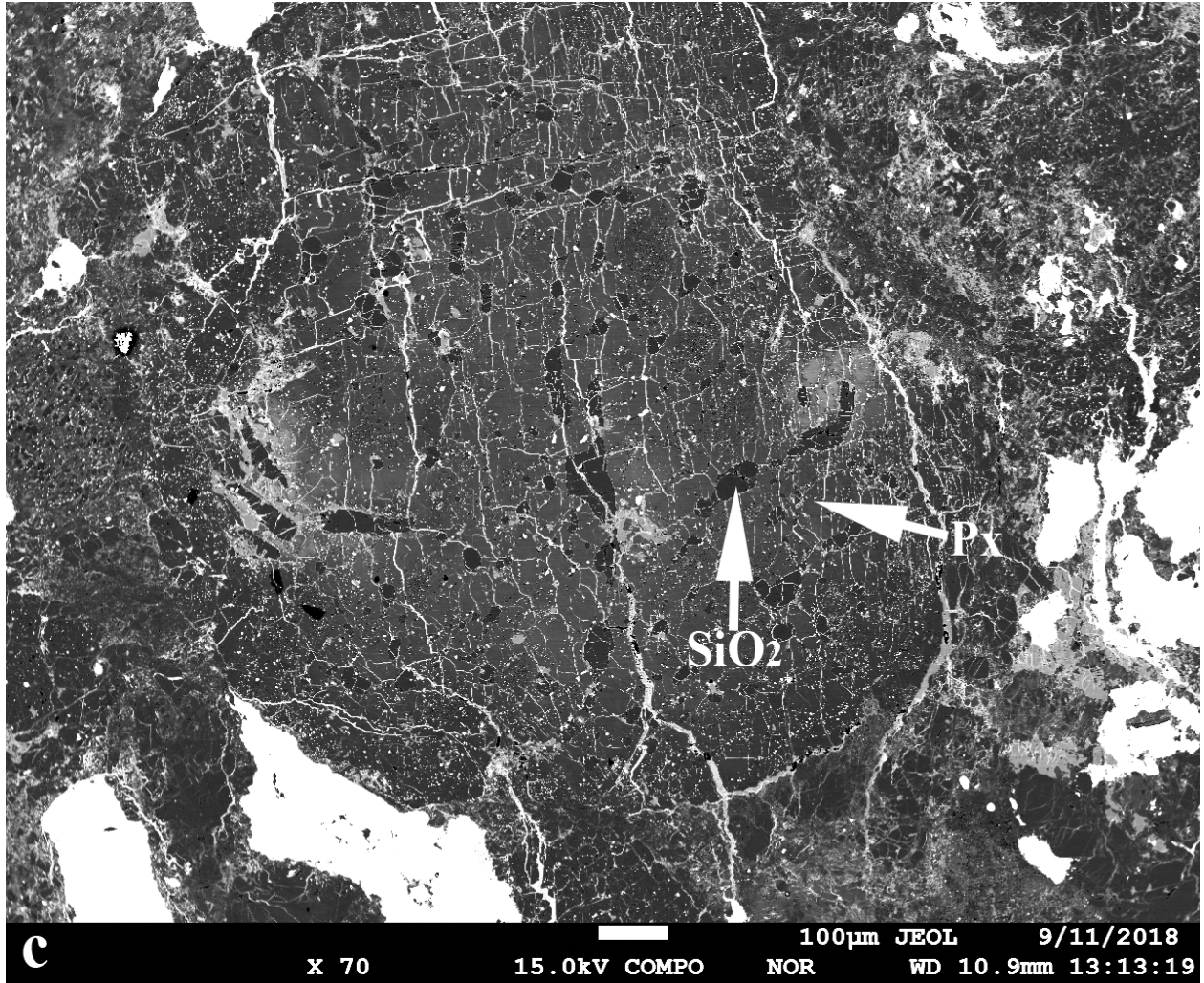


Fig. 2.

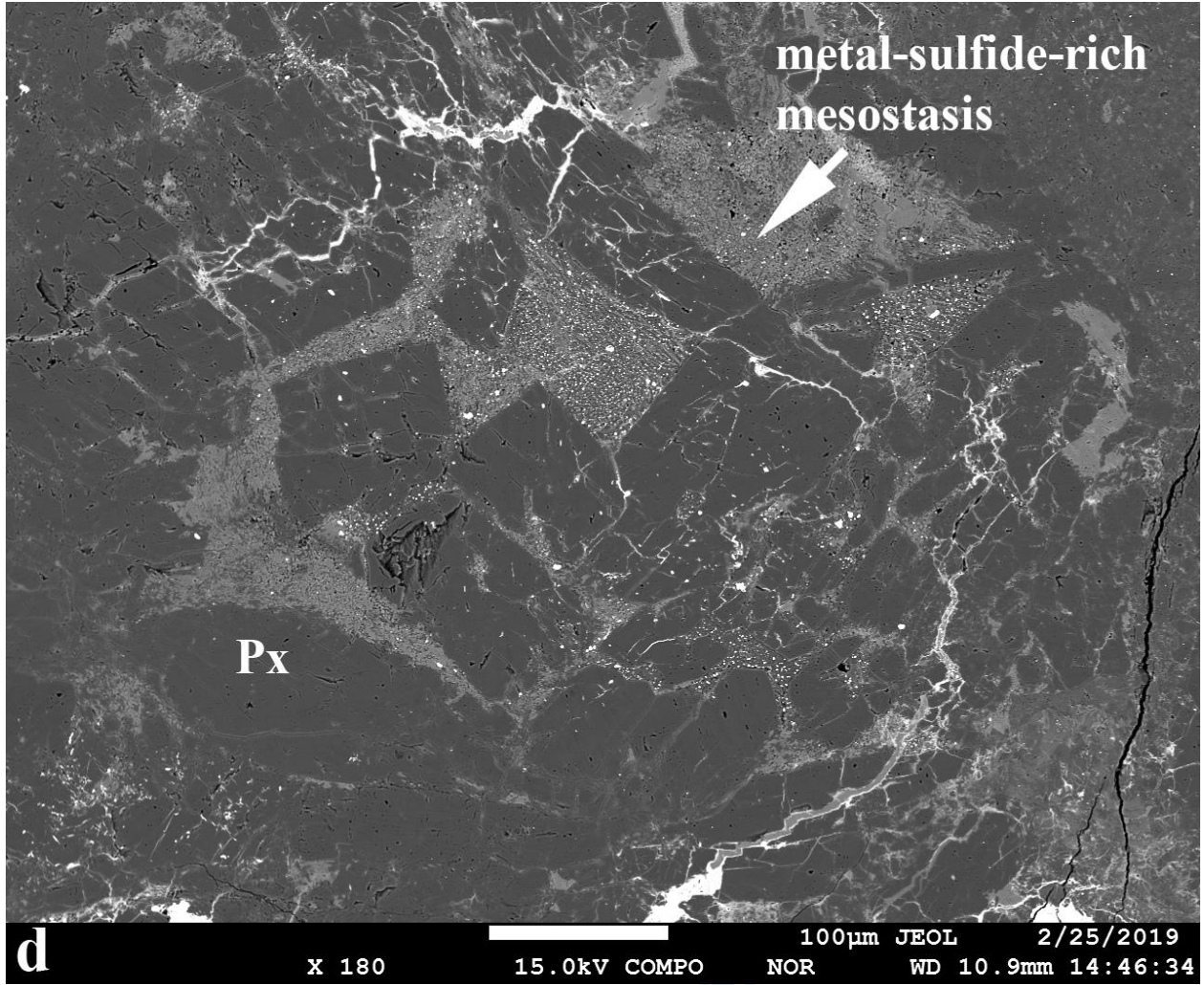


1
2
3
4
5
6
7
8
9
10
11
12
13
14
15
16
17
18
19
20
21
22
23
24
25
26
27
28
29
30
31
32
33
34
35
36
37
38
39
40
41
42
43
44
45
46
47
48
49
50
51
52
53
54
55
56
57
58
59
60

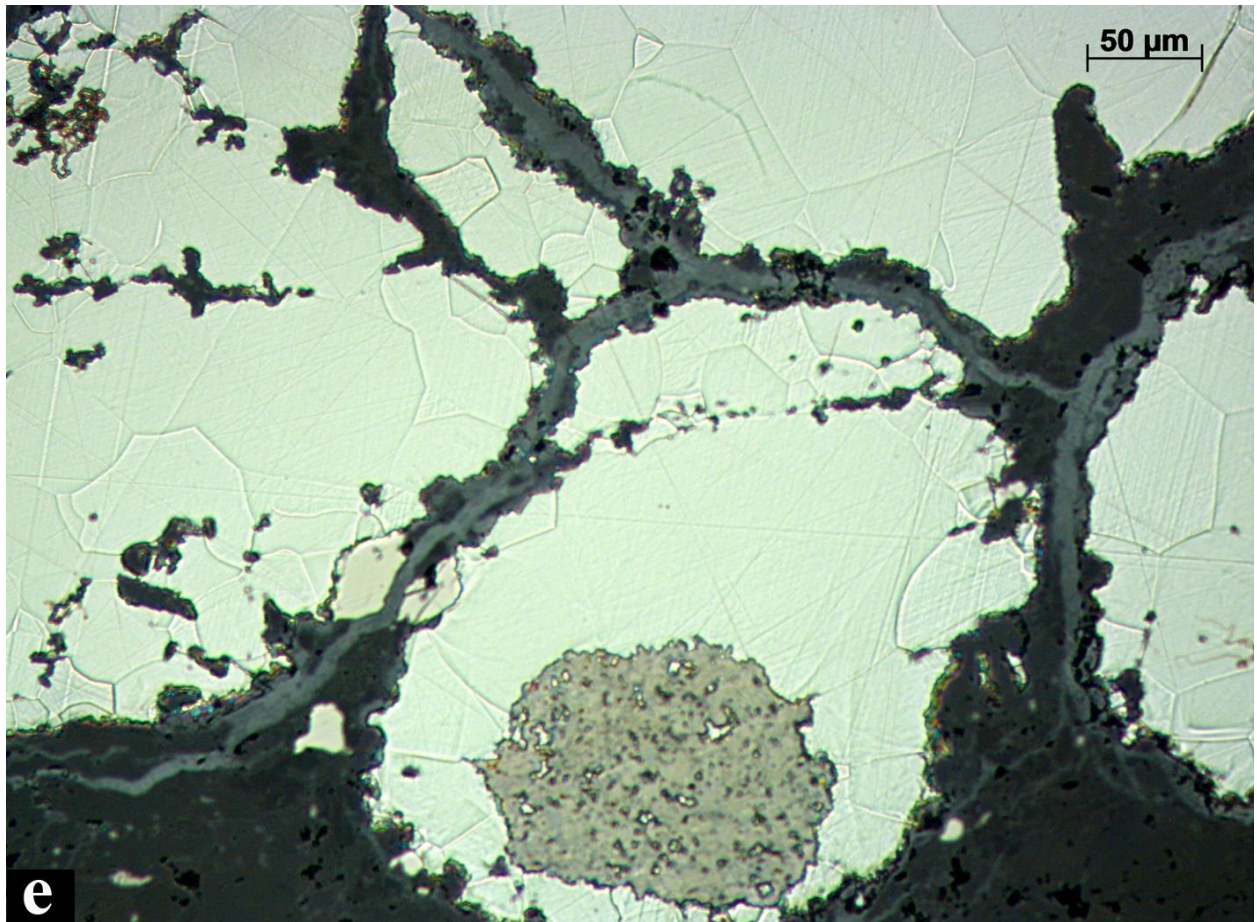




1
2
3
4
5
6
7
8
9
10
11
12
13
14
15
16
17
18
19
20
21
22
23
24
25
26
27
28
29
30
31
32
33
34
35
36
37
38
39
40
41
42
43
44
45
46
47
48
49
50
51
52
53
54
55
56
57
58
59
60

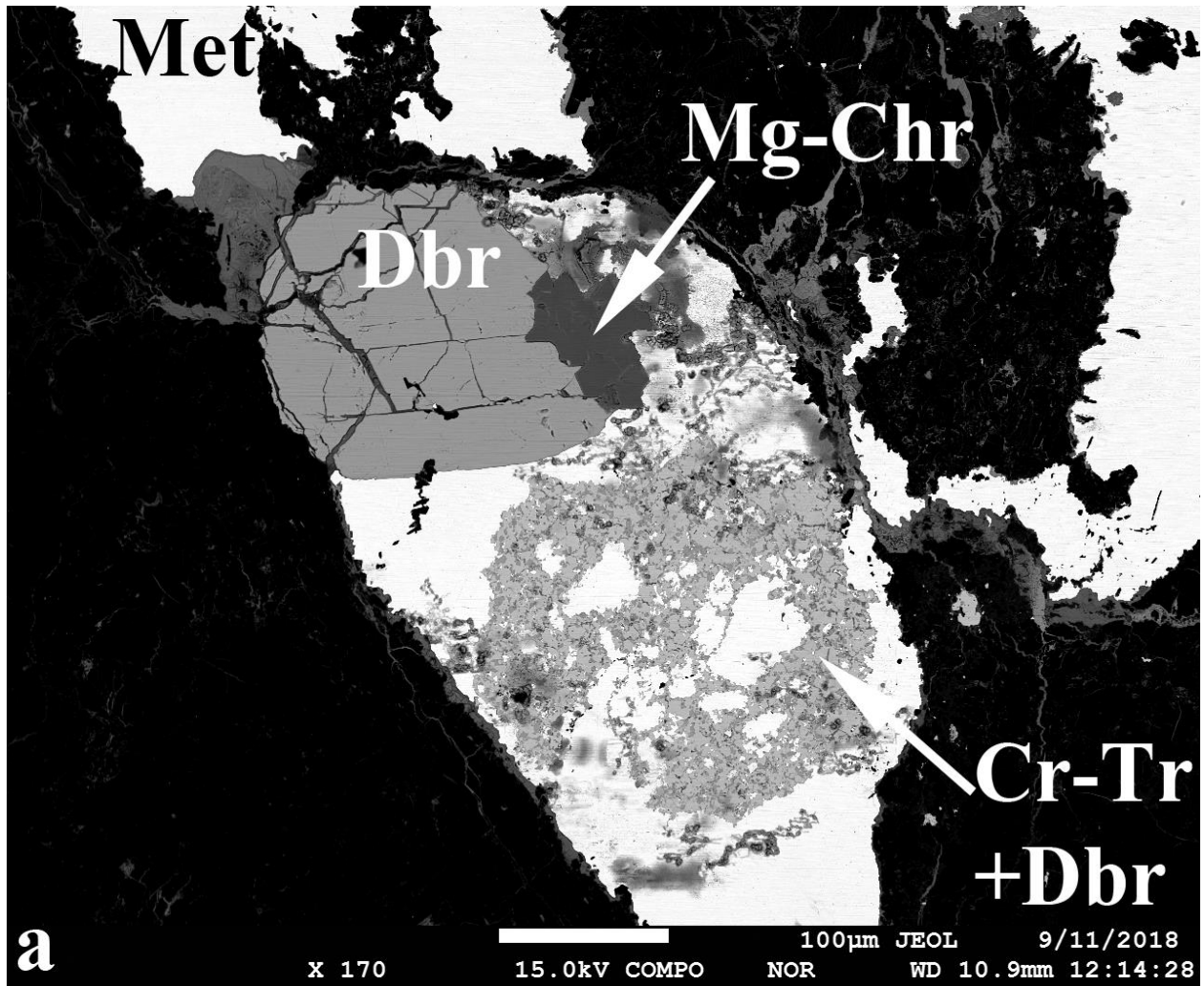


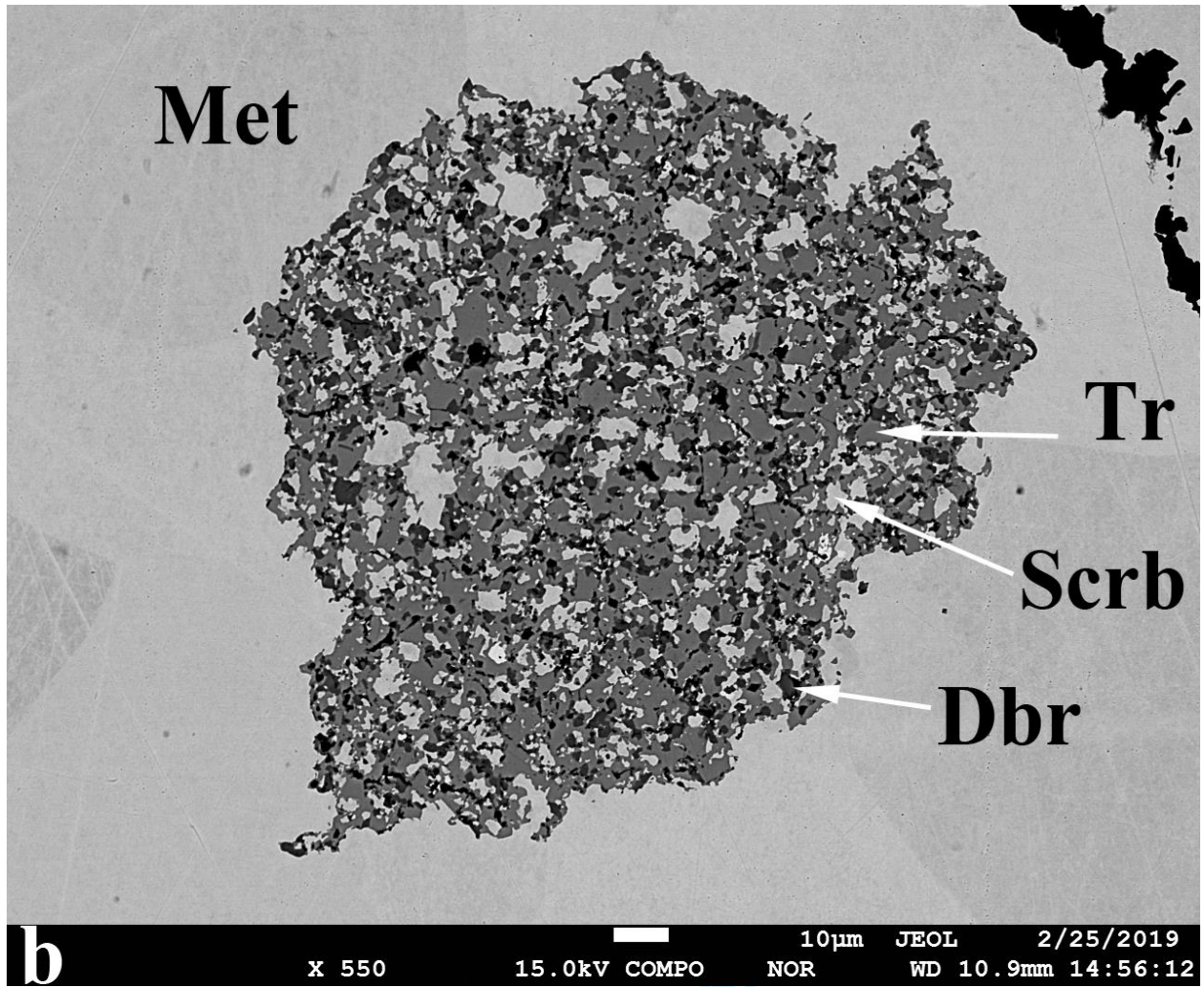
1
2
3
4
5
6
7
8
9
10
11
12
13
14
15
16
17
18
19
20
21
22
23
24
25
26
27
28
29
30
31
32
33
34
35
36
37
38
39
40
41
42
43
44
45
46
47
48
49
50
51
52
53
54
55
56
57
58
59
60



Review Only

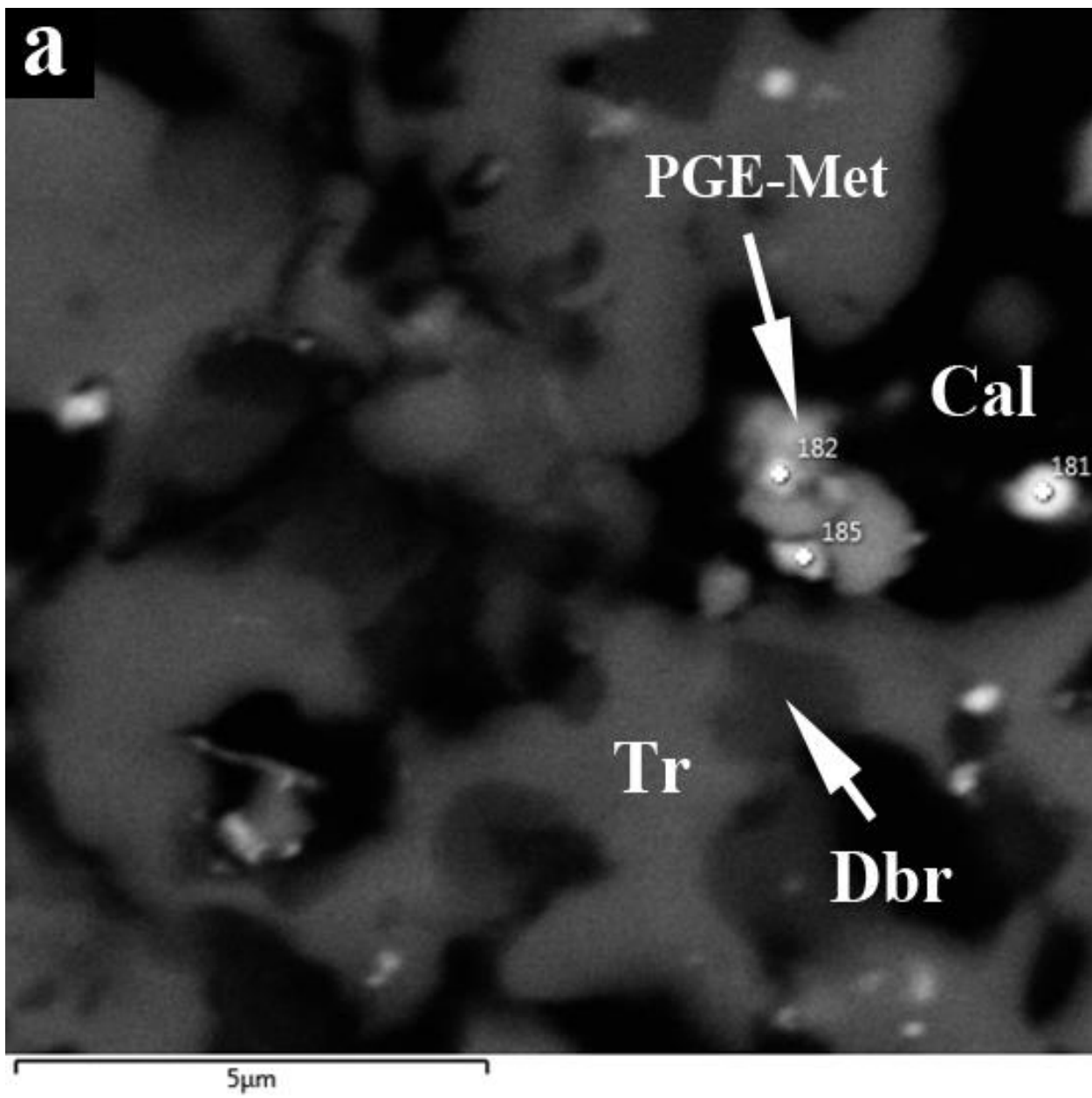
Fig. 3.





1
2
3
4
5
6
7
8
9
10
11
12
13
14
15
16
17
18
19
20
21
22
23
24
25
26
27
28
29
30
31
32
33
34
35
36
37
38
39
40
41
42
43
44
45
46
47
48
49
50
51
52
53
54
55
56
57
58
59
60

Fig. 4.



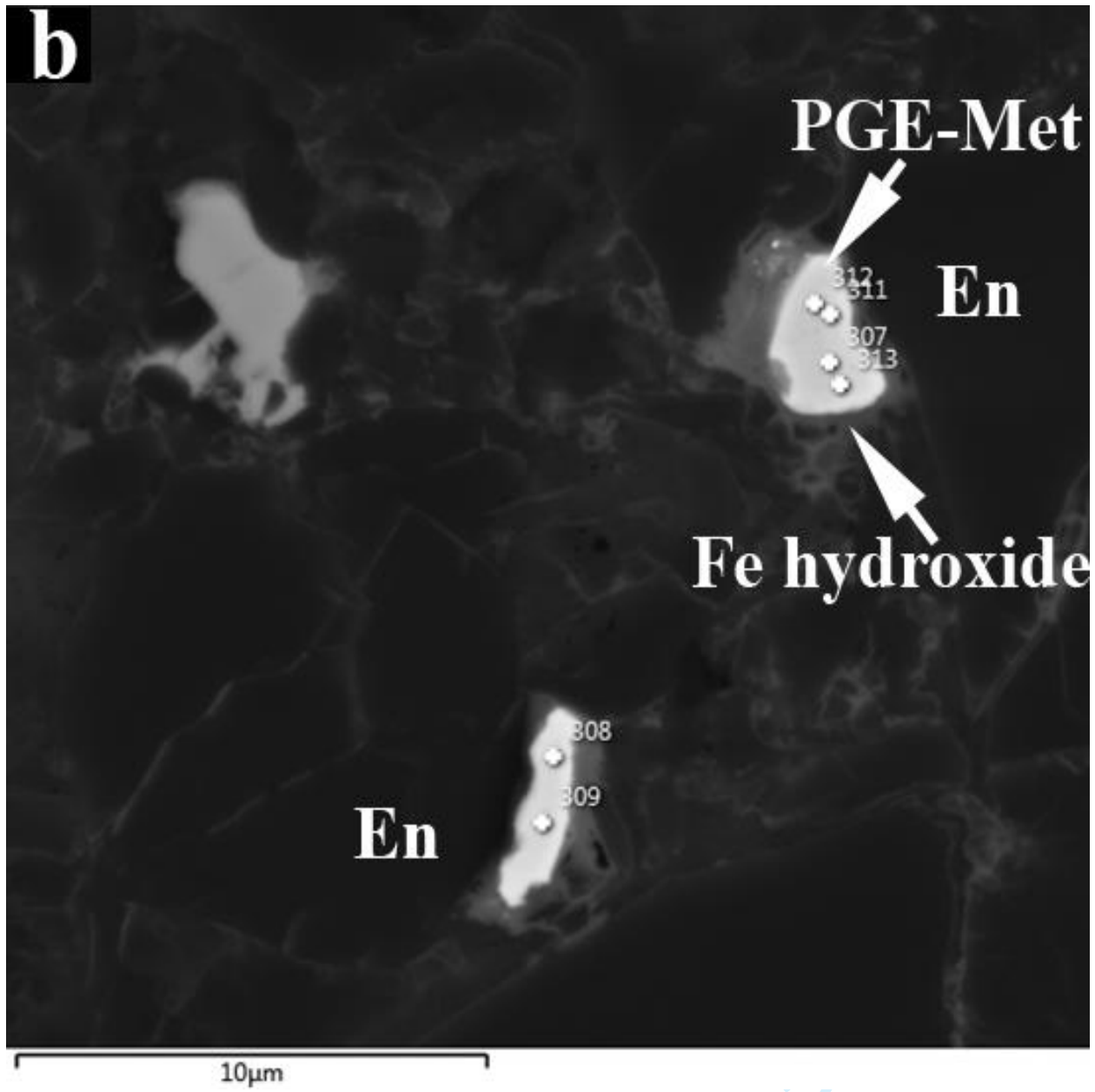
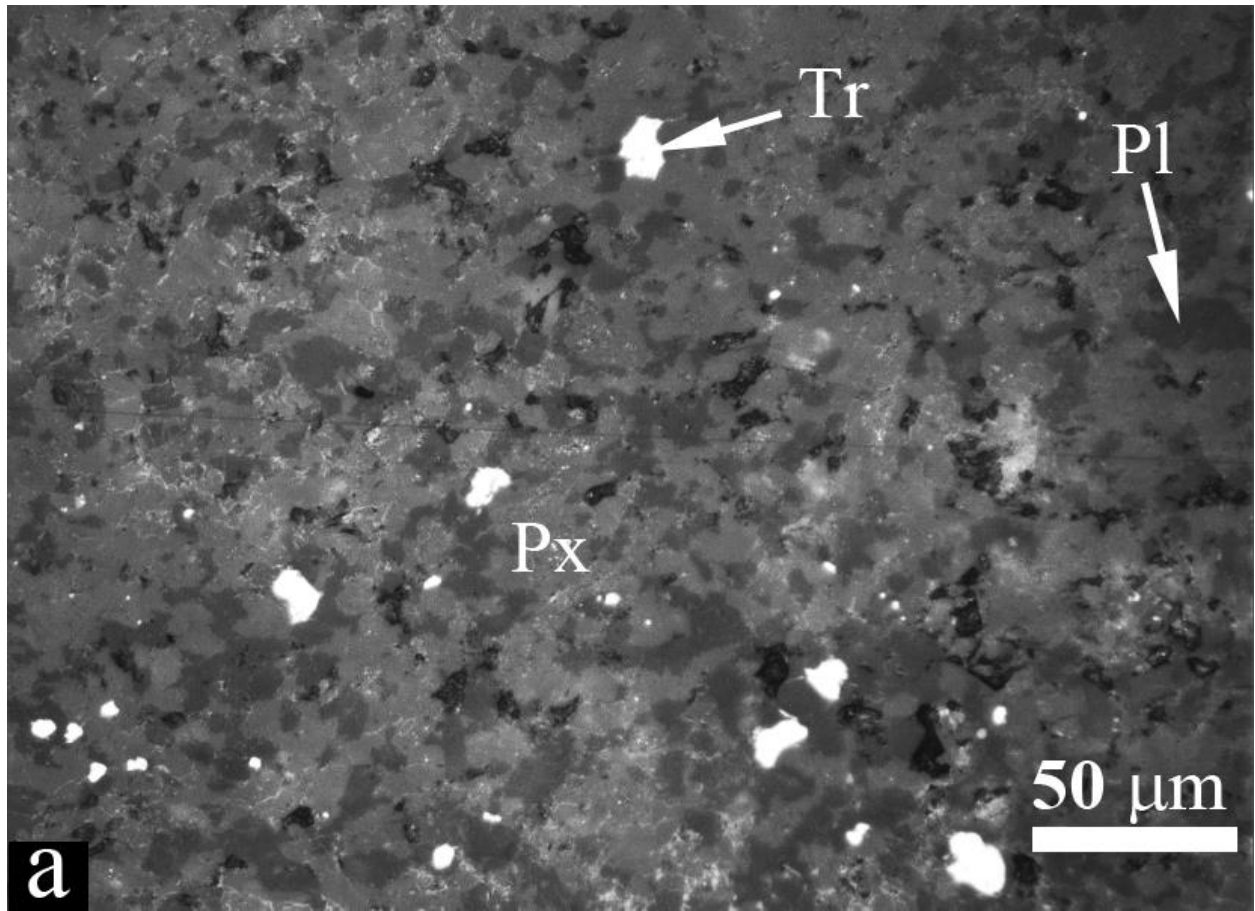
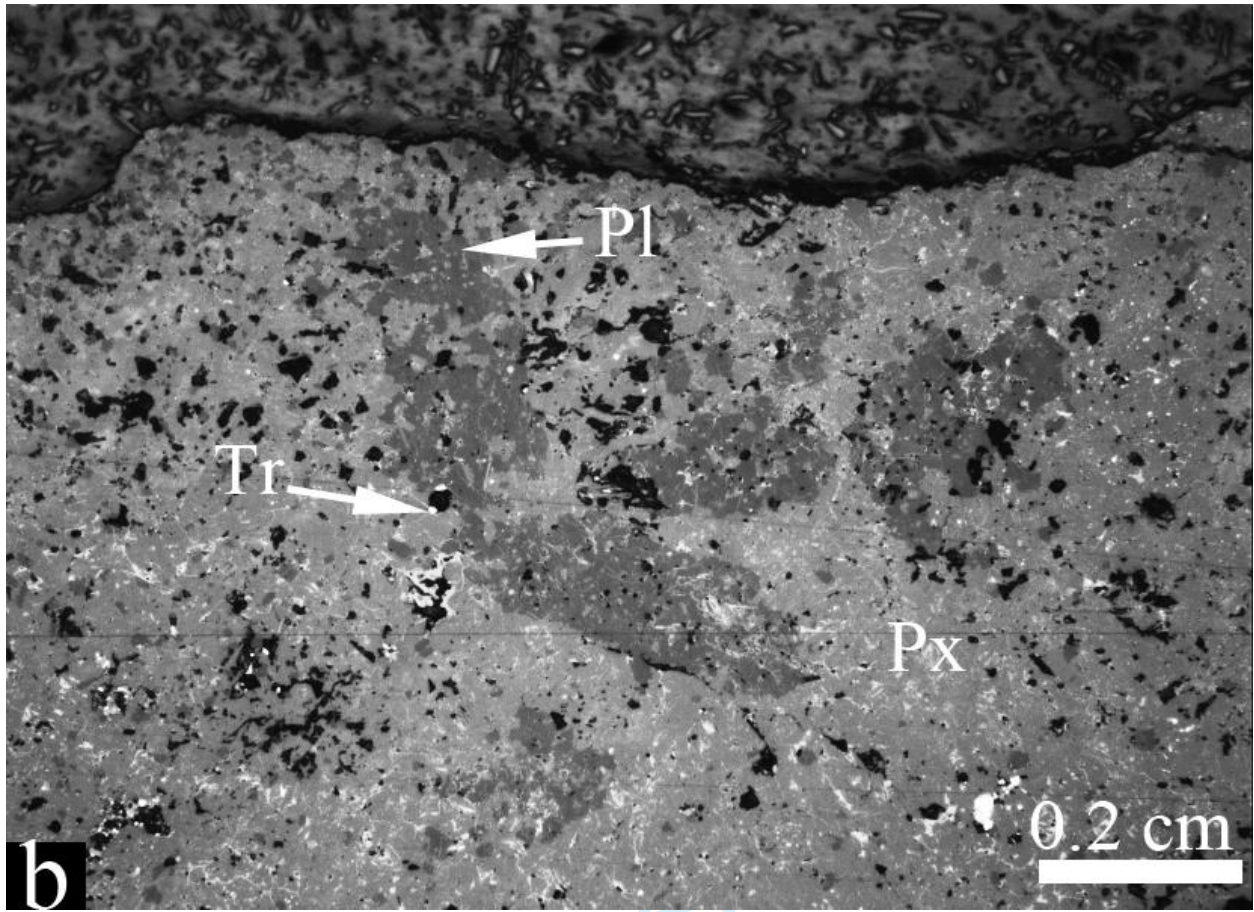


Fig. 5.





1
2
3
4
5
6
7
8
9
10
11
12
13
14
15
16
17
18
19
20
21
22
23
24
25
26
27
28
29
30
31
32
33
34
35
36
37
38
39
40
41
42
43
44
45
46
47
48
49
50
51
52
53
54
55
56
57
58
59
60

Fig. 6.

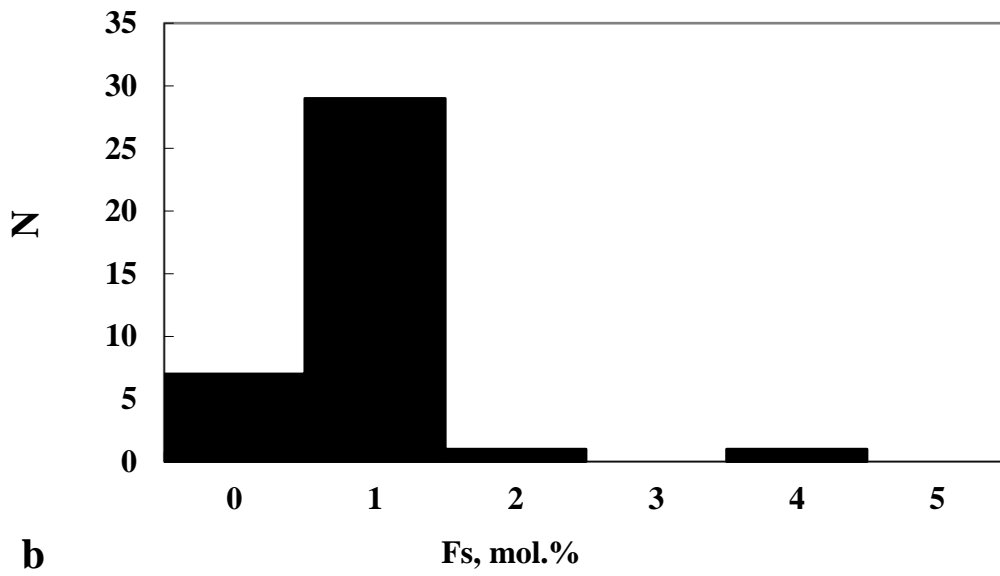
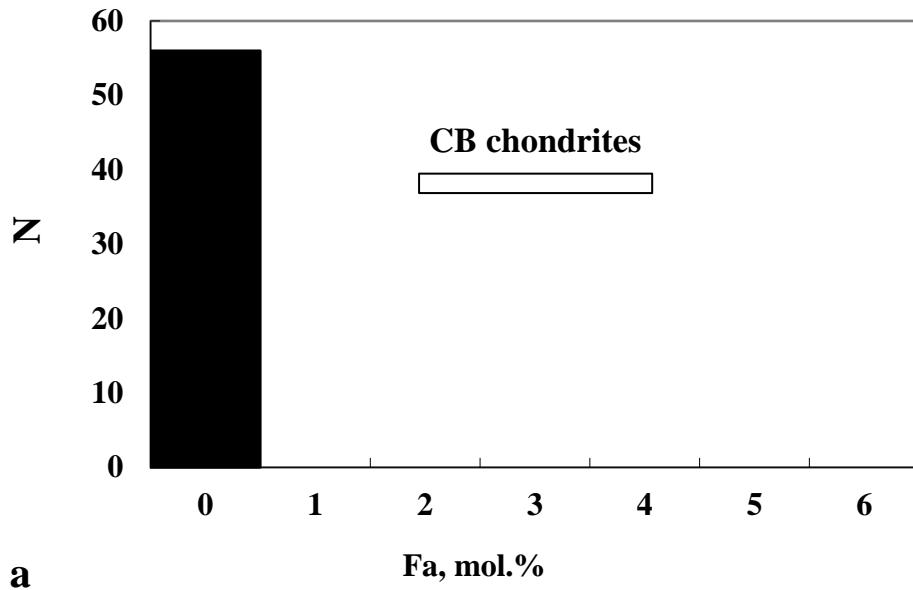
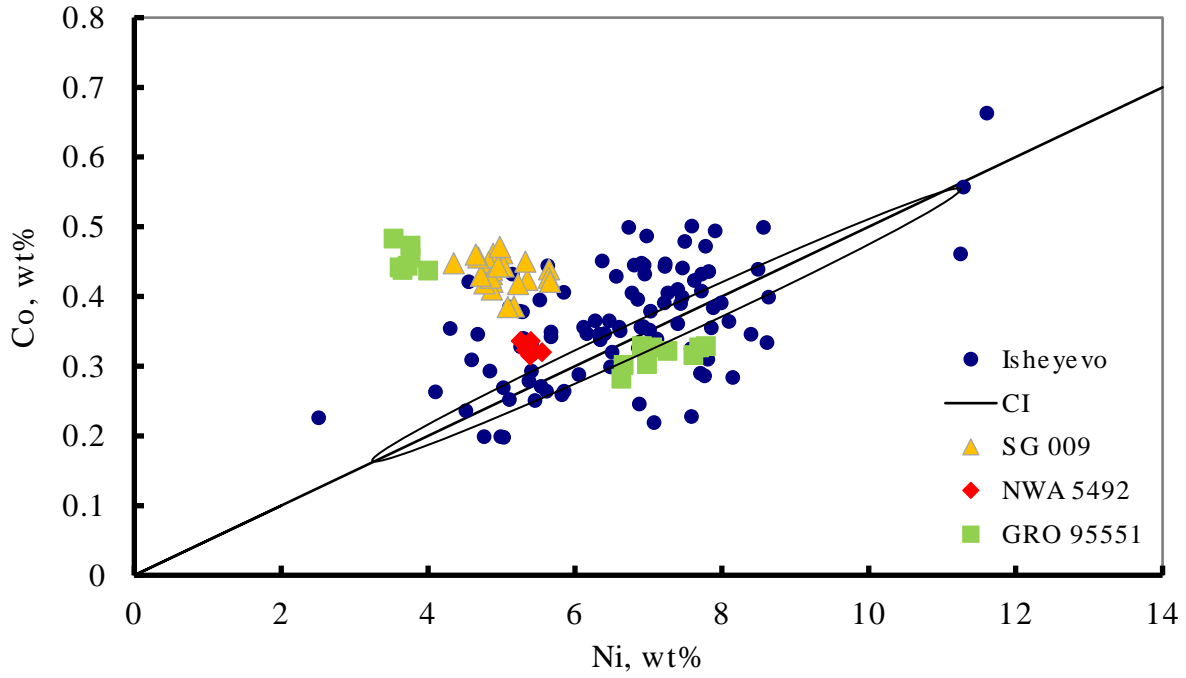


Fig. 7.



Running Head

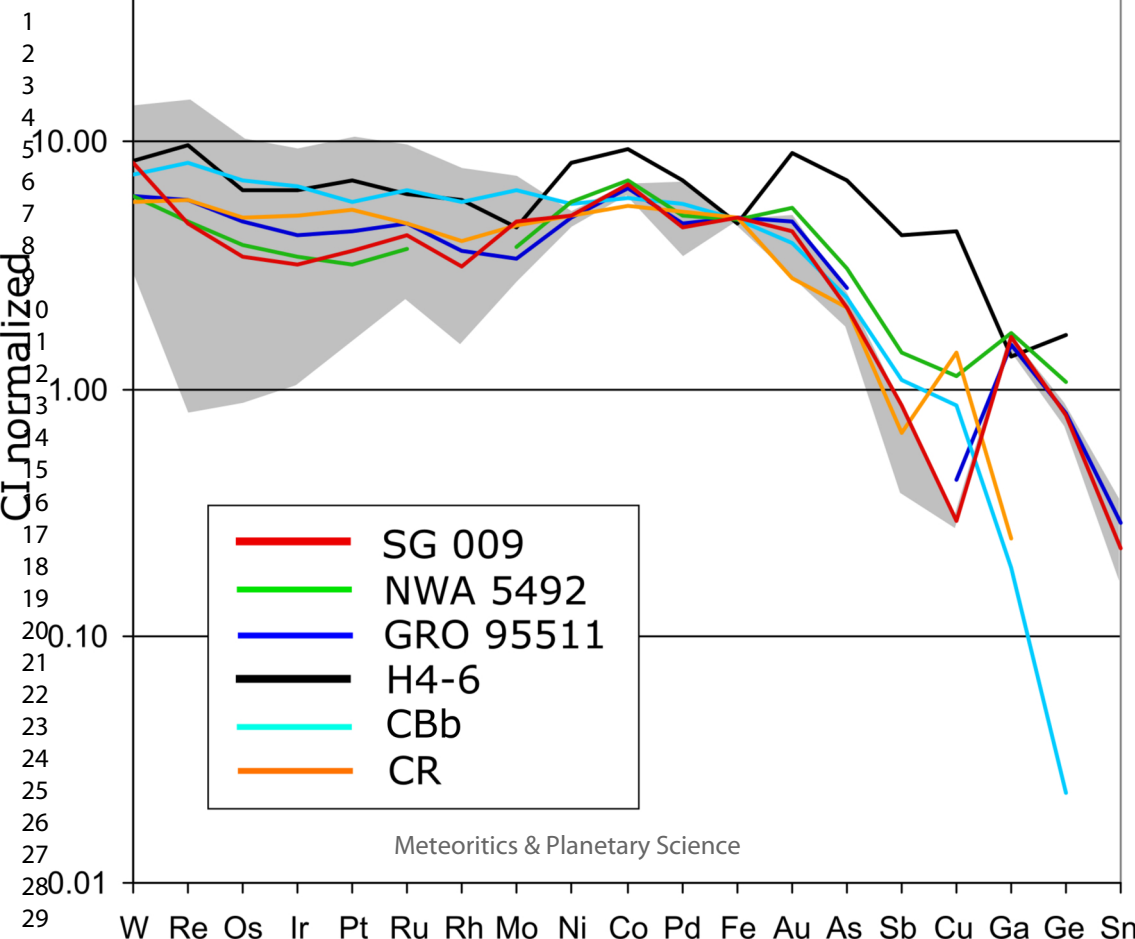
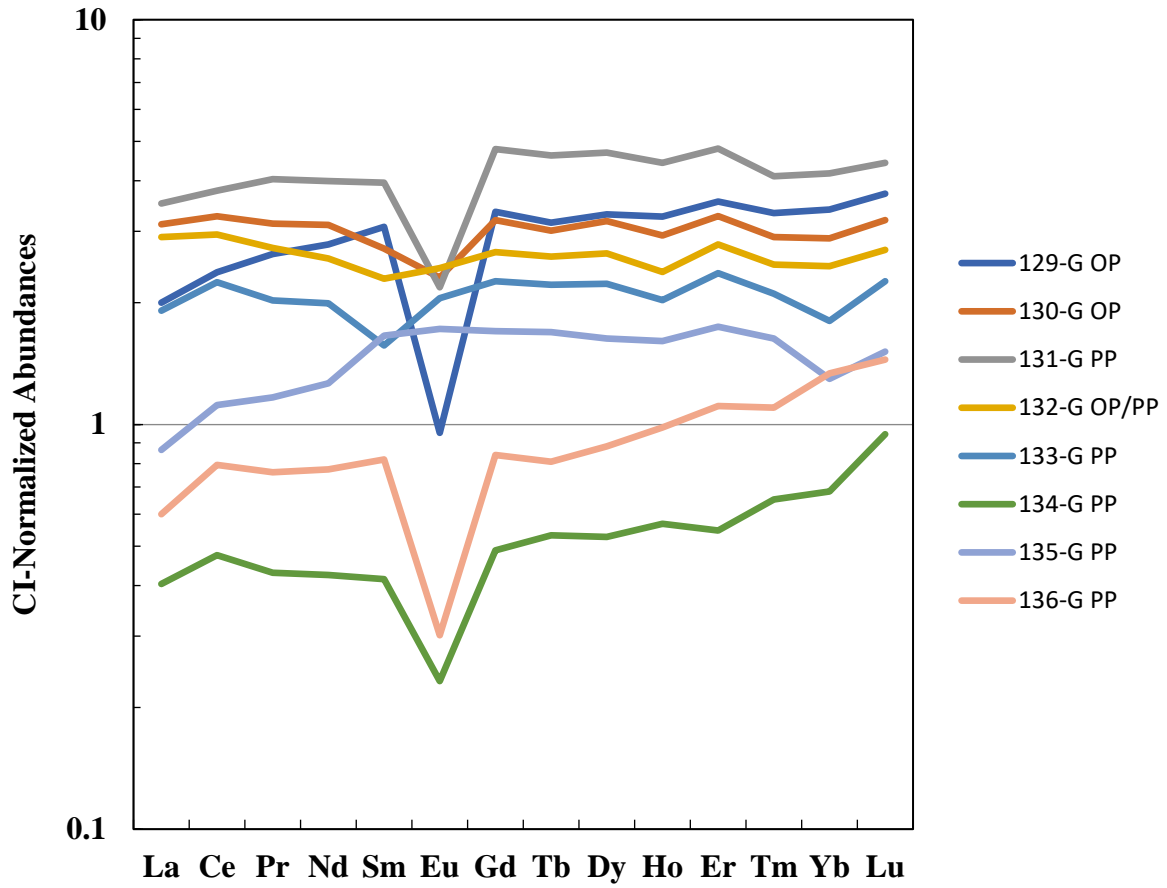
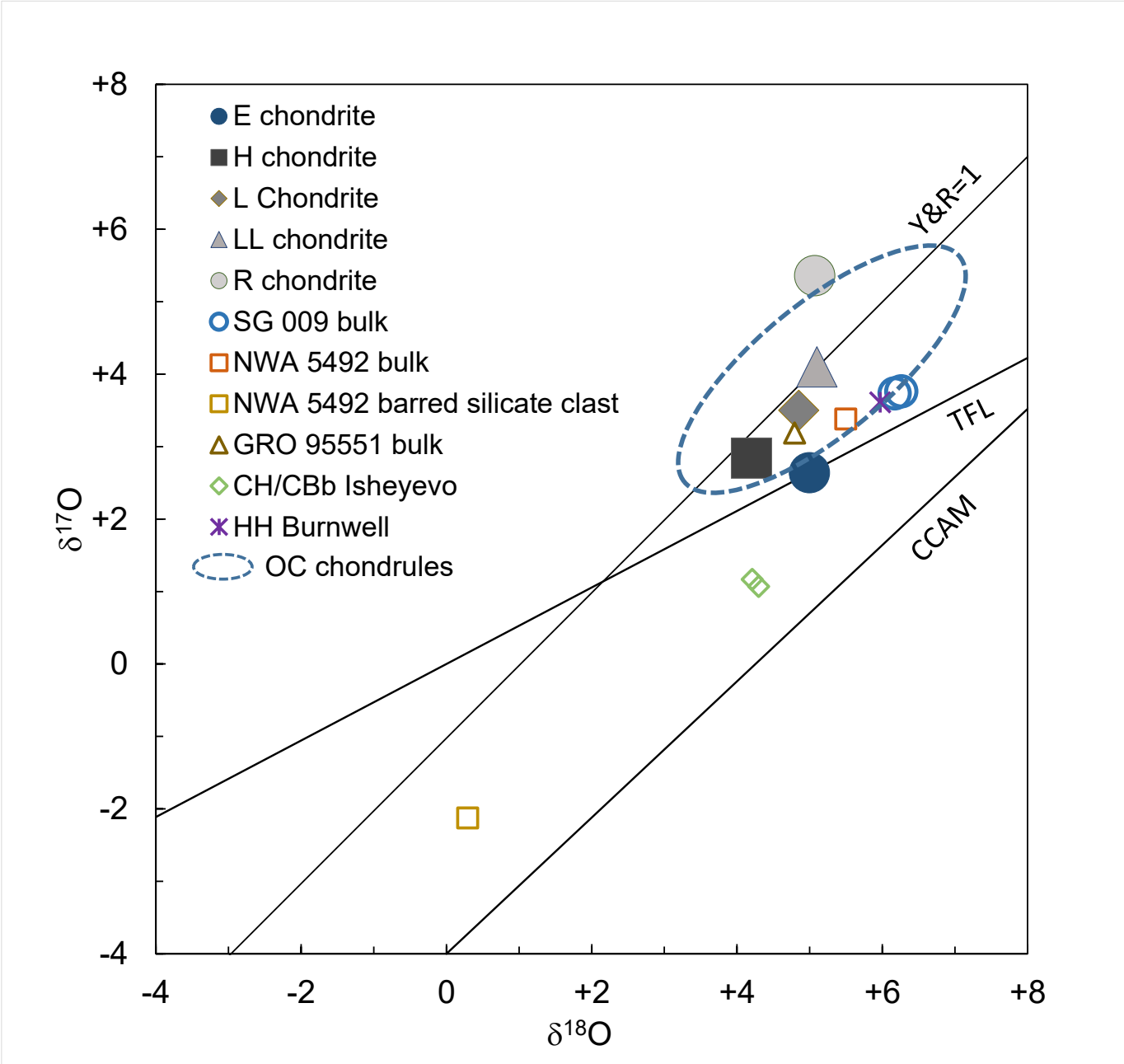


Fig. 9.



1
2
3
4
5
6
7
8
9
10
11
12
13
14
15
16
17
18
19
20
21
22
23
24
25
26
27
28
29
30
31
32
33
34
35
36
37
38
39
40
41
42
43
44
45
46
47
48
49
50
51
52
53
54
55
56
57
58
59
60



1
2
3
4
5
6
7
8
9
10
11
12
13
14
15
16
17
18
19
20
21
22
23
24
25
26
27
28
29
30
31
32
33
34
35
36
37
38
39
40
41
42
43
44
45
46
47
48
49
50
51
52
53
54
55
56
57
58
59
60

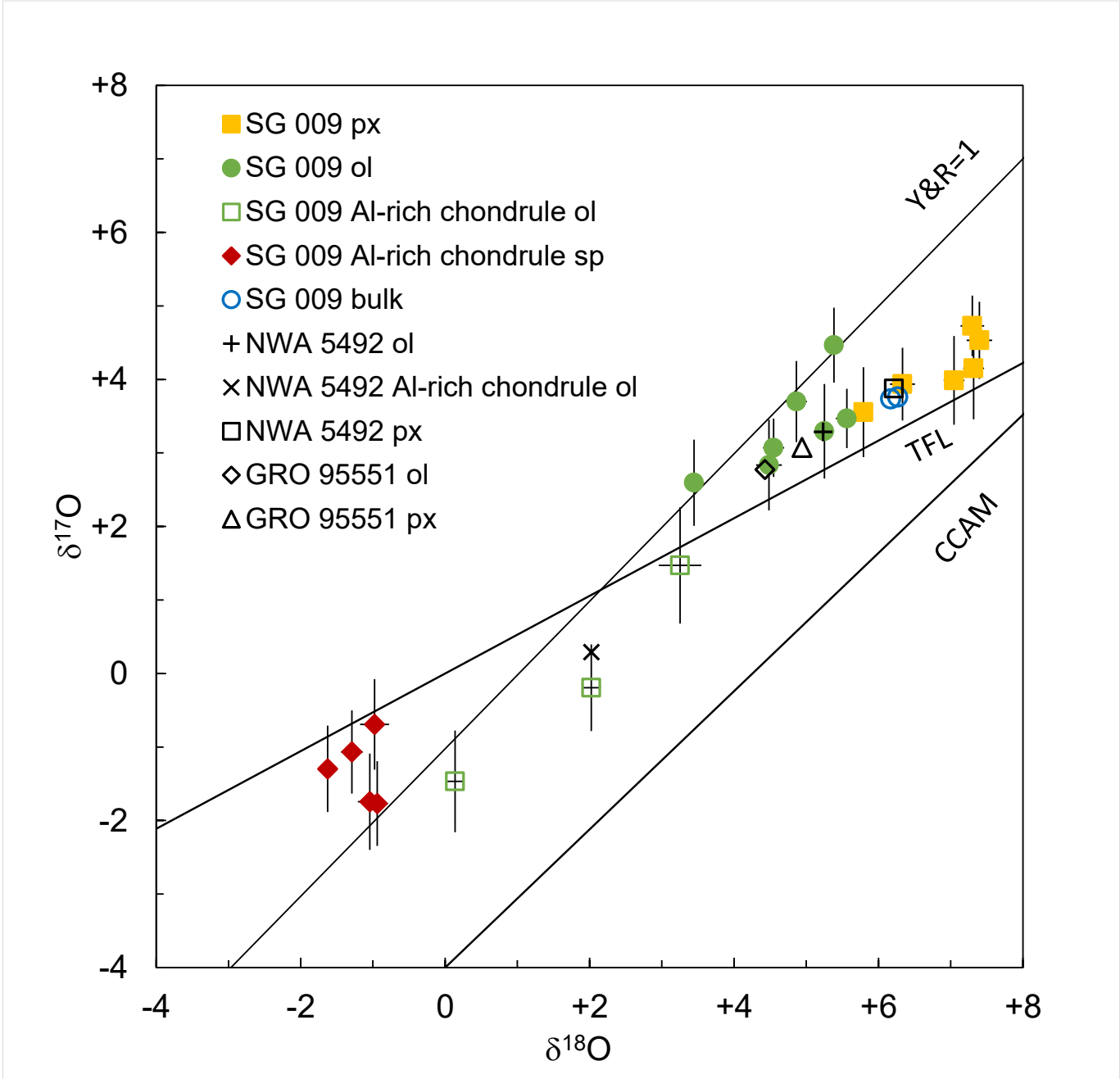


Fig. 12.

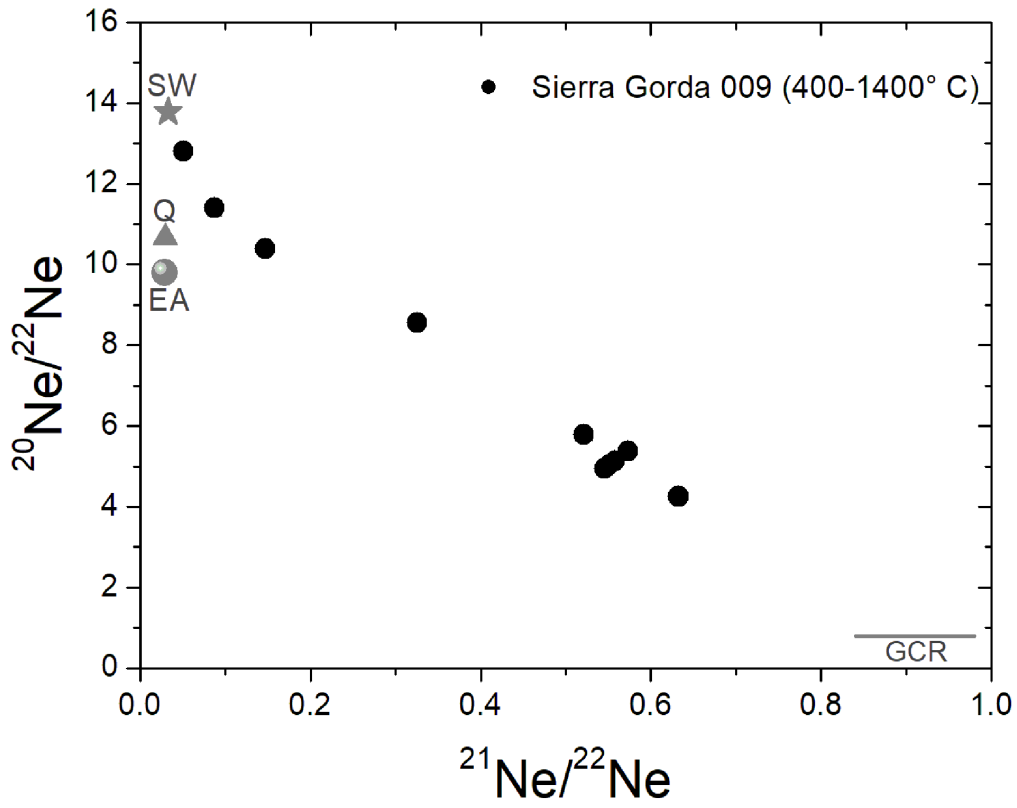


Fig. 13.

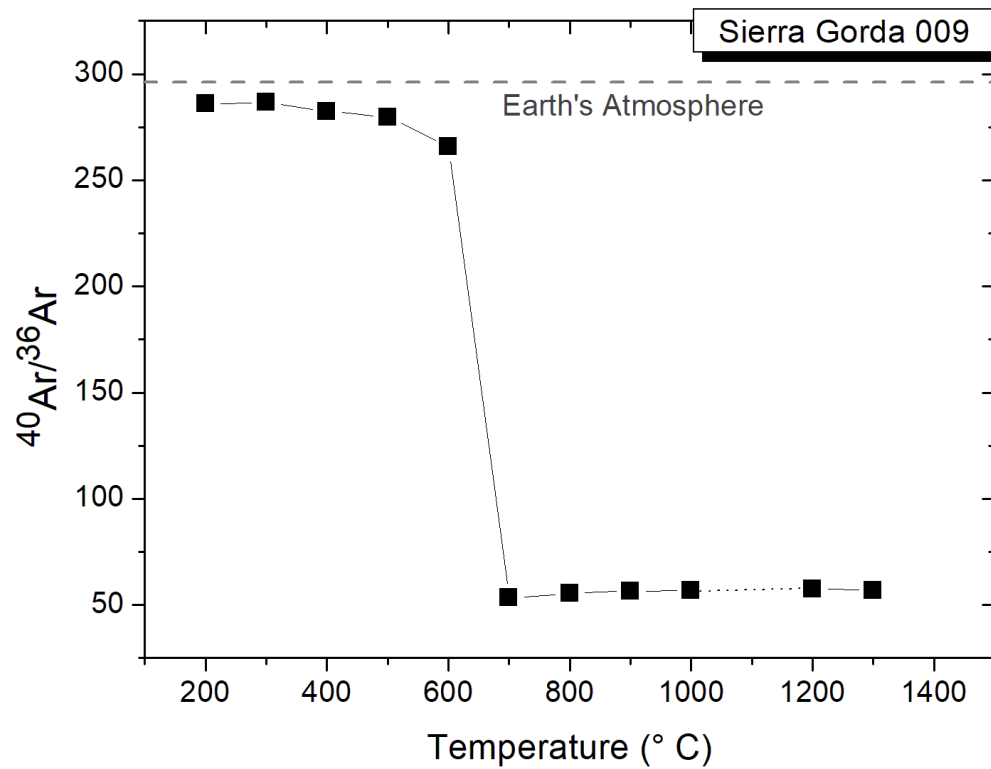


Fig. 14.

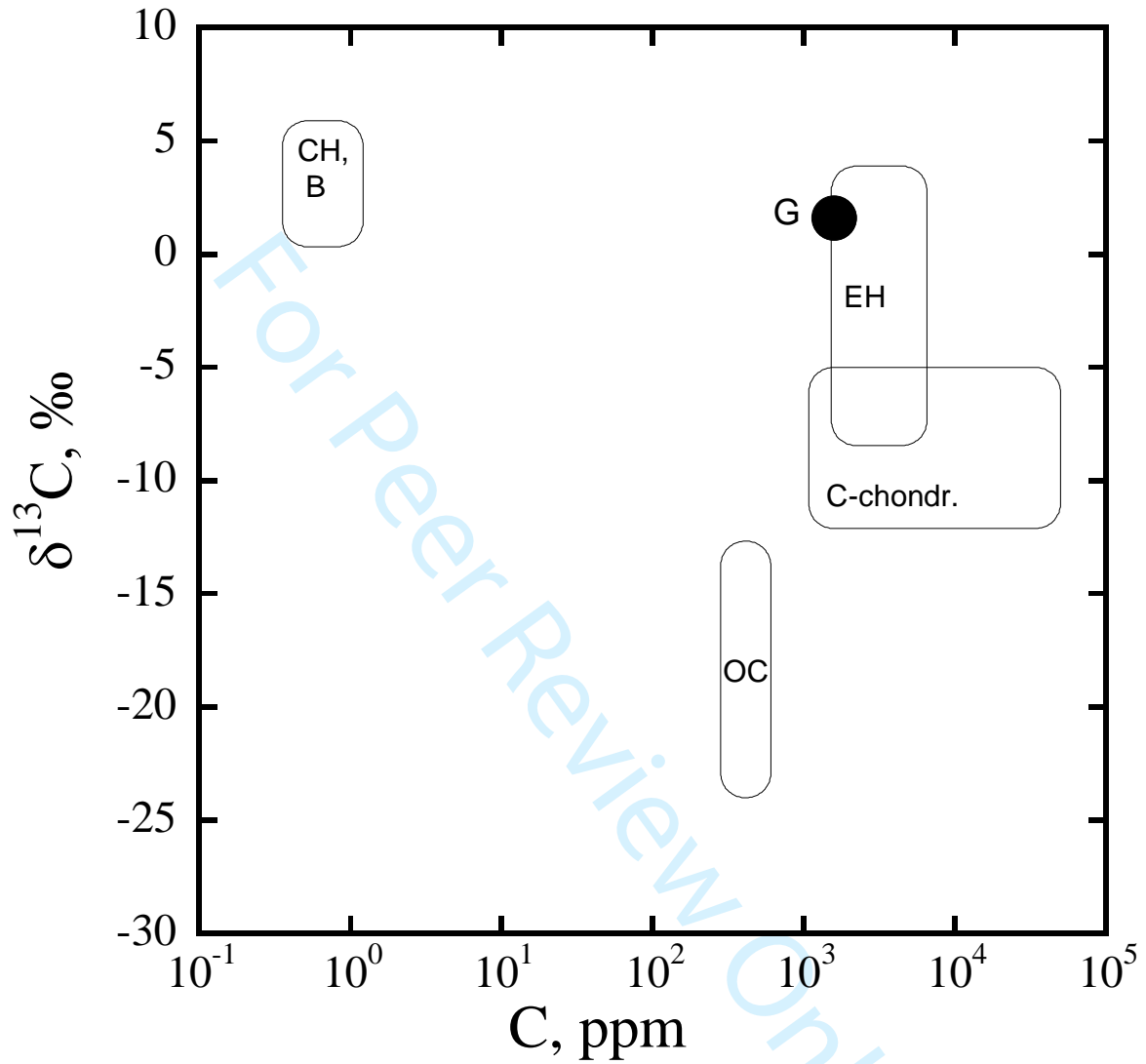
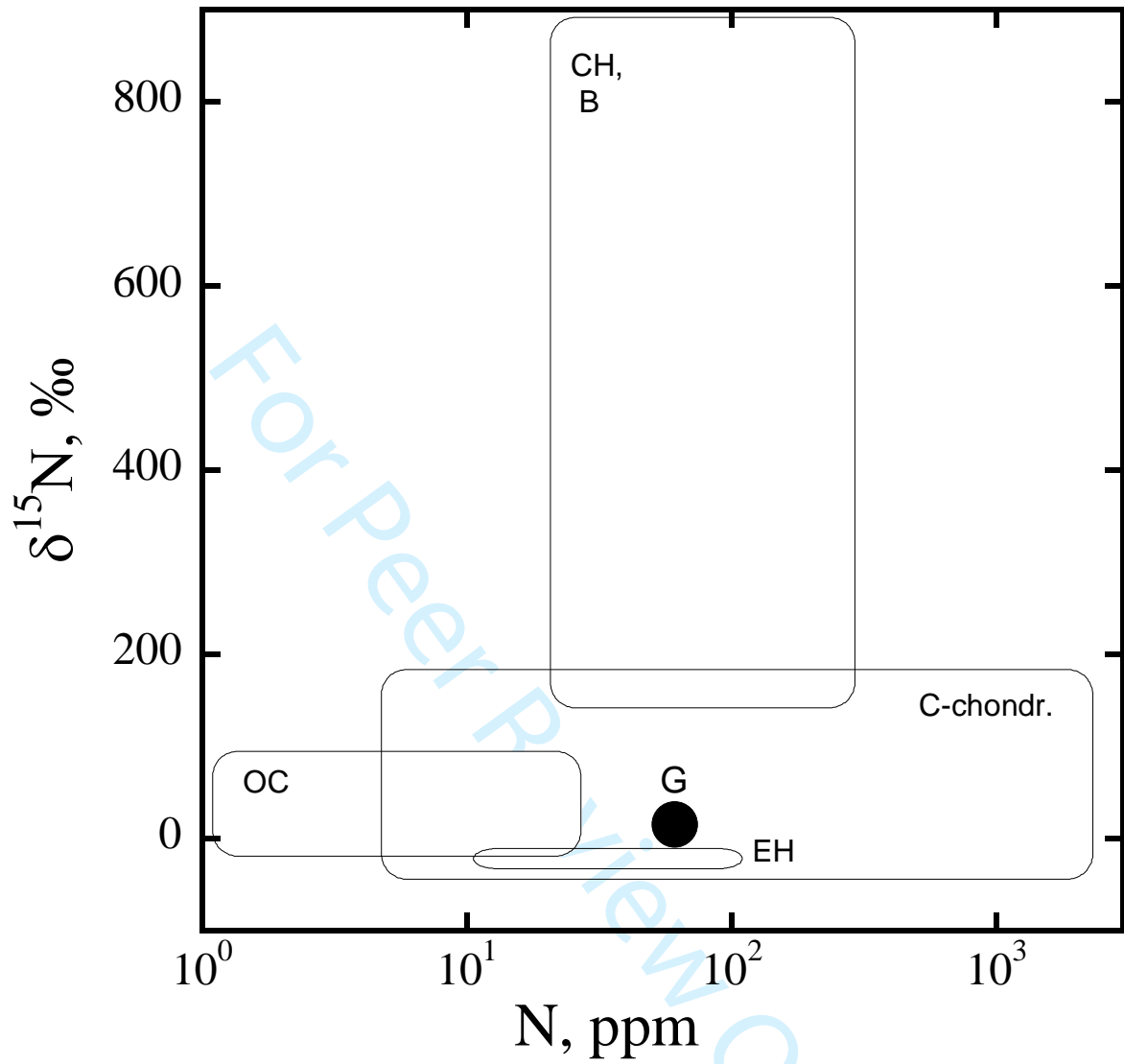


Fig. 15.



1
2
3
4
5
6
7
8
9
10
11
12
13
14
15
16
17
18
19
20
21
22
23
24
25
26
27
28
29
30
31
32
33
34
35
36
37
38



10

CI

0.1

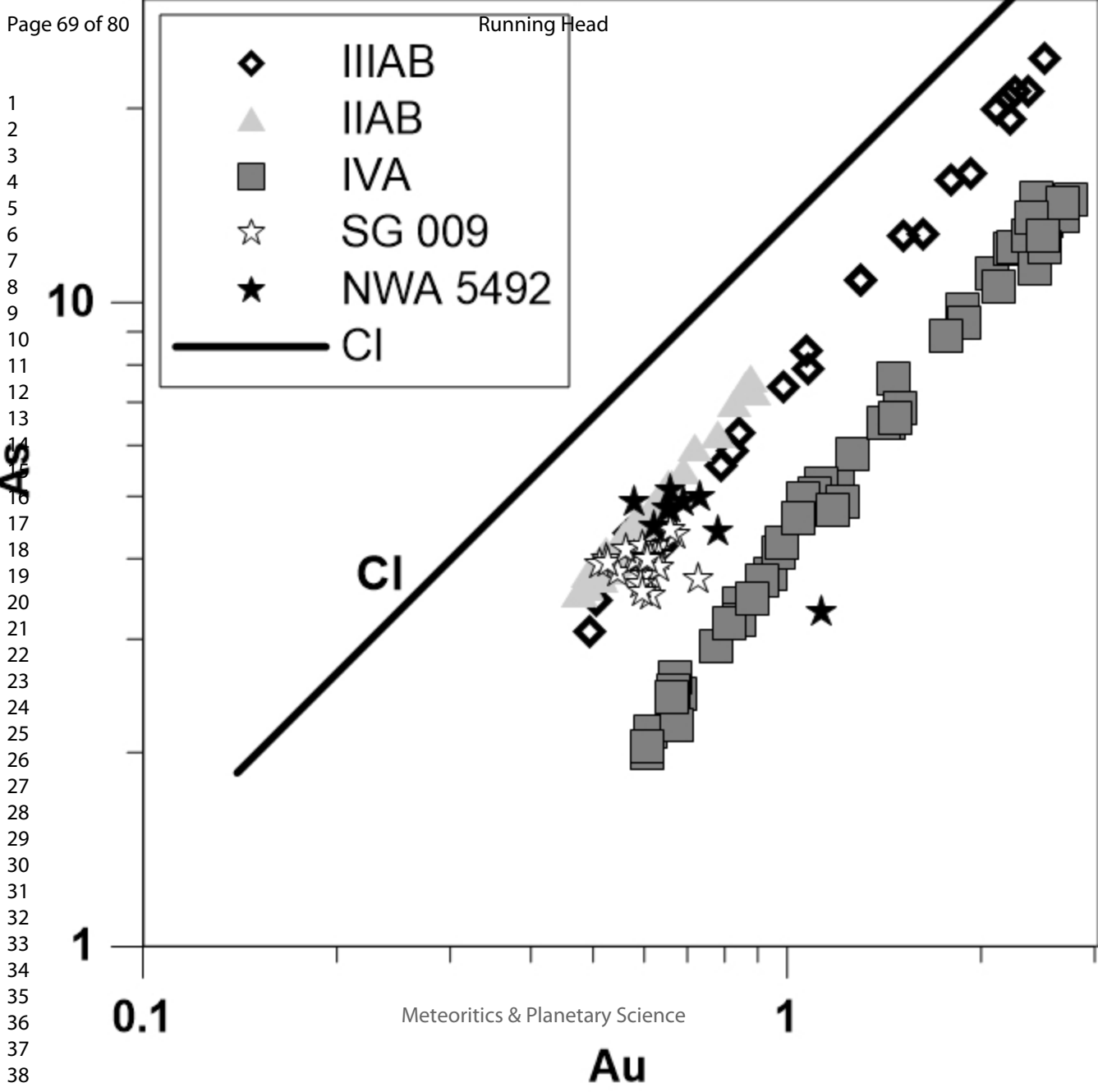
Meteoritics & Planetary Science

1

Au

1

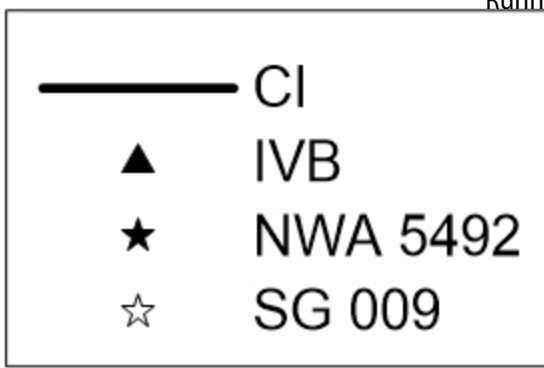
As



1
2
3
4
5
6
7
8
9
10
11
12
13
14
15
16
17
18
19
20
21
22
23
24
25
26
27
28
29
30
31
32
33
34
35
36
37
38
39
40
41
42
43
44
45

10

1



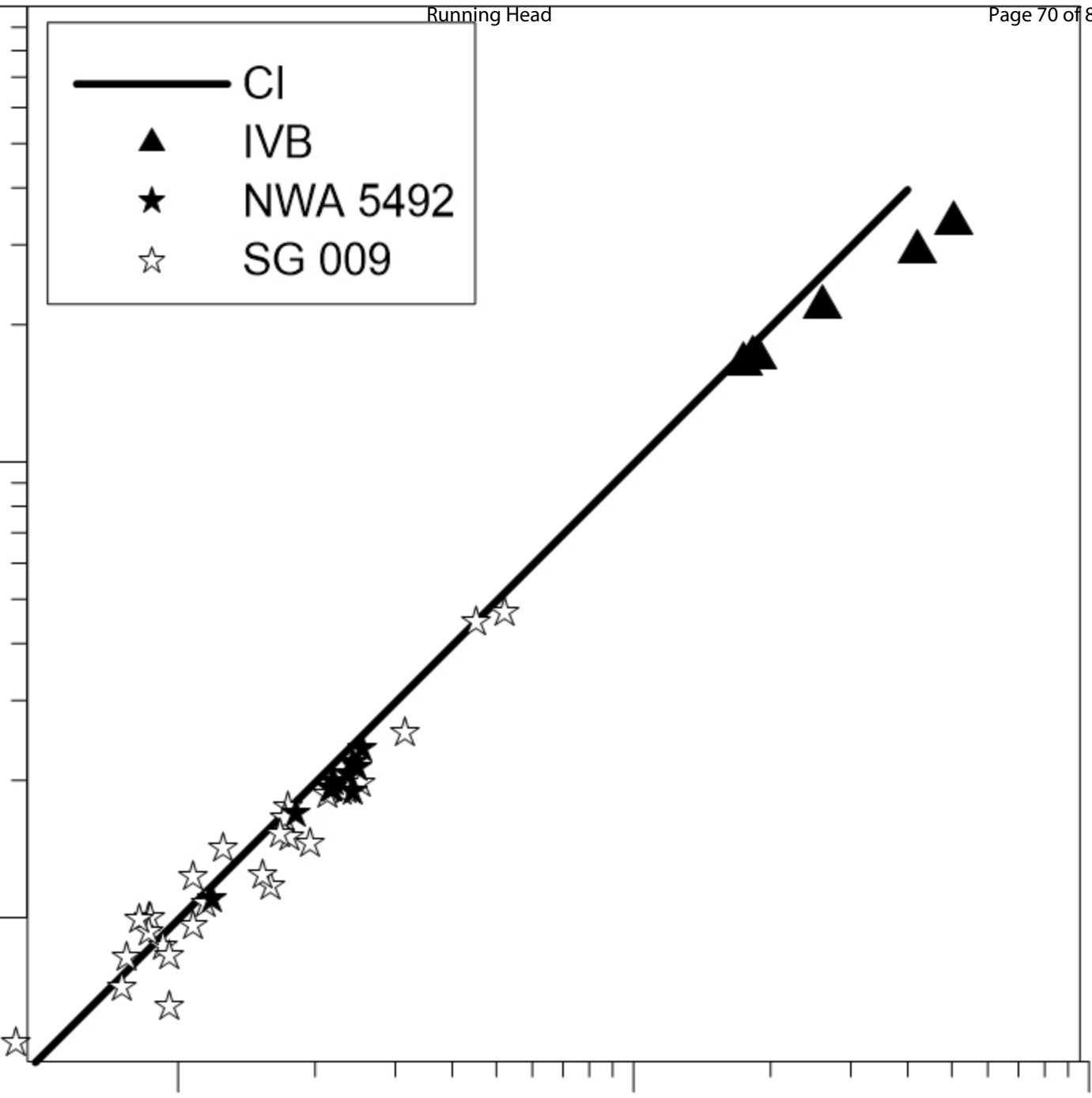
1

Meteoritics & Planetary Science

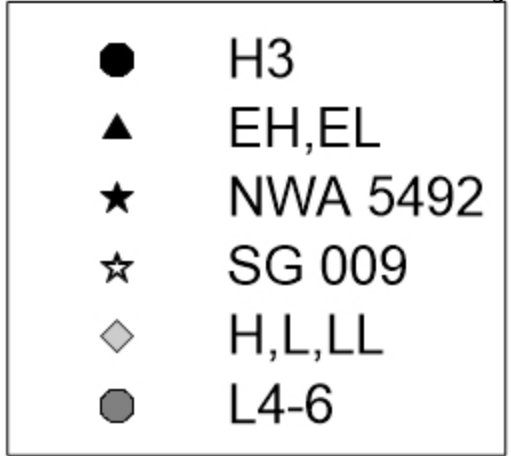
10

Os

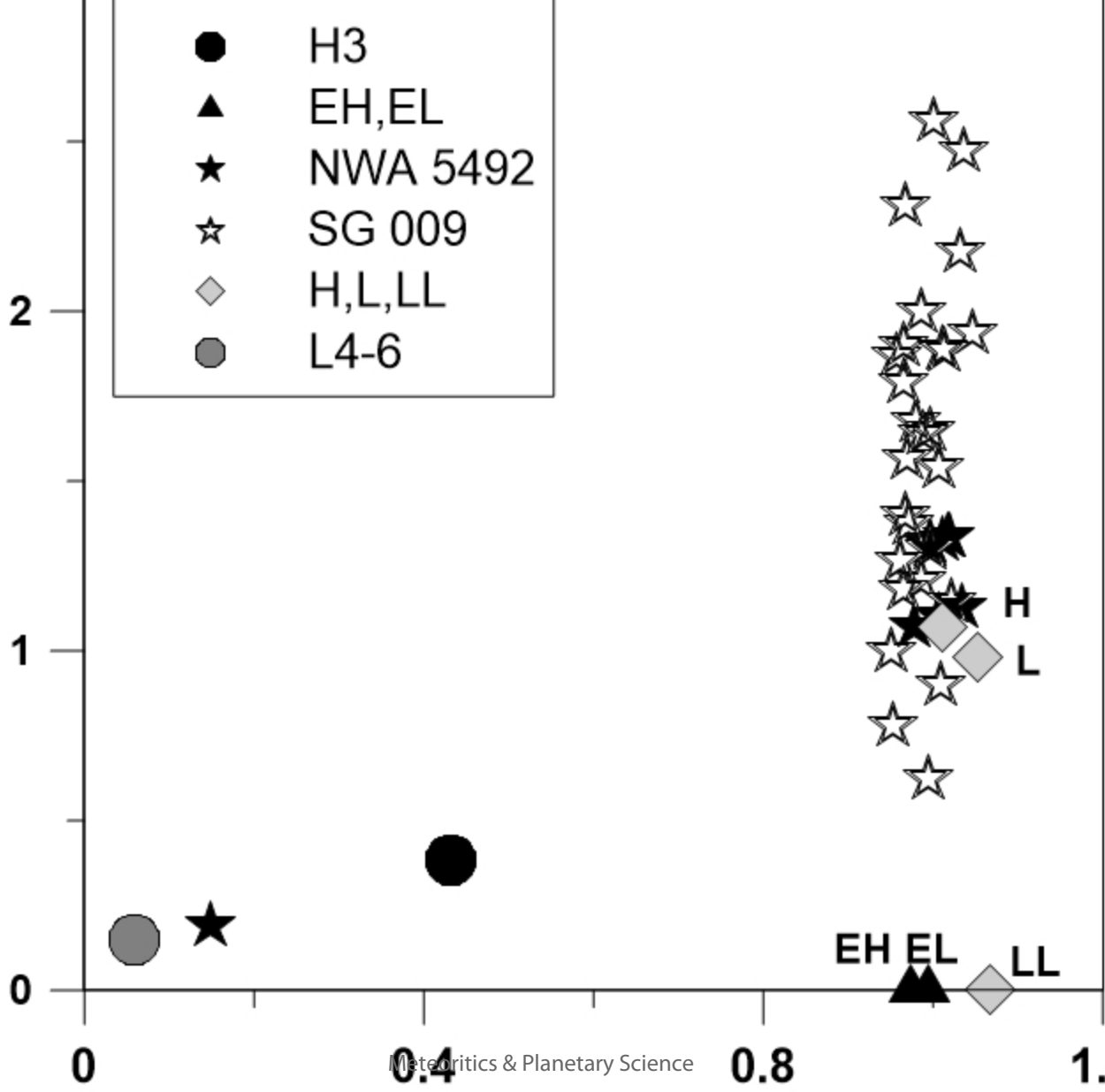
100



1
2
3
4
5
6
7
8
9
10
11
12
13
14
15
16
17
18
19
20
21
22
23
24
25
26
27
28
29
30
31
32
33
34
35
36
37
38
39



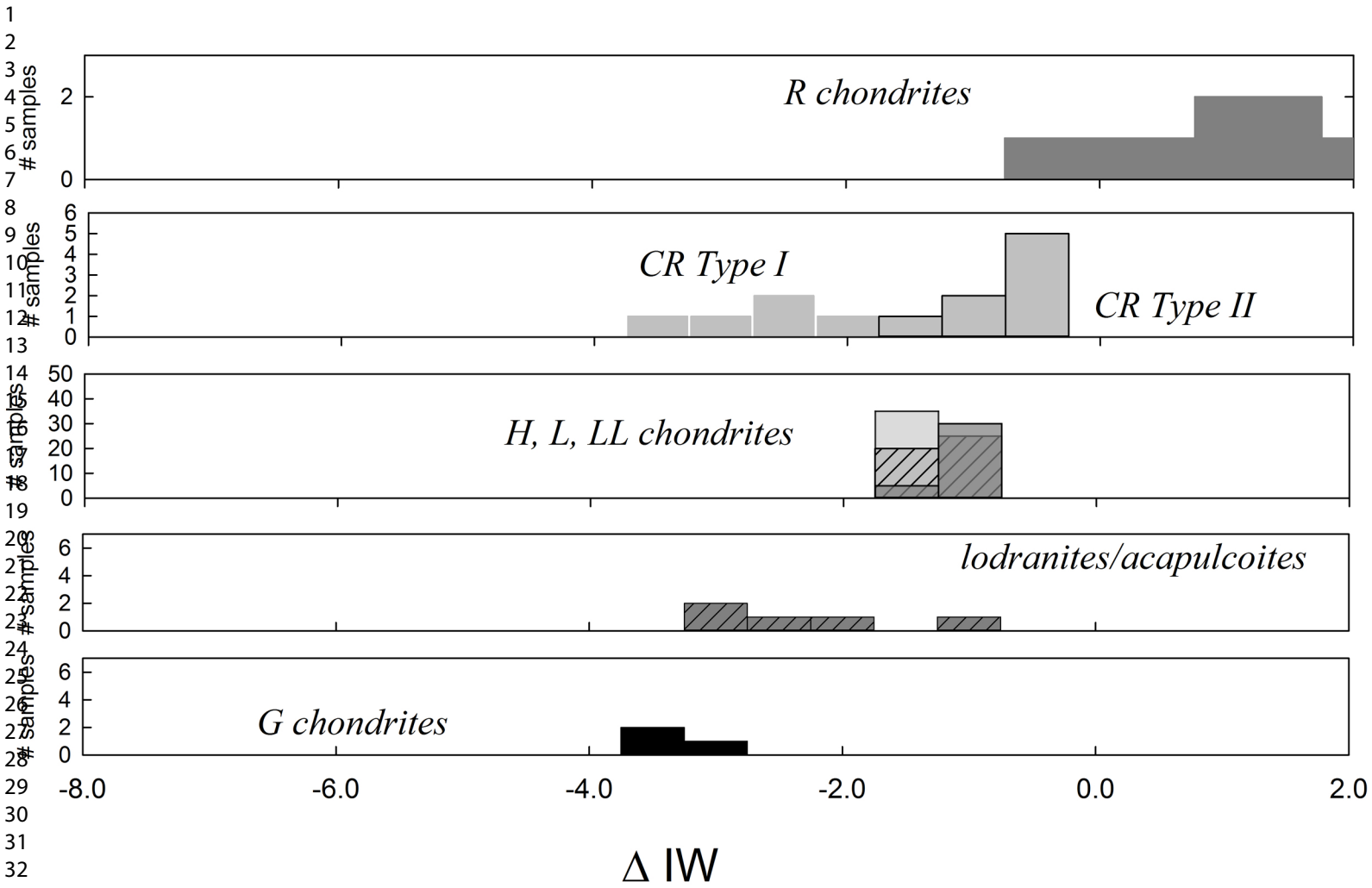
W/Ni



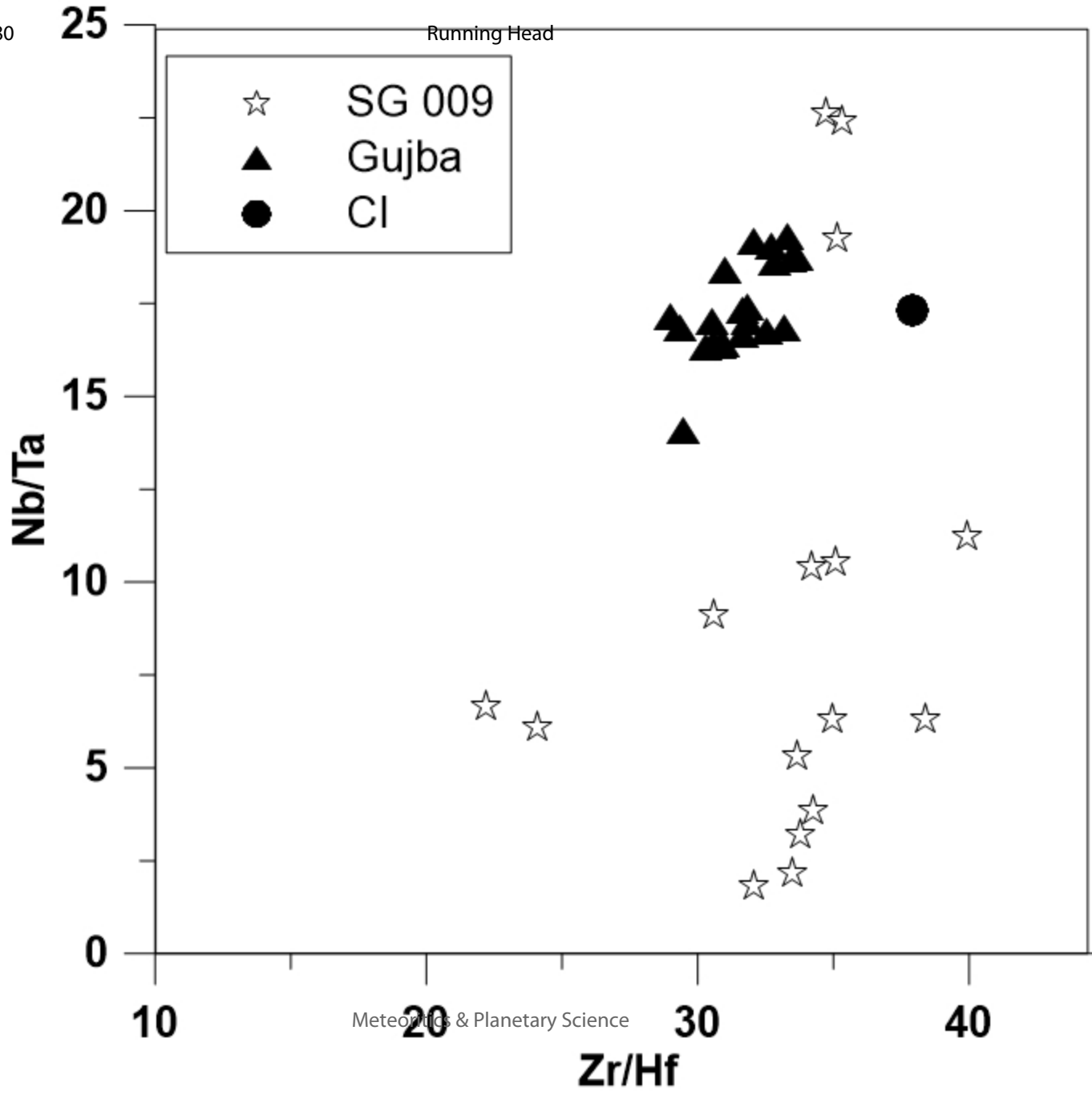
H
L

EH EL LL

Fe/Ni

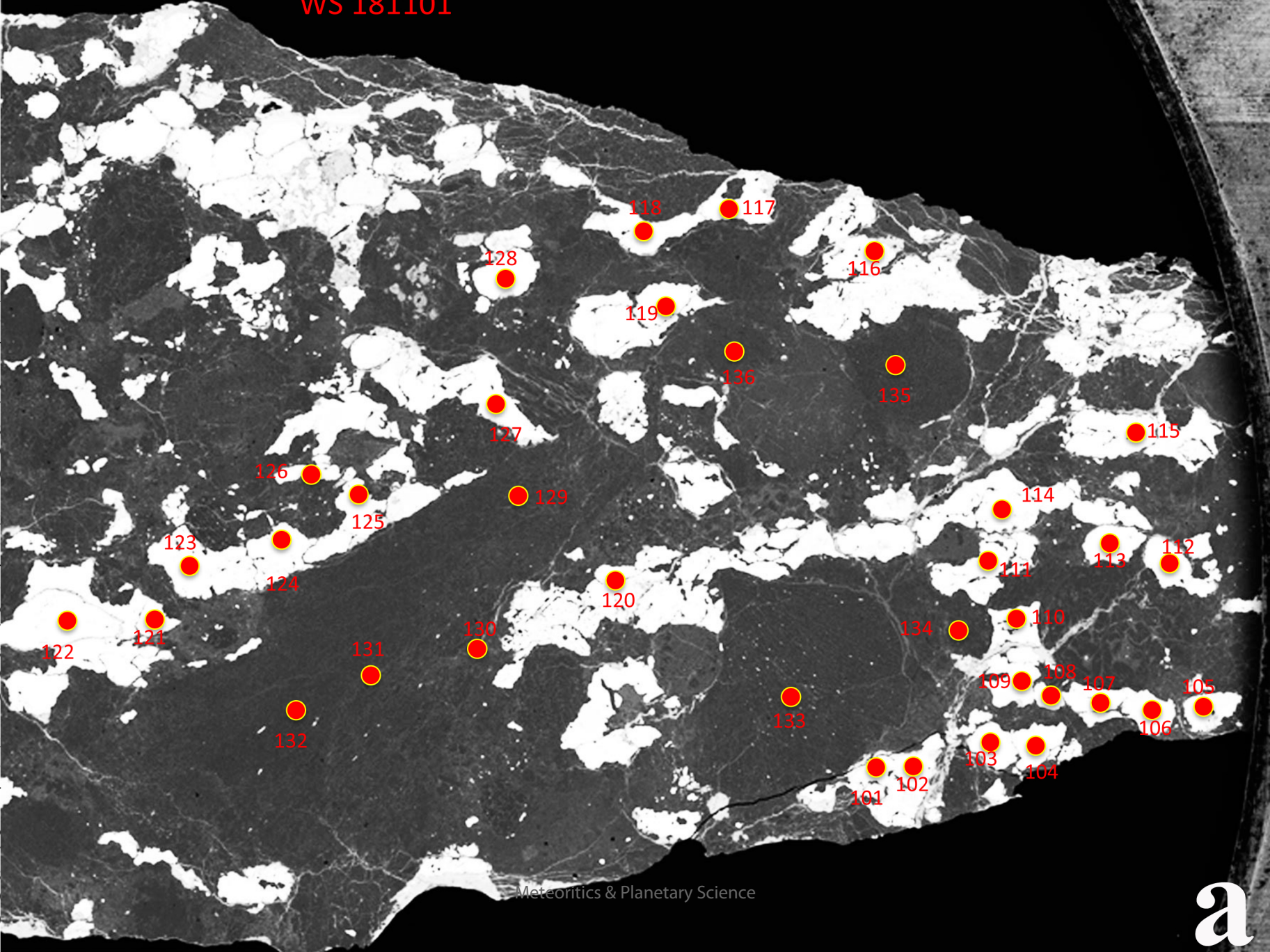


1
2
3
4
5
6
7
8
9
10
11
12
13
14
15
16
17
18
19
20
21
22
23
24
25
26
27
28
29
30
31
32
33
34
35
36
37
38
39



WS 181101

1
2
3
4
5
6
7
8
9
10
11
12
13
14
15
16
17
18
19
20
21
22
23
24
25
26
27
28
29
30
31
32
33
34
35
36
37
38
39
40
41

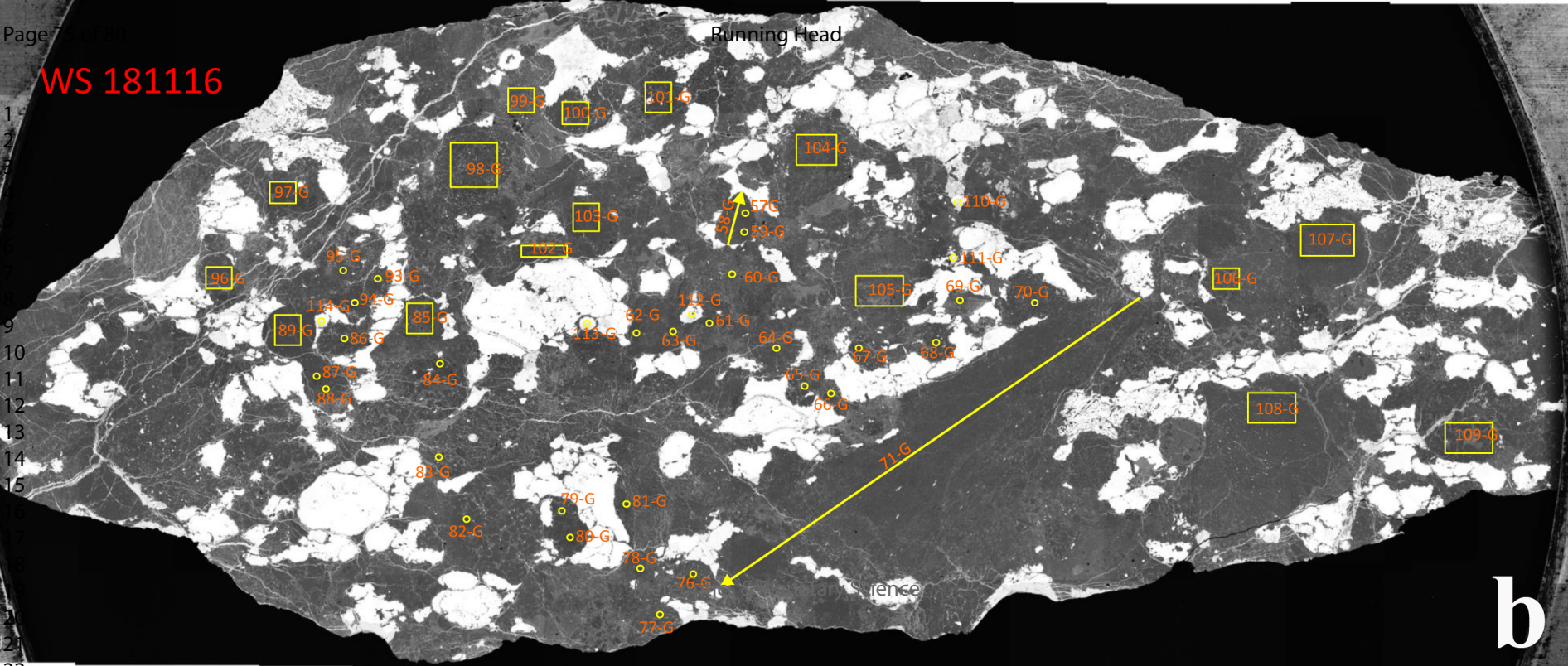


WS 181116

Running Head

1
2
3
4
5
6
7
8
9
10
11
12
13
14
15

16
17
18
19
20



b

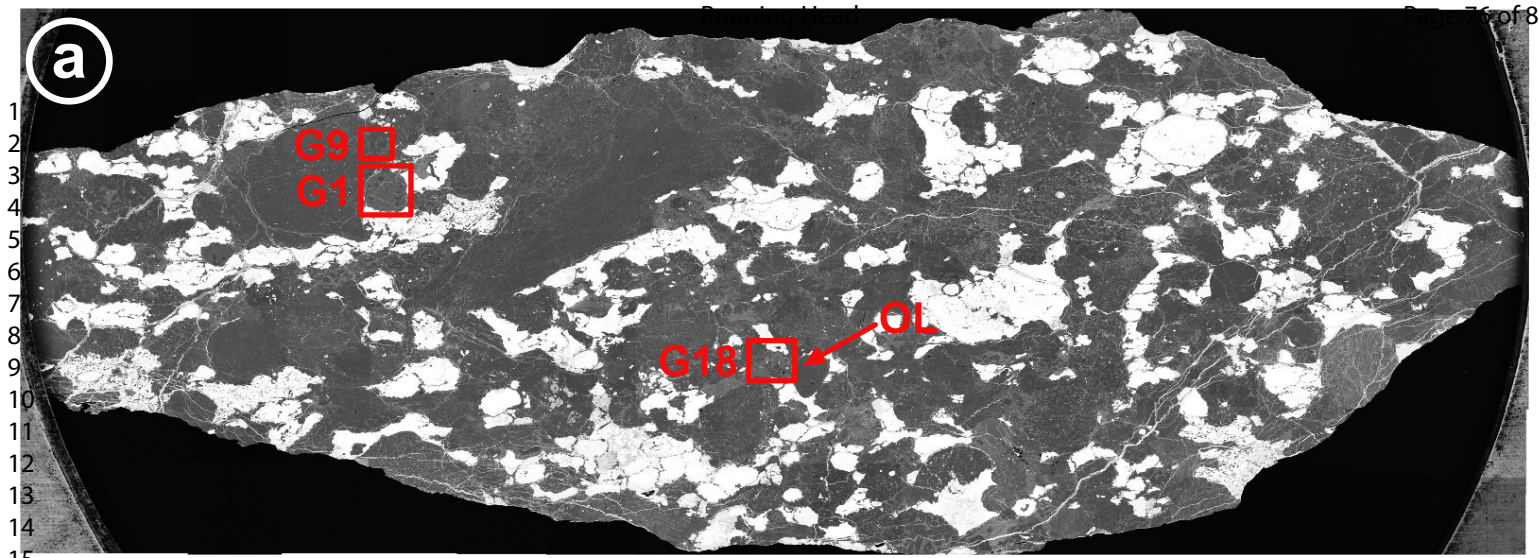


Fig. S2

(a) BSE image of the sample showing the regions G1, G9, G18 and the location of the single SIMS analysis "OL" (olivine).

(b), (c) and (d) are overlays of EDX mappings (red = Mg, blue = Al, green = Ca) and reflected light images of regions G1, G9 and G18. The reflected light images were taken while the sample was still coated with gold. The dark squares in the reflected light images are the SIMS spots.

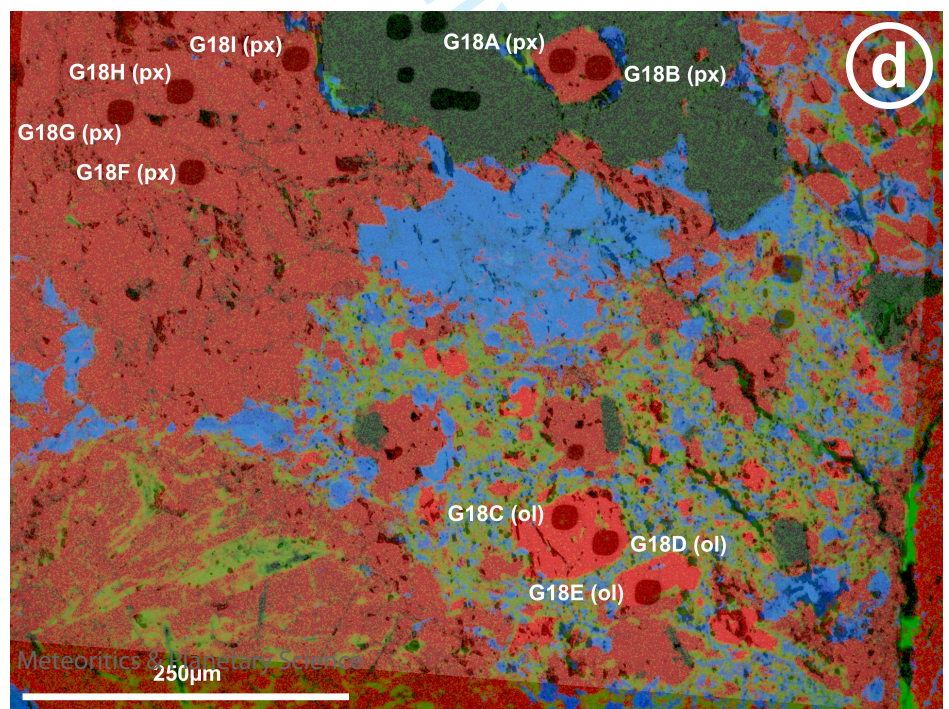
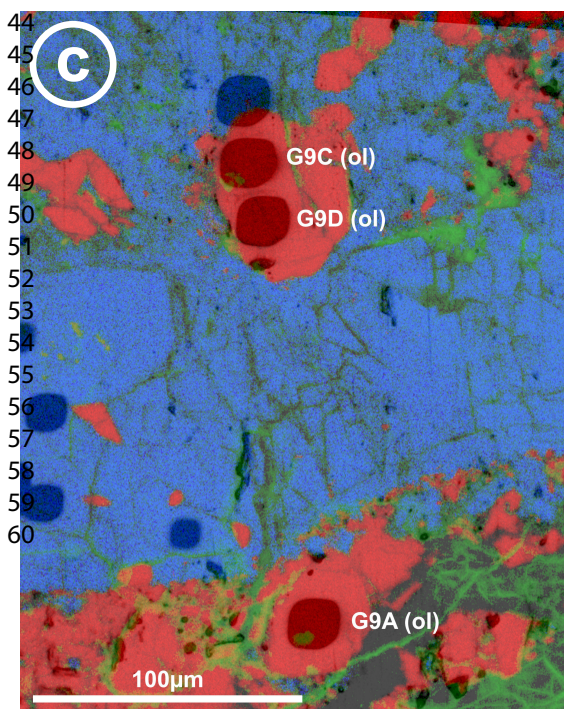
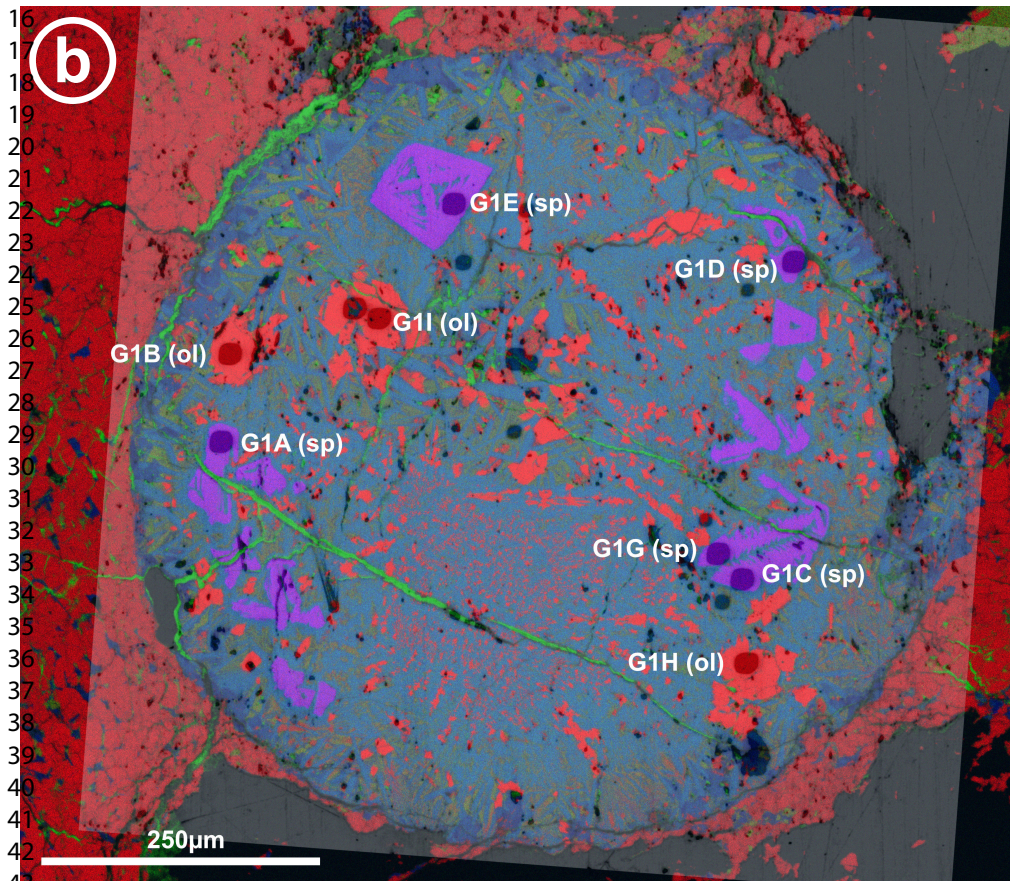


FIGURE CAPTIONS.

Fig. 1. Texture and constituents of Sierra Gorda 009: a) BSE image shows that the meteorite consists of a silicate fraction represented by chondrules and their fragments (dark grey), and Fe,Ni-metal nodules, 23 vol.% (white); b) X-ray element map (Mg - red, Ca - green, Al – blue) shows chondrules and their fragments consisting of Mg-rich silicate (red), only one Al-rich chondrule occurs (blue); c) X-ray element map (Fe - pink, S - light - blue, P – dark - blue, Cr - yellow), shows that sulfide (light-blue) is abundant, schreibersite (dark-blue) and magnesiochromite (yellow) are rare. Scale bar is similar for all images.

Fig. 2. BSE images of different objects from SG 009: a) POP chondrule consisting of olivine (Ol), pyroxene (Px), and glassy mesostasis (Glass), b) Al-rich chondrule consisting of spinel (Sp), pyroxene, olivine and anorthite (An), also shown on Fig. S2b – X-ray elemental map (Mg - red, Ca - green, Al – blue) ; c) SiO₂-rich chondrules containing SiO₂ – phase and pyroxene; d) PP - chondrule consisting of pyroxene and metal-rich mesostasis; e) etched grain of low-Ni metal with cross-cutting graphite grain in SG 009 (optical microscope, reflected light).

Fig. 3. BSE images of opaque assemblages from SG 009: a) Fe,Ni-metal (Met) – daubreelite (Dbr) – Mg-chromite (Mg-Chr) – Cr-troilite (Cr-Tr) + daubreelite; b) troilite + daubreelite + schreibersite (Scrb).

Fig. 4. PGE metal particles (PGE-Met) in: a) troilite (Tr) – daubreelite assemblage surrounded by secondary calcite (Cal); b) in enstatite (En) surrounded by iron hydroxide.

Fig. 5. a) Reflected light image of fine-grained area of achondritic clast (50x). Pyroxene is light grey, plagioclase is dark grey, troilite is white. b) Reflected light image of medium-grained area of achondritic clast (20x). Pyroxene is grey, plagioclase is dark grey, oxide is light-grey, troilite is white.

Fig. 6. Chemical compositions of a) olivine compared to olivine composition of CB chondrites, and b) low-Ca-pyroxene in SG 009. N – number of grains.

Fig. 7. Composition of metal in SG 009, NWA 5492, GRO 95551 (Weisberg et al. 2015), compared to metal from CBb-chondrites (Campbell et al. 2001), Isheyev CH/CBb (Ivanova et al. 2008) relatively CI (Anders and Grevesse, 1989).

Fig. 8. Siderophile elements distribution in metal of SG 009, NWA 5492 and GRO 95551 (Weisberg et al. 2015, Campbell and Humayun, 2003), H4-6 (Kong and Ebihara, 1997), CBb (Campbell et al. 2001), E chondrite (Kong et al. 1997) and CR chondrites (Kong et al. 1999) relative to CI composition (Anders and Grevesse, 1989). The shadow gray area is a range of the SG 009 metal composition.

Fig. 9. Representative CI-normalized (Anders and Grevesse, 1989) abundances of REEs of silicate chondrules from SG 009. OP-olivine porphyritic, PP-pyroxene porphyritic, PP/OP – olivine pyroxene porphyritic chondrules. (129-G - 136-G - numbers of chondrules).

1
2
3 Fig. 10. Bulk oxygen isotopic compositions (‰) of SG 009 compared to bulk values of two
4 other G chondrites NWA 5492 and GRO 95551 (Weisberg et al. 2012, 2015), HH chondrite
5 Burnwell (Russell et al. 1998), CH/CBb Isheyevo (Ivanova et al. 2008), as well as average
6 values of ordinary (Clayton et al. 1991), enstatite (Clayton et al. 1984) chondrites and
7 Rumuruti (Bischoff et al. 1994).
8
9

10 Fig. 11. Oxygen isotopic compositions (‰) of olivine and pyroxene from several POP
11 chondrules, and of olivine and spinel from an Al-rich chondrule from SG 009 compared to
12 bulk oxygen isotopic composition of SG 009, and mean values of NWA 5492 and GRO
13 95551 olivine and pyroxene ion probe data (Weisberg et al. 2012, 2015). ^{16}O rich
14 composition is best preserved in spinel and likely related to refractory precursor material.
15
16

17 Fig. 12. Three isotope plot of $^{21}\text{Ne}/^{22}\text{Ne}$ vs. $^{20}\text{Ne}/^{22}\text{Ne}$ for Sierra Gorda 009. Ne isotope data
18 points form a trend reflecting a mixture of solar wind and the cosmogenic component. The
19 contributions from cosmogenic neon are more pronounced at the late combustion steps. Other
20 components plotted include solar wind (SW; Heber et al. 2009), Earth's atmosphere (EA;
21 Eberhardt et al. 1965) and Q (Ott 2002). The cosmogenic component produced by galactic
22 cosmic rays (GCR) are given: $(^{20}\text{Ne}/^{22}\text{Ne})_c$ from Eugster and Michel (1995), $(^{21}\text{Ne}/^{22}\text{Ne})_c$ using
23 Leya and Masarik (2009) for the bulk chemical composition of SG 009 calculated from mineral
24 compositions and modes.
25
26

27 Fig. 13. The $^{40}\text{Ar}/^{36}\text{Ar}$ ratio variations in temperature steps for Sierra Gorda 009. The value of
28 the temperature step 1100°C is omitted. $^{40}\text{Ar}/^{36}\text{Ar}$ ratios of temperature steps $\geq 700^\circ\text{C}$
29 characterize argon isotopic composition of this meteorite without atmospheric contamination
30 observed at low temperatures.
31
32

33 Fig. 14. Carbon abundance and carbon isotopic composition of SG 009 (G) compared to EH,
34 OC, CH/CB and carbonaceous chondrites (Grady and Wright 2003).
35
36

37 Fig. 15. Nitrogen abundance and nitrogen isotopic composition of SG 009 (G) compared to
38 EH, OC, CH/CB and carbonaceous chondrites (Grady and Wright 2003).
39

40 Fig. 16. As vs Au composition of metal phase from SG 009, IIIAB (Wasson, 1999), IVA
41 (Wasson and Richardson, 2001), IIAB irons (Wasson et al. 2007), and metal phase from
42 NWA 5492 (Weisberg et al. 2015).
43

44 Fig. 17. Ir-Os correlation in metal of SG 009 compared with IVB iron (Campbell and
45 Humayun, 2005) and metal of NWA 5492, G-chondrite (Weisberg et al. 2015).
46

47 Fig. 18. W/Ni vs. Fe/Ni in the SG 009 metal phase. Data are normalized to CI (Anders and
48 Grevesse, 1989), and compared to data for metal from OC chondrites (Kong and Ebihara
49 1997), EH and EL (Kong et al. 1997) and NWA 5492 (Weisberg et al. 2015).
50
51

52 Fig. 19. Histograms of calculated oxygen fugacity (relative to the iron-wüstite buffer or ΔIW)
53 for the G chondrites (Sierra Gorda, GRO 95551, and NWA 5492) compared to R chondrites,
54 Type I and II chondrules in CR chondrites, H, L and LL chondrites, and lodranites and
55 acapulcoites. The G chondrites are calculated using the equilibrium $\text{Fe} + \text{FeSiO}_3 + \frac{1}{2} \text{O}_2 =$
56
57
58
59
60

1
2
3 Fe_2SiO_4 (as described by Righter and Drake, 1996), mineral compositions from this study
4 and those reported in Weisberg et al. (2001), Weisberg et al. (2012) and Weisberg et al.
5 (2015). All other data are from studies cited within Righter et al. (2016).
6

7
8 Fig. 20. Nb/Ta vs. Zr/Hf for SG 009 silicate chondrules and their fragments, and Gujba CC
9 and BO chondrules (Oulton et al. 2016) relative to chondritic (Anders and Grevesse 1989).
10

11 12 13 14 **SUPPLEMENTARY MATERIAL.** 15

16
17
18 Fig. S1. BSE image of the SG 009 section with data points analyzed by LA-ICP-MS method of
19 a) metal and silicates, b) silicates and sulfides.
20

21 Fig. S2. (a) BSE image of the sample showing the regions G1, G9, G18 and the location of the
22 single SIMS analysis "OL" (olivine), SP (spinel), PX (pyroxene).
23

24 (b), (c) and (d) are overlays of EDX mappings (red=Mg, green=Ca, blue=Al,) and reflected light
25 images of regions G1,G9 and G18. The reflected light images were taken while the sample was
26 still coated with gold. The dark squares in the reflected light images are the SIMS spots.
27
28
29
30
31
32
33
34
35
36
37
38
39
40
41
42
43
44
45
46
47
48
49
50
51
52
53
54
55
56
57
58
59
60

1
2
3 **REPLY to AE Cyrena Goodrich.**
4
5
6

7 Associate Editor: Goodrich, Cyrena

8 Comments to the Author:

9 please see attached, minor corrections to the English.

10 I have only one substantive question. Do you really mean to imply that OC experienced "fluid
11 assisted" thermal metamorphism? see bottom of page 4.

12 I thought metamorphism of OC was pretty dry.
13
14

15 Dear Cyrena,
16

17 Thank you very much for your comments and suggestions.

18 We carefully revised the manuscript according to all your comments and marked in red in the
19 revised version.
20
21

22 Reply for your question - Do you really mean to imply that OC experienced "fluid assisted"
23 thermal metamorphism?

24 Authors Jansen et al. (2019) meant that the fluid could be gaseous, dry and not necessary
25 contained water. However, we corrected this sentence (on page 4) and wrote in the manuscript:
26 "In contrast to the metal-rich chondrites, but similar to OCs, the meteorite NWA 12379
27 experienced thermal metamorphism that resulted in nearly complete chemical equilibration of
28 chondrule olivine, and formation of Cl-apatite, merrillite, chromite, tetrataenite, and ferroan
29 olivine that replaces low-Ca pyroxene."
30
31

32 Sincerely,
33

34 Marina Ivanova
35
36
37
38
39
40
41
42
43
44
45
46
47
48
49
50
51
52
53
54
55
56
57
58
59
60